Development of a Yeast Biosynthetic Platform for Rapid Production and Engineering of an Influenza Virus-like Particle Vaccine

by

Brett D. Hill

A dissertation submitted in partial fulfillment
of the requirements for the degree of
Doctor of Philosophy
(Chemical Engineering)
in the University of Michigan
2020

Doctoral Committee:

Associate Professor Fei Wen, Chair
Professor Erdogan Gulari
Professor Akira Ono
Professor Henry Wang

Brett D. Hill

labrett@umich.edu

ORCID iD: 0000-0002-7220-6708

Dedication

To my parents, Karen and Dallas Hill

Acknowledgements

First, I would like to acknowledge my advisor Dr. Fei Wen. Working with Fei has forced me to step outside my comfort zone. She consistently encouraged me to push through stubborn research problems that I initially believed were unsolvable, ultimately leading to success. In addition, Fei taught me the importance of framing and selling my ideas, skills that will undoubtedly help me in the future. I would also like to thank my committee members Prof. Akira Ono, Prof. Erdogan Gulari, and Prof. Henry Wang for their helpful feedback on my broad thesis topic. Their enthusiasm for some of my key findings encouraged me, and I appreciated their practical insight. I would also like to thank the members of the Wen lab for their feedback and creating a positive working environment. In particular, I appreciate the help and thoughts provided by Andrew Zak, Dr. Prabhu Ponnandy, Luke Bugada, and Dr. Syed Monem Rizvi who assisted with these projects.

Outside of the lab, I was fortunate enough to be in the company of a great group of friends. From fantasy football, camping trips, climbing, and darts tournaments, I will look back on my times spent with Mason Smith, David Hietala, Vikesh Chandrashekar, Cornelius Cilliers, Nishanth Bharadwaj, Sumit Bhatnagar, and Trenton Wilke fondly. I would also like to acknowledge my future wife Katherine Carl for her patience, love, and support. No matter how my lab experiments turned out, she was always there to lift my spirits and motivate me. I am excited for our future together. Finally, I would like to thank my parents Karen and Dallas Hill. I appreciate the support and opportunities they have provided for me throughout my life and their encouragement to pursue my Ph.D. While pursuing a Ph.D. has been the my most challenging endeavor, it has also been the most rewarding.

Table of Contents

List of Tables

List of Figures

List of Appendices

Abstract

Although vaccination is the primary means of preventing influenza virus infection, current influenza vaccines are only moderately effective and do not provide protection against strains with pandemic potential. To overcome these limitations, new vaccine approaches are desperately needed. Virus-like particles (VLP) have recently emerged as attractive influenza vaccine candidates due to their immunogenicity, safety, and tunability. Despite their potential, engineering influenza VLP to elicit long-lasting protection against diverse influenza strains remains challenging. In this dissertation we develop a novel platform for the rapid synthesis, engineering, and testing of influenza VLP vaccine candidates in order to accelerate their development as next generation influenza vaccines.

Forward progress in the development of influenza VLP vaccines has been impeded by their manufacture in higher eukaryotic hosts, which are cumbersome to genetically manipulate. To accelerate VLP synthesis, we investigated if the lower eukaryote *Saccharomyces cerevisiae* could support the production of influenza VLP. We show that, while *S. cerevisiae* can successfully express the critical influenza hemagglutinin (HA) and M1 proteins from diverse influenza subtypes, HA does not efficiently traffic to the plasma membrane where VLP formation takes place. Notably, we demonstrate that fusion of a fluorescent protein to the C-terminus of HA results in a dramatic increase in plasma membrane localization. Furthermore, following cell wall removal

of cells expressing M1 and this fluorescent HA, we discovered the supernatant contained fluorescent nanoparticles possessing functional properties of influenza virus including the ability to agglutinate red blood cells and undergo endocytosis in a sialic acid dependent manner. Thus, we demonstrate for the first time the capacity of *S. cerevisiae* to support influenza VLP production, significantly enhancing the speed at which influenza VLP can be manufactured.

To facilitate the rapid engineering of these yeast VLP strains, high-throughput protein detection methods are necessary for screening and strain characterization. To fill this need, we developed yeast intracellular staining (yICS), a technique that enables fluorescent antibodies to access intracellular compartments of yeast cells while maintaining their cellular integrity for flow cytometry. We demonstrate that yICS expedites identification of rare, high-producing yeast clones and allows simultaneous detection of multiple intracellular proteins. Along with the yeast influenza VLP system, these approaches combine to enable rapid prototyping of influenza VLP vaccine candidates.

To support the comprehensive testing of VLP vaccines, we next validated high-dimensional mass cytometry (CyTOF) for in-depth immune characterization. As a proof of concept, we applied CyTOF to study the early stages of influenza infection in the mouse lung. This technology enabled quantitative tracking of 24 cellular subsets over the course of infection including their expression of activation markers, cytokines, and influenza viral proteins, making this study the most comprehensive single-cell analysis of the influenza immune landscape to date. Our investigation provides a high-resolution view of the early inflammatory response followed by the initiation of the adaptive response. Specifically, we show the importance of effector T cells in shaping the lung cytokine environment and provide new insights into the susceptibility of immune cells to viral infection and replication *in vivo*. Overall, this dissertation develops novel tools that synergistically combine to form a rapid platform for designing, building, and testing influenza VLP that not only can accelerate development of universal influenza vaccines but is also generally applicable for viral vaccine development, biologics synthesis, and gaining a systematic understanding of their impact on the immune system.

Chapter 1. Introduction

1.1. Publication Information

Hill, B. D., Zak, A. J., Khera E., and Wen, F. Engineering Virus-like Particles for Antigen and Drug Delivery. *Curr. Protein Pept. Sci.*19(1):112-127 (2018).

Materials in sections 1.3.1, 1.3.2, and 1.4.1 have been modified from the published document and adapted for this text.

1.2. Influenza Virus

The word influenza originated in Italy during the 1500s stemming from the belief that disease outbreaks were caused by the heavens asserting their "influence" on the Earth.[1] Today, influenza is recognized as being caused by a highly infectious virus from the *Orthomyxoviridae* family with four known types denoted as influenza A, B, C, and D. While influenza C and D cause little to no disease in humans, influenza A and B circulate seasonally in the human population, leading to an estimated 290,000 to 650,000 deaths per year.[2] Influenza A virus, in particular, is known to circulate in several animal reservoirs including humans, birds, pigs, cats, dogs, bats, seals.[3] In addition to causing seasonal influenza epidemics, influenza A viruses frequently cross interspecies barriers, leading to influenza pandemics that can be much more deadly. Most notably, the 1918 influenza pandemic was estimated to have killed between 1% and 6% of the world's population.[4] Consequently, disease caused by influenza A remains a considerable threat to global public health. Unless otherwise mentioned, all following references to influenza are in regard to influenza A.

1.2.1.Anatomy of Influenza Virus and Viral Life Cycle

Influenza is an enveloped virus with a lipid membrane that protects a core of eight negative sense, single-stranded RNA segments that encode the viral proteins (**Figure 1.1**). Embedded in the host-derived lipid bilayer are three surface proteins – hemagglutinin (HA), neuraminidase (NA), and matrix protein 2 (M2) – that make up approximately 80%, 17%, and 3% of the total viral surface proteins, respectively (**Figure 1.1**).[5] Immediately under the lipid bilayer is the matrix protein 1 (M1), the most abundant viral protein. M1 interacts with the cytoplasmic tails of HA, NA, and M2 as well as the internal ribonucleoprotein (RNP)[5] core that contains the viral genome as well as several proteins related to its packaging and replication. Together, these proteins play instrumental roles in the viral life cycle.

The viral life cycle begins when the HA "spike" protein binds to sialic acid residues on the surface of a cell, leading to viral uptake into the cell through endocytosis.[6] As the endosome becomes acidified, M2 transports H^+ ions into the interior of the virion[7] leading to dissociation of M1-RNP complex, a critical step required for release of the viral genome.[8] In parallel, the acidified endosome induces a conformational change in HA that enables HA to fuse the viral and endosomal membranes,[7] ejecting the RNP core into the cytoplasm. The RNP core is then transported to the nucleus where the genetic material is replicated and translated into viral proteins. Newly translated HA, NA, and M2 viral proteins traverse the secretory pathway on their way to the plasma membrane where viral assembly occurs. M1 associates with RNP in the nucleus, causing the M1-

RNP complex to be exported into the cytoplasm where it subsequently binds to the cytoplasmic tails of HA, NA, and M2 proteins on the apical surface of the plasma membrane.[9] Following attachment of the M1-RNP complex, HA is thought to initiate viral budding by inducing outward curvature of the plasma membrane followed by scission of the budded membrane by M2,[6] forming the complete viral particle. Due to HA's affinity for sialic acid, progeny virions are initially attached to the host cells surface, requiring the sialidase activity of NA to facilitate the release of the newly formed virion to complete another viral life cycle.[6,10]

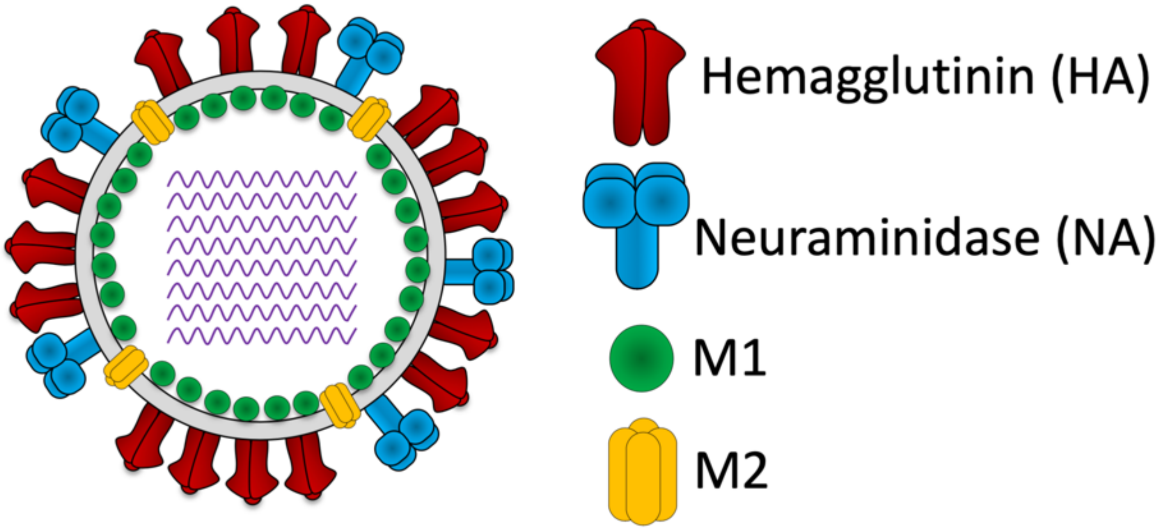

Figure 1.1. Anatomy of influenza virus
Influenza A is an enveloped, negative sense RNA virus with an 8-segment genome. Hemagglutinin (HA), neuraminidase (NA), and matrix protein 1 (M1), and matrix protein 2 (M2) all play critical roles in the virus life cycle and are important targets for vaccination.

1.2.2. Antigenic Drift and Shift of Influenza Viruses

A major difficulty in preventing the spread and infection of influenza is the ability of the virus to rapidly mutate. Influenza's error prone RNA polymerase is responsible for about one mutation for every viral genome replicated.[11] When combined with the fact that a single influenza infected cell produces on the order of 10,000 progeny virions,[12] it is clear why influenza has one of the fastest mutation rates of any known virus.[13] While most of these mutations negatively affect viral fitness, a small number result in evolutionary advantages, such as the ability of escape preexisting influenza-specific antibodies. Antibody responses against influenza are predominantly mounted against the globular head of the influenza HA and NA surface proteins.[14,15] However these regions are highly susceptible to mutation by the error-prone RNA polymerase, allowing the virus to escape preexisting antibodies.[14] Termed genetic drift, this phenomenon is responsible for seasonal variations in influenza virus that require updated annual vaccines.

Less frequently, the influenza virus undergoes what is known as genetic shift. There are currently 18 known HA subtypes (H1 – H18) and 11 known NA subtypes (N1 – N11) with certain subtypes being predominant in birds, pigs, humans, and other species.[10] When two influenza viruses of distinct subtypes infect the same cell, resulting viral progeny can incorporate genome elements from both parent viruses. This genetic reassortment, termed genetic shift, can give rise to viral progeny that have distinct evolutionary advantages. While only a few mutations in influenza surface proteins (genetic drift) enable influenza to evade the immune system, genetic shift can result in influenza viruses with entirely new proteins on their surface. With these new proteins, it is possible that very few, if any, host antibodies are effective against this new virus, leading to a much more severe infection.[10] In a little over a century, genetic shift has resulted in four pandemics, the worst of which caused 50 – 100 million deaths worldwide.[16] The most recent genetic shift was the H1N1 “swine flu” virus that circulated in 2009.

1.2.3. Current Vaccination Approaches and Their Challenges

While antiviral drugs are available, vaccination currently provides the best approach for preventing the spread and infection of influenza virus. Vaccine production begins with the prediction of two influenza A strains and two influenza B strains that will be circulating in the upcoming influenza season as a result of global surveillance by the Centers for Disease Control (CDC) and the World Health Organization (WHO). Next, these viruses are propagated in hundreds of millions of chicken eggs in a process that remains largely unchanged since the 1960s.[17] The virus is then inactivated with formaldehyde or β-propiolactone and disrupted with a detergent to form the split-virus vaccine. Alternatively, the HA protein from this split vaccine can be partially purified, forming what is known as the subunit vaccine. While these formulations are effective for generating virus-specific antibodies, they fail to efficiently generate virus-specific CD4 and CD8 T lymphocytes[18,19] that play a vital role in the immune response and have been shown to provide heterosubtypic protection.[19,20]

With the goal of eliciting improved humoral and cellular immune responses, live attenuated influenza virus (LAIV) vaccines were developed at the University of Michigan by Dr. Hunein Maassab in the 1960s. LAIV vaccines are produced by swapping the desired HA and NA proteins into the viral backbone of a temperature-sensitive strain.[21] The resulting virus grows at a reduced temperature of 25 °C which confines its replication to the nasal passage, enabling the immune system to be stimulated through controlled viral replication without risk of infection.[21] While initial clinical studies were promising, LAIV vaccines have demonstrated lower effectiveness compared to inactivated vaccines over the course of multiple influenza seasons.[22,23] There are also other concerns about LAIV vaccines. Due to this ability replicate, there is potential that LAIV may revert to virulence through genetic drift or genetic shift.[24] While the validity of these safety concerns has yet to be determined, LAIV are also less stable and more sensitive to elevated temperatures than their inactivated counterparts.[25] Since the protection induced by LAIV is highly dependent on its ability to replicate, breaks in the cold chain can render the LAIV vaccines less effective.[26] For the same reason, LAIV vaccines are less suitable for vaccination against suspected pandemic strains that have not yet developed the ability to replicate efficiently in the upper respiratory tract in humans.[27,28] Moreover, due to LAIV's ability to replicate, LAIV vaccines are not recommended for the most vulnerable demographics – the very young, the elderly, and the immunocompromised – which are precisely the populations that require the most protection.

The reliance of both inactivated and LAIV influenza vaccines on chicken egg production also has several limitations. The procedure of adapting the virus for growth in chicken eggs, aside from taking several weeks, can introduce mutations.[29] The reliance of the process on large quantities of chicken eggs also makes the process vulnerable to egg shortages due to avian pandemics. Probably most concerning is the long production timeframe of roughly 6 months. In the case of a pandemic, many deaths could occur before sufficient vaccine is available. Due to these concerns, there is significant interest in identifying immunogenic and replication-incompetent influenza vaccines that do not rely on chicken eggs.

1.3.Virus-like Particles (VLP)

In the mid 1960s, pathologists first observed nanoscale particles from virus-infected human and animal tissue samples that resembled a virus in morphology but were noninfectious.[30] These virus-like particles (VLP) were soon discovered to consist of viral proteins arranged in the repetitive, highly organized structures of the native virion but lacking the viral genetic (**Figure 1.1**). These features attracted significant interest in developing VLP as novel immunogens in prophylactic vaccines and were a major departure from the previously adopted "isolate-inactivate-inject" vaccination approach, which had spawned the successful polio, measles, and rubella vaccines.[31]

The first VLP vaccine was approved in 1981 and was composed of naturally occurring hepatitis B VLP purified from the plasma of chronically infected individuals.[32] Although the vaccine was costly to produce and was sourced from a limited supply of donors,[33] it was nevertheless very effective and demonstrated the vaccination potential of VLP. With the advent of recombinant DNA technology, it was discovered that high yields of hepatitis B VLP could be produced in the yeast *Saccharomyces cerevisiae* upon expression of hepatitis B surface antigen (HBsAg). As a result, these VLP were formulated into the successful Recombivax HB vaccine licensed in 1986.[33] The use of recombinant methods to produce VLP marked a second generation in VLP production, leading to higher production yields and the ability to produce VLP derived from viruses of diverse genetic backgrounds (**Figure 1.1**).

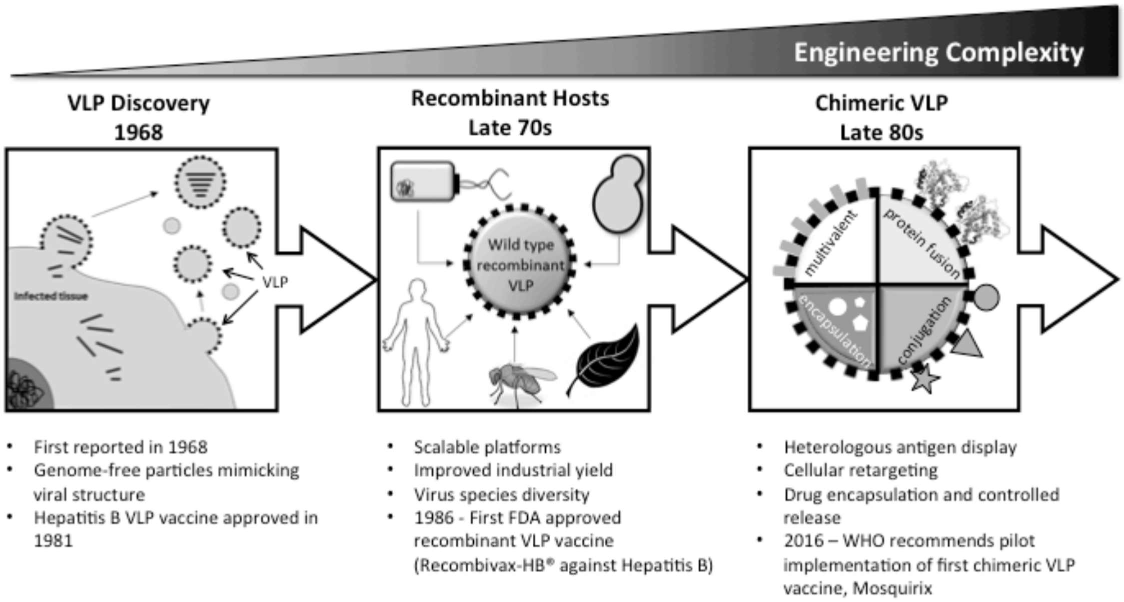

Figure 1.2. An overview of the evolutionary stages in the development of VLP
Wild-type VLP were first discovered in virus infected tissue samples, but advances in recombinant engineering enabled VLP to be produced in a variety of recombinant host systems. More recently, additional functionalities not present in VLP composed of native viral proteins have been introduced by chemical and genetic engineering approaches. These modifications have enabled increased tunability and greatly expanded applications including their use as antigen and drug delivery vehicles.

The high tailorability of VLP proteins has since been the subject of chemical and genetic engineering to expand their applications beyond the simple presentation of native antigenic epitopes. These third-generation chimeric VLP have broadened the applications of VLP to include their use as imaging reagents,[34-37] template synthesis,[38,39] and catalysts[40-42] (**Figure 1.1**). Nevertheless, the most studied applications of VLP lies in their use as vaccines and drug delivery vehicles.

1.3.1. VLP for Drug Delivery

Effective drug delivery vehicles should ideally be safe, encapsulate cargo, specifically target cells or tissues, and release the cargo at the destination in a controlled manner. VLP lend themselves well to these objectives, as viruses have perfected the art of cellular delivery of their genetic material over eons of evolution. In addition, VLP are versatile structures amenable to chemical and genetic modifications that result in predictable, highly defined, and homogenous alterations. These traits have generated numerous interests in using VLP as vehicles for drug delivery.[43,44]

The inherent affinities present in VLP can be explored to encapsulate desirable materials. For instance, the inner surface of the viral capsid is often positively charged and thus amenable to encapsulating genomic materials, therapeutic nucleotides,[45-47] and other negatively-charged substrates such as polymers,[48] nanoparticles,[49] and enzymes.[50] In addition, the pre-existing mechanisms that viruses use to bind nucleic acids can be repurposed to incorporate diverse cargos in VLP. For example, MS2 viral capsid bind an RNA sequence known as the *pac* site.[51] Through conjugation of this *pac* site to quantum dots, siRNA, doxorubicin, or ricin toxin-A chain, these cargos were encapsulated in the MS2 capsids by disassembly and reassembly *in vitro.*[52] For a more simplified production strategy, intracellular VLP assembly and cargo encapsulation was accomplished utilizing bi-functional RNA aptamers that bind both Qβ coat protein and an arginine rich peptide (Rev) fused to fluorescent proteins[53] or luciferase and peptidase E enzymes.[54]

Following encapsulation of the desired payload, VLP need to be targeted to the desired delivery site. VLP often retain the natural tropism of the wild-type virus, which can be exploited to deliver therapeutic cargoes to specific tissues or organs. For example, JC polyomavirus and rotavirus VLP have been shown to target xenografted human bladder tumor nodules or intestinal cells[55,56] in mice, respectively. In addition, VLP can be retargeted by the display of cell-specific targeting ligands when the natural tropism of the VLP does not target the desired site. Cancer cells, one of the most common targets for drug delivery, often overexpress receptors that help promote their growth such as folate, epidermal growth factor, and transferrin receptors.[57] Therefore, VLP presenting these ligands have been widely used for targeted delivery and uptake by various cancer cells.[58-61] In addition, antibodies have been utilized to retarget VLP for drug delivery[62,63] due to their exquisite specificity. However, antibodies and their derivatives are generally expensive and too big to be genetically fused to VLP proteins (with some exceptions[62,64]). Due to these limitations, VLP have been conjugated with other smaller (< 20 kDa) and less expensive targeting ligands in the form of DNA aptamers[65-67] and peptides[52,68], which can achieve similar binding specificity and affinity as antibodies.[57]

1.3.2. VLP for Vaccination

As viruses often display many copies of only a few proteins,[69] it has been postulated that the co-evolution of viruses and vertebrates has led to the ability of the immune system to rapidly detect, discriminate, and respond to the repeated and ordered structure of a virus.[16] Therefore, vaccination with the organized and repetitive structure of a VLP often provides enhanced immunogenicity compared to less organized vaccine designs, such as protein subunit vaccines.[70,71] In fact, VLP are such potent immune stimulators of B cells that self-antigen displayed on VLP has been shown to break B-cell self-tolerance and induce the production of autoreactive antibodies.[72-75] The small particulate nature of VLP also leads to efficient uptake by antigen presenting cells (APCs) and results in subsequent activation of both CD8 and CD4 T cells, which can further enhance the antibody response.[76,77] For these reasons, VLP often make great vaccine immunogens as witnessed by the success of the hepatitis B, HPV, and malaria vaccines. However, designing next generation vaccines to combat diseases that have evaded prior vaccination efforts will require additional VLP functionalization to enhance their immunogenicity and to strategically focus the immune response towards key epitopes. Enhancing the immunogenicity of VLP will be discussed in **Section 1.4.1** while an overview of epitope display on VLP follows.

Many viruses such as influenza and HIV as well as non-viral targets such as malaria and cancers require the immunogenic presentation of cross-protective epitopes. Rational epitope design aided by identification of immunogenic insertion sites, epitope flanking sequences, and multivalent epitope display has increased the versatility of VLP and has allowed them to initiate tailored and specific immune responses to a variety of targets. The identification of B-cell and T-cell epitopes that can be exploited for vaccination is a major research field that presents many challenges.[78-82] In cases where epitopes are unknown for a given antigenic protein, the whole or nearly whole protein can be delivered in its native form for immune recognition. Indeed, by means of genetic fusion,[63,83-92] conjugation,[93,94] or pseudotyping,[62,83,95-97] large antigenic proteins have been successfully incorporated into VLP, eliciting effective antigen-specific humoral and/or cellular immune responses. In cases where the epitopes have been identified, the delivery of selected epitopes presents several advantages over that of large antigens. First, epitopes are often easier to be incorporated into a VLP than larger antigens thanks to their short sequences imposing minimal interference with VLP protein function and assembly. Many sites in a range of VLP proteins have been successfully used for epitope insertion.[98] Second, the small size of epitopes also entails the possibility of incorporating multiple different epitopes or multiple copies of the same epitope into one or more sites in a VLP protein to elicit an improved immune response. For example, multiple epitopes have been inserted into HBcAg VLP to improve cytotoxic T-cell responses against hepatitis B virus[99] and *Plasmodium falciparum*[100] as well as to increase the breadth of antibody response against influenza virus.[101] Other studies have demonstrated that increasing the number of repeats of an influenza M2 epitope displayed on HBcAg[102] or nodavirus[103] VLP increases M2-specific antibody titers in mice. Finally, epitopes that are specific for certain immune cells such as B cells, CD4$^+$ T cells or CD8$^+$ T cells have been incorporated into VLP to selectively activate different arms of the adaptive immune system[104] providing further control over the desired immune response.

Despite these advantages, there are several challenges associated with the design of epitope-based vaccines. In the case of B-cell epitopes, their location in a VLP carrier protein can greatly affect the magnitude of the resulting antibody response. It has been shown that the region around amino acid 80 of the HBcAg protein is the major antigenic determinant of the HBcAg VLP,[105] and the placement of heterologous epitopes in this immunodominant region results in a stronger epitope-specific antibody response than in other locations of the HBcAg.[106] Another challenge is associated with the conformational structure of a significant fraction of B-cell epitopes,[107] making it more difficult to present them on the VLP surface in an antigenic form than linear epitopes. Yet, vaccines targeting conformational B-cell epitopes provide a means of generating broadly neutralizing antibodies for viruses that have proven difficult to vaccinate against such as influenza[108] and RSV.[109,110] One class of the most common conformational epitopes are those with α helical structure found in coiled-coil motifs of many enveloped viral glycoproteins.[111] Antibodies targeting these α helix epitopes have been shown to inhibit cellular entry of HIV,[112] Ebola,[113] and influenza[114] viruses. To achieve conformational presentation of these α helix epitopes, the leucine zipper domain of the yeast transcription factor GCN4 has been used as the flanking sequence to stabilize their conformation.[112,115-117] Presentation of epitopes with more complex conformations, such as a helix-turn-helix structure, is not as straightforward and may require computational design of specialized scaffolds to obtain the correct epitope conformation.[109]

T-cell epitopes, although linear, also present unique challenges. The sequences flanking T-cell epitopes have been implicated in the efficiency of antigen processing and presentation,[118,119] thus present an engineering opportunity for modulating epitope-specific T-cell activation. Analysis of the flanking sequences of highly presented T-cell epitopes has led to the identification of both natural and synthetic sequences that can either promote or inhibit the epitope presentation to T cells.[120,121] Additionally, oligoalanine residues flanking an epitope have been shown to increase the epitope presentation efficiency, possibly by providing a buffer from nearby interfering sequences.[119] Rueda *et al.* applied this concept when designing parvovirus-like particles to present an immunodominant CD8$^+$ T-cell epitope of chicken ovalbumin (OVA). By inserting an additional 3-5 aa of the natural OVA sequence flanking the epitope, the resulting parvovirus-like particles demonstrated considerable improvement of the epitope presentation compared to the OVA epitope alone.[122] In addition to epitope flanking sequences, the selection of T-cell epitopes themselves is challenging due to their dynamic nature. It is believed that the long-lasting protective memory T cells respond to only a few peptides derived from the pathogen, termed immunodominant epitopes.[123-125] However, the immunodominant epitopes can change depending on an individual's disease state,[126-128] and subdominant T-cell epitopes are also shown to be important in controlling viral replication.[129] To address this challenge, further cooperative advancements in high throughput T-cell epitope mapping,[130,131] disease pathology,[132,133] and personalized approaches in vaccine development[134] are required.

1.4. Engineering Influenza VLP for Vaccination

Influenza vaccines based on VLP present numerous advantages over conventional influenza vaccination approaches. Compared to production of influenza vaccine in chicken eggs, the recombinant methods employed to produce VLP in cell culture have increased production capacity, decreased production times, and do not require the need of egg adaption.[29,135] In addition, influenza VLP have been shown to elicit a better immune response than the conventional inactivated split influenza vaccines.[136] For these reasons, VLP have garnered significant interest in industry for development of next generation influenza vaccines. In this section we discuss the design considerations for the development of next generation influenza VLP vaccines to improve their immunogenicity and breadth of protection.

1.4.1.Enhancing T Cell Activation

While the particulate nature of VLP leads to efficient uptake by antigen presenting cells (APCs) for subsequent presentation to CD8 and CD4 T cells,[77,137] VLP often elicit weaker T-cell responses compared to viral infection due to the lack of additional stimuli presented by viral replication.[138,139] Yet, recent studies have suggested the necessity of targeting T cells in developing effective influenza vaccines. Cytotoxic CD8 T cells in particular play a critical role in the influenza immune response and have been shown to be a strong correlate of protection.[140-142] Furthermore, influenza specific T cells can provide cross protection against other influenza viruses due to their recognition of more conserved epitopes.[19,20] Therefore, enhancing the capability of VLP to induce strong T cell immune responses is of great interest.

The immunogenicity of vaccines is commonly tuned through the use of immunomodulatory agents known as adjuvants. Although not fully understood, studies have suggested that adjuvants improve vaccine efficacy partly by enhancing the activation and maturation of APCs, such as dendritic cells (DCs) and macrophages.[143] These activated APCs then induce the maturation of T cells and B cells that are crucial in adaptive immune responses and immunological memory.[144,145] It is well established that APC activation is frequently triggered by the recognition of pathogen-associated molecular patterns (PAMPs) by toll-like receptors (TLRs) expressed on the APC surface.[146] In addition to upregulating the expression of major histocompatibility complex (MHC) for enhanced antigen presentation to T cells, activated APCs provide a cytokine and chemokine microenvironment that supports strong antigen-specific cellular and humoral immune responses.[147] Therefore, TLR ligands and their synthetic analogs represent an attractive class of adjuvants that can enhance APC maturation, which in turn improves the activation of antigen-specific T cells.[148,149]

TLRs are activated by specific pathogen associated molecular patterns (PAMPs), which can be exploited as potential VLP adjuvants. Oligonucleotides (CPG DNA, ssRNA),[150-153] lipopeptides (E_8Pam_2Cys),[154] and bacterial peptides (flagellin)[88,155] are TLR agonists that have been introduced into VLP to significantly increase antigen specific T cell responses. In particular influenza VLP functionalized with flagellin have been shown to elicit greater antibody titers, enhanced T cell responses, improved cross-protection, and increased immunogenicity compared to VLP without flagellin.[156,157] Although T cell activation through TLRs is thought to primarily occur indirectly through the activation of APCs, there is increasing evidence that a range of T-cell subsets including cytotoxic CD8 T cells also express TLR2 and/or TLR5 on their surface, thus can be activated directly.[158-164] It should also be noted that molecules activating other immune signaling pathways that are independent of TLRs can also be displayed on VLP to enhance T-cell activation.[165,166] For instance, the activation of natural killer T cells by α-galactosylceramide (α-GalCer),[167] the activation of DCs by CD40L,[168,169] and VLP directly functionalized with supporting cytokines[170,171] have been shown to increase antigen-specific T-cell responses.

1.4.2. Increasing Heterosubtypic Protection

Antibodies generated by vaccination or infection are primarily targeted to the immunodominant head of the HA protein[14,15] where four antibody binding sites have been identified.[172] Due to their close proximity to the HA receptor binding site, antibody binding to these areas results in virus neutralization. However, these viral regions easily accommodate mutations through genetic drift, enabling the virus to escape neutralizing antibodies generated towards prior strains[14] and resulting in the need for annual vaccination. Thus, significant research has focused on targeting the immune response towards more conserved areas of the influenza virus that are less prone to mutation in order to provide protection against drifted strains as well as more genetically distant subtypes of influenza virus. To this end, several strategies have been investigated.

The M2 ion channel protein is highly conserved among influenza viruses. In particular, amino acids 1-9 of the M2 ectodomain (M2e) display >98% sequence homology among all known influenza viruses.[173] However, M2 is only weakly immunogenic during infection, with only a fraction of infected individuals producing M2 antibodies.[174] This is likely due to the low incorporation of M2 in influenza virions (~3% of total surface proteins)[5] as well as its concealment under the much larger HA and NA glycoproteins. Several studies have incorporated epitopes of M2e on the surface of several VLP carriers, resulting in strong antibody responses.[175] However, there is evidence that antibodies raised against these M2e epitopes do not bind well to influenza virus,[176] likely due to the inability of these epitope vaccines to mimic the tetrameric structure of the native M2 protein.[177] However, presentation of full-length M2 proteins incorporated into VLP without HA or NA was demonstrated to substantially increase the antibody response towards M2 and these antibodies were found to provide cross protection in mice challenged with H1N1, H3N2, and H5N1 subtypes.[178] While these results are promising, it should be noted that antibodies generated against M2 are non-neutralizing and therefore cannot prevent infection. Therefore, M2 is best used in conjunction with other strategies to mitigate the morbidity of influenza virus infection.

While the globular head of HA is prone to mutation, the stalk domain of HA is much more conserved. Although stalk reactive antibodies are not efficiently generated during infection, isolated antibody clones that do bind to the stalk region of HA have the ability to cross react with a large proportion of HA subtypes.[179] Therefore, designing vaccines that elicit stalk-reactive antibodies is a research priority. However, immunogenically presenting the stalk region in its native conformation has been a challenge. Two main strategies have emerged. In one strategy, "headless" HA proteins lacking the globular head domain are stabilized in their native conformation through numerous mutations.[180,181] Vaccination with these headless H1 proteins completely protected mice[180] or ferrets[181] from lethal heterosubtypic challenge with H5N1. Despite the achievement, the construction of these proteins required several complex design iterations and protection has only been demonstrated so far within group 1 HA proteins. Another approach is to sequentially vaccinate with HA proteins containing the same stalk domain but different head domains.[179] This strategy was inspired by the observation that infection or vaccination with H1N1 during 2009 preferentially generated broadly neutralizing antibodies towards the HA stalk.[182,183] Interim results from phase I clinical trials demonstrated that these chimeric HA proteins formulated into split or LAIV vaccines can induce high-titer cross reactive antibodies in humans.[184] However, relatively high levels of adverse events were reported (20-61% of participants) although most were mild.[184] Presentation of these proteins on VLP may allow these chimeric HA vaccines to retain their immunogenicity with reduced levels of adjuvant, making the vaccine more tolerable.

1.4.3. Recombinant Hosts for Producing Influenza VLP

A crucial consideration for producing any therapeutic protein is the choice of expression system. VLP can be produced by expressing structural and immunogenic proteins of a virus in either bacteria, yeast, insect, mammalian, or plant cells. The choice of the host system can have a significant impact on the yield and characteristics of the product, and each system has its advantages and disadvantages[185] (summarized in **Table 1.1**). Influenza VLP have been extensively described in higher organisms such as insect, mammalian, and plant cells.[186-188] These systems have produced influenza VLP that have protected mice or ferrets from challenges with lethal doses of influenza and are currently in clinical trials.[136,186,187] It is notable that the protein requirement for producing influenza VLP varies by expression system. In mammalian cells, VLP can be efficiently produced through expression of just HA, however the budded VLP remain attached to the cell surface due to HA's affinity for sialic acid unless NA is incorporated into VLP or exogenous NA is added.[189] In the plant cells of *Nicotiana benthamiana*, only HA is necessary for formation of VLP[186] since plants do not natively produce sialic acid.[190] In contrast, influenza VLP production in insect cells requires M1 in addition to HA as there are no reports of VLP being produced with HA alone.[191] Despite the ability to produce VLP with these minimal requirements it can also be advantageous to express additional influenza proteins. For example, the efficient incorporation of M2 into VLP can lead to M2 antibodies with the ability to provide cross protection.[178] In our lab, Zak et al. was able to engineer high density incorporation of M2 into influenza VLP produced in Sf9 insect cells through use of the of M2 ion channel inhibitor amantadine.[192]

For industrial production of recombinant proteins, it is often advantageous to utilize the most primitive host system possible. Despite the use of insect, mammalian, and plant cells to produce influenza VLP, these systems almost exclusively rely on the use of viral vectors for VLP production. Viral vectors require lengthy cloning procedures, amplification steps, and extra downstream purification that ultimately limit the throughput of these systems and extends the timescale for VLP production. On the other end of the spectrum, HA proteins produced in *Escherichia coli* are unrecognized by neutralizing antibodies suggesting that *E. coli* is incapable of producing HA in the correct conformation.[193] In contrast there is evidence that HA can be produced in yeast that is correctly folded and glycosylated.[194-200] Despite this, influenza VLP production in yeast has not yet been described.

Table 1.1. Recombinant hosts for influenza VLP production
Advantages and disadvantages of commonly used expression systems for the production of recombinant proteins. Cost, speed, scalability, yield, and complexity adapted from Lua *et al.*[185]

	E. coli	Yeast	Insect	Mammalian/Plant
Cost	$	$ $	$ $ $	$ $ $ $
Speed	+ + + +	+ + +	+ +	+ +
Scalability	+ + + +	+ + +	+ +	+ +
Yield	+ + + +	+ + +	+ +	+
Complexity	+	+ +	+ + +	+ + + +
Produce HA?	X	✓	✓	✓
Produce VLP?	X	?	✓	✓

1.5. Project Overview

The development of a universal influenza vaccine that can provide long-lasting protection against diverse influenza subtypes for all demographics is incredibly challenging and such a vaccine has eluded researchers for decades. While there are many promising influenza vaccine concepts, experimental therapeutics have a historically high risk of failure in clinical trials. It currently takes an average of $1 billion and 10-20 years to bring new therapeutics to market.[201] Furthermore, previous work has demonstrated that broadly protective influenza vaccines require extensive engineering of the vaccine immunogen beyond the simple presentation of native influenza proteins to elicit strong and durable protection.[179-181] To meet these challenges, new technologies are needed to expedite influenza vaccine synthesis, engineering, and pre-clinical testing. VLP represent optimal immunogens for next generation vaccines as they are inherently immunogenic and highly tunable through either chemical or genetic modification to enhance their properties.[98] However, influenza VLP production has so far been limited to higher eukaryotic hosts, limiting the speed that influenza VLP candidates can be produced, engineered, and evaluated. To this end, this thesis describes the development of a new platform for rapid prototyping and testing of influenza VLP candidates.

In **Chapter 2**, we describe the production of influenza VLP in a new recombinant host: *S. cerevisiae.* Compared to recombinant protein production in insect, mammalian, and plant cells, recombinant protein production in the yeast *S. cerevisiae* is generally faster, higher yielding, and less expensive.[185] Furthermore, *S. cerevisiae* has well-established tools for rapid genetic manipulation. When this is combined with the immunogenicity and tunability of VLP, the result is a rapid system for developing and engineering VLP-based influenza vaccines. However, whether *S. cerevisiae* can support influenza VLP production has not yet been reported. While we demonstrate that *S. cerevisiae* supports the expression of full-length and glycosylated influenza HA proteins from diverse influenza subtypes, we discovered that HA does not efficiently traffic to the yeast plasma membrane where VLP formation presumably takes place. Importantly we were able to engineer plasma membrane localization of HA by fusing a fluorescent protein to its C-terminus. Expression of M1 and this mutant HA resulted in production of influenza VLP that possessed functional characteristics of influenza virus, including the ability to agglutinate red blood cells and undergo endocytosis, demonstrating for the first time the ability to produce influenza VLP in a lower eukaryotic host.

In order to permit the rapid engineering of these yeast VLP strains for enhanced VLP yield and immunogenicity, high-throughput methods for detecting and quantifying influenza protein expression in yeast cells are essential. **Chapter 3** describes the development and validation of a high-throughput strategy for detecting intracellular and plasma membrane proteins such as HA and M1 in yeast. This approach – which we have termed yeast intracellular staining (yICS) – enables detection of proteins residing on the plasma membrane and in intracellular compartments following removal of the yeast cell wall by fluorescent antibody staining. Quantitative protein expression in single cells is then obtained by flow cytometry analysis. After validating the ability of yICS to detect endogenous intracellular yeast proteins, we demonstrate that yICS can detect multiple recombinant proteins simultaneously. As a proof of concept, we then applied yICS to screen libraries of multicopy integration clones containing different copy numbers of a target protein. yICS efficiently identified rare (~1%) high copy clones that resulted in ~8-fold increase in target protein yield. This yICS tool in combination with the yeast influenza VLP system will enable rapid prototyping of influenza VLP formulations by aiding in characterization and identifying high producing clones.

While Chapters 2 and 3 establish a rapid pipeline for VLP production and engineering, it is necessary to establish methods of evaluating the immune response towards these VLP. In **Chapter 4**, we assess the ability of mass cytometry (CyTOF) for this purpose by applying CyTOF to interrogate the immune response to influenza virus infection in the mouse lung. CyTOF enabled detection of 40 markers on single cells, providing detailed information on cellular phenotype, activation status, cytokine production, and expression of influenza proteins. To aid in the analysis of such a large and high-dimensional dataset, we developed an automated supervised learning approach to classify cells into one of 24 highly specific immune cell subsets. Analysis of the resulting data provide a high-resolution view of the early inflammatory response to influenza virus infection and its transition towards adaptive immunity and tissue repair. In addition to identifying anticipated changes in immune cell populations that validate the CyTOF approach, the high-resolution dataset provides new insight into *in vivo* cytokine production, the susceptibility of immune cells to viral infection and replication, and defects associated with the aging immune system. This study demonstrates the power of high-dimensional single cell analysis for evaluation of the immune response and lays the groundwork for the future evaluation of VLP vaccines.

Chapter 2. Production of Influenza VLP in *Saccharomyces cerevisiae*

2.1. Publication and Patent Information

Hill, B. D., Zak, A. J., Rizvi, S. M., Ponnandy, P., and Wen, F. Engineering Yeast *Saccharomyces cerevisiae* for Assembly of Enveloped Influenza Virus-Like Particles. (*In Prep*)

Wen, F., Khera, E., Hill, B. D., Rizvi, S. M. Virus-like Particles. U.S. Patent Application 15/566,069. 2020.

The goal of this chapter is to test the feasibility of influenza VLP production in the lower eukaryote *Saccharomyces cerevisiae.* Accomplishing this goal has the potential to greatly expedite the production and engineering of influenza VLP vaccines. Dr. Syed Monem Rizvi assisted with VLP synthesis, cloning, and immunogold labeling. Andrew Zak performed the endocytosis assay and IMAC purification. Dr. Prabhu Ponnandy assisted with multicopy integration and subsequent screening for high copy integration events.

2.2. Abstract

Current influenza vaccines produced in chicken eggs have several drawbacks including moderate efficacy, long production timelines, and susceptibility to egg shortages. Influenza virus-like particles (VLP) have emerged as a promising alternative vaccination approach due to their

enhanced immunogenicity, tunability, and ability to be produced by recombinant methods in cell culture. While influenza VLP have been successfully produced in mammalian, plant, and insect cells, the ability of lower eukaryotic hosts to produce influenza VLP has not been reported despite potential advantages of reduced cost, faster production, and easier scale up. To this end, we investigated the feasibility of influenza VLP production in the yeast *Saccharomyces cerevisiae.* We demonstrate that *S. cerevisiae* supports the production of full-length influenza hemagglutinin (HA) and M1 proteins from diverse influenza subtypes H1N1, H3N2, and H7N9. Further analysis revealed that HA is not efficiently transported to the plasma membrane where influenza VLP formation takes place, indicating a defect in HA processing along the secretory pathway. Importantly, fusion of a fluorescent protein to the C-terminus but not the N-terminus of HA removed the defect, improving plasma membrane localization of HA dramatically. Following cell wall removal, fluorescent nanoparticles could be detected in the supernatant of cells expressing this mutant HA and M1 by nanoparticle tracking analysis (NTA). Transmission electron microscopy (TEM) further revealed that these lipid nanoparticles could be densely stained with anti-HA antibody, confirming for the first time the formation of influenza VLP in yeast. Notably, these VLP also displayed key functional characteristics of influenza virus as demonstrated by their ability to agglutinate red blood cells, bind MDCK cells in a sialic acid dependent manner, and undergo endocytosis. Combined with the versatility and speed of recombinant protein production in *S. cerevisiae*, this novel yeast-based influenza VLP production platform can enable rapid engineering and prototyping of next generation influenza vaccines.

2.3. Introduction

Seasonal influenza infection kills between 290,000 – 650,000 individuals per year[2] and continues to be a global health concern. While vaccination remains the most effective approach for preventing the spread of influenza virus, the effectiveness of influenza vaccines is highly variable from year to year, ranging from 19-60%.[202] This inconsistent efficacy can be partially attributed to the long-standing practice of manufacturing the vaccine in embryonated chicken eggs, a process whose long (6+ month) manufacturing timeline and requirement for egg adaptation often leads to mismatches between circulating strains and vaccination strains.[29] However, vaccine efficacy is still surprisingly modest even in low risk individuals when there is a good match between vaccine strains and circulating strains.[203] Perhaps most concerning is the lack of protection in individuals over the age of 65, who have difficulty generating protective immune responses from influenza vaccination and consequently account for 70 – 90% of all influenza related deaths.[204] This marginal performance highlights the need for improved influenza immunogens that generate a more protective immune response as well as alternative manufacturing methods that do not rely on eggs.

Influenza vaccines based on virus-like particles have garnered significant attention as next generation influenza vaccines. Virus-like particles (VLP) are nanoscale biological structures consisting of viral proteins assembled in a morphology that mimics the native virion but do not contain the viral genetic material. The possibility to manipulate the proteins contained within VLP makes them an attractive tunable system for synthesizing predictable nanoscale structures that have numerous applications including drug delivery and biocatalysts.[98] However, VLP are especially amenable to vaccine development due to their presentation of authentic viral proteins to the immune system in their near-native conformation without risk of infection.[98] In fact, the FDA has approved VLP-based vaccines for human papilloma[205] and hepatitis B[206] viruses, and clinical trials for several other vaccines containing VLP are currently underway.[207]

Aside from their immunogenicity and safety, VLP vaccines are synthesized in cell culture, which, compared to egg production, increases production capacity, decreases production times, omits the need for egg adaption, and avoids the handling of infectious virus.[29,135] Specifically, influenza VLP have been successfully produced in insect, mammalian, and plant cells[186-188] that protect mice or ferrets from lethal influenza challenge.[136,186,187] While influenza VLP made in these higher eukaryotic hosts show great promise, it is often advantageous to express recombinant proteins in the most primitive host system possible in order to produce high yields while minimizing cost. Several reports demonstrate that full length[194] or truncated[195,199,200] influenza surface protein hemagglutinin (HA) can be produced in the lower eukaryotes *Saccharomyces cerevisiae* or *Pichia pastoris*. Despite this evidence, the capability of yeast to produce influenza VLP has not been previously described. A yeast-based production system for influenza VLP would have several potential advantages. First, high expression of multi-protein complexes in insect, mammalian and plant systems requires the use of viral vectors, necessitating lengthy cloning approaches and complex purification methods to separate the viral vectors from the VLP.[208] On the other hand, multiple gene constructs can be highly expressed from endogenous promoters in yeast after a single cloning step, enabling faster production timelines without viral vector contamination. Additionally, recombinant protein production in yeast is often higher yielding, less expensive, more scalable, and more robust than production in insect, plant, or mammalian cell systems.[185]

In this work, we explore the production of influenza VLP in *S. cerevisiae*. Notably, we demonstrate that *S. cerevisiae* has the capability to express full length HA and M1 protein from diverse influenza subtypes, and the co-expression of HA and M1 leads to detectable levels of these proteins in cell supernatants following removal of the yeast cell wall. Further investigation reveals a defect in HA processing along the secretory pathway that prevents efficient localization of HA to the yeast plasma membrane. We further demonstrate that the fusion of a fluorescent protein to the C-terminus of HA dramatically enhances plasma membrane localization and significantly increases VLP yield. Resulting VLP demonstrated functional characteristics of influenza virus including the ability to agglutinate red blood cells and to be internalized by mammalian cells in a sialic-acid dependent manner *in vitro*. Taken together, these data demonstrate that yeast is capable of producing functional influenza VLP, laying the groundwork for a new influenza vaccination platform and opening the door for yeast based VLP production of other enveloped viruses.

2.4. Results and Discussion

2.4.1. S. cerevisiae Can Express HA and M1 Proteins from Diverse Influenza Subtypes

Co-expression of the influenza HA glycoprotein and the M1 matrix protein leads to influenza VLP formation in higher eukaryotes.[191] To determine if *S. cerevisiae* has the capability to express these essential viral proteins, HA and M1 proteins from strains H1N1 A/Puerto Rico/1934, H3N2 A/Aichi/2/1968, and H7N9 A/Shanghai/MH01/2013 strains were cloned into the high-copy pRS426 plasmid under control of the strong *Gal10* and *Gal1* galactose-inducible promoters (**Figure 2.1A**). Following galactose induction, yeast cell lysates were analyzed by Western blot with strain-specific antibodies (**Figure 2.1B,** lanes labeled "Yeast") alongside commercially available HA and M1 standards produced in Sf9 insect cells (**Figure 2.1B**, lanes labeled "Sf9"). Detectable protein bands were observed for all yeast constructs in the expected size range of 62 kDa for HA and 28 kDa for M1, demonstrating successful translation of all full-length proteins in *S. cerevisiae* (**Figure 2.1B**). Notably, multiple HA bands could be detected in lanes loaded with yeast lysates, demonstrating that HA multimers are being formed. However, there are observable differences between Sf9- and yeast-produced HA proteins. Two bands approximately 5-10 kDa apart are observed for yeast-derived H1 and H7 proteins whereas Sf-9 produced HAs have a clean single band. Furthermore, yeast derived H3 is approximately 20 kDa lower than its Sf9 counterpart.

Discrepancies in the size of recombinant proteins produced in different hosts are often the result of differences in glycosylation. N-glycosylation is an essential post-translational modification that promotes proper folding, intracellular transport, and stability of HA.[209-211] Upon incubation of cell lysates with PNGaseF, an enzyme that cleaves oligosaccharides from N-linked glycosylation sites,[212] yeast HA proteins had increased electrophoretic mobility compared to mock-treated HA proteins (**Figure 2.1C**), demonstrating that yeast HAs are glycosylated. In addition, the two bands observed for yeast produced H1 and H7 proteins prior to PNGaseF treatment collapsed into a single band upon incubation with PNGaseF, indicating that the lower band likely represents an unglycosylated intermediate form of HA. Furthermore, the shift in molecular weight of yeast derived H1 (**Figure 2.1C**, top) and H7 (**Figure 2.1C**, bottom) were of similar magnitude to their Sf9 counterparts, indicating a similar extent of glycosylation for these proteins in both hosts. In contrast, the shift in molecular weight for H3 was much greater in Sf9 than in yeast (**Figure 2.1C**, middle), indicating that yeast and Sf9 vary in their glycosylation behavior of this protein. Indeed, it is well known that *S. cerevisiae* possesses more primitive glycosylation machinery compared to higher eukaryotes, often resulting in hyper-glycosylation of mammalian-derived glycoproteins.[213] Although only three strains of HA were analyzed, it is reassuring the yeast-produced HA proteins from the chosen strains were not subject to this effect, which often negatively affects protein function.[214] Taken together, these results demonstrate that *S. cerevisiae* possesses the capacity to produce full length, glycosylated HA protein from genetically diverse influenza subtypes, however the extent of glycosylation for some subtypes may differ from those produced in higher eukaryotes. These results build on a previous evidence that full length and glycosylated H1 from H1N1 A/WSN/33 virus can be successfully produced in *S. cerevisiae*.[194] In addition, we are the first to report the successful expression of M1 proteins in *S. cerevisiae* to our knowledge.

Next, the yield of cellular HA expression was estimated using Western blot by comparison to commercial standards (**Appendix A.1**). H1 expression levels were more than 2-fold higher than H3 expression levels ($p < 0.01$) and more than 5-fold higher than H7 expression levels ($p < 0.001$). Due to its high expression level, we were also able to confirm trimer formation in the H1 construct (**Appendix A.2**), a critical processing step believed to occur in the endoplasmic reticulum immediately prior Golgi transport in mammalian cells.[215] While a small sample size, we noted that HA proteins with higher expression level correlated with a lower pH reported for HA-mediated membrane fusion in the literature.[216] While the induction media was buffered to pH 7.6 in this study to promote HA stability, these data suggest that increasing the acid tolerance of HA or increasing intracellular pH may further improve HA expression level. Regardless, the construct expressing H1 and M1 from A/Puerto Rico/1934 (hereafter referred to as H1M1) was chosen for further experimentation based on its high expression level (**Figure 2.1D**), confirmed trimerization (**Appendix A.2**), and similar glycosylation pattern to the H1 Sf9 standard (**Figure 2.1C**, top).

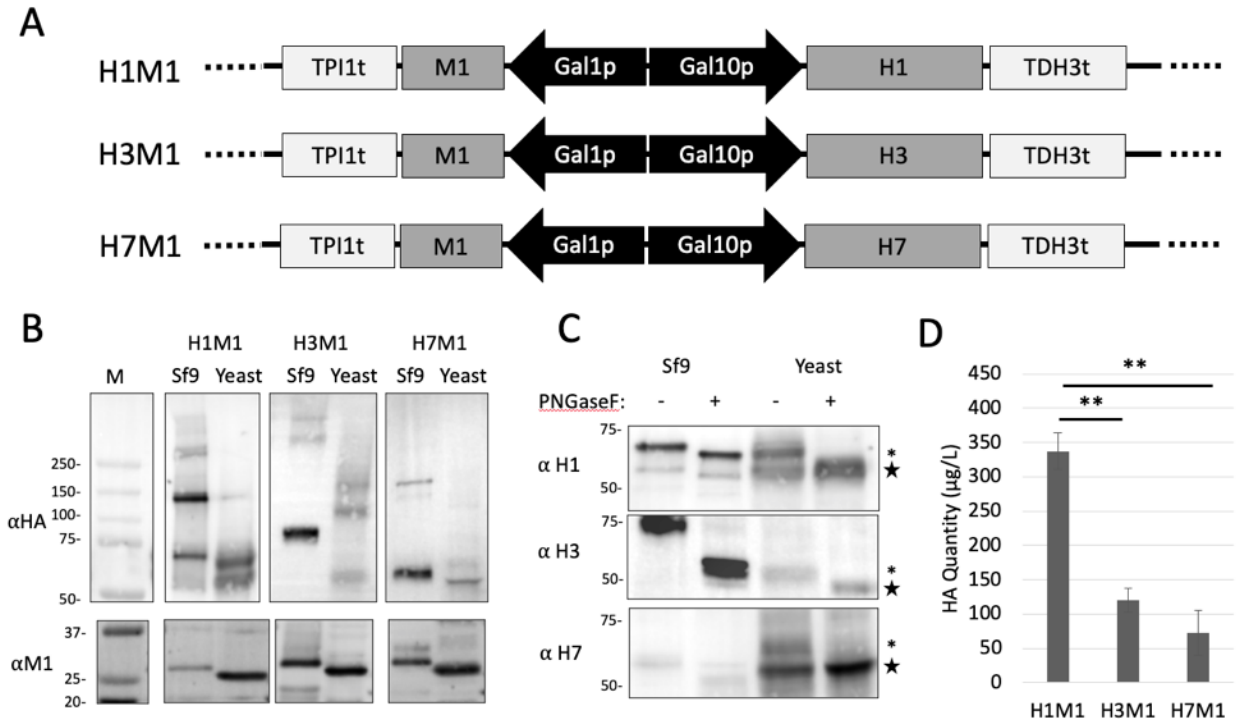

Figure 2.1. Expression of influenza HA and M1 proteins in *S. cerevisiae*

(**A)** HA and M1 proteins from strains H1N1 A/Puerto Rico/1934, H3N2 A/Aichi/2/1968, and H7N9 A/Shanghai/MH01/2013 were cloned into plasmids under control of *Gal10* and *Gal1* galactose-inducible promoters. (**B**) Western blot analysis of yeast cell lysates and Sf9 protein standards shows expression of full-length HA (~62kDa) and M1 (~28 kDa) proteins. (**C**) PNGaseF digestion decreases molecular weight of HA, indicating successful glycosylation in yeast. Asterisks denote glycosylated HA and stars denote deglycosylated HA. (**D**) Quantification of different HA subtypes in yeast cell lysates. Data represent mean ± standard error of the mean (SEM), $n = 2$; statistical comparisons computed by one-way ANOVA followed by post hoc Tukey's pairwise comparisons, $*p < 0.05$, $**p < 0.01$, $***p < 0.001$.

2.4.2. Integration Improves Intracellular and Extracellular Yield of H1 and M1 Proteins

While H1 had the highest expression level of all three constructs (~300 ug/L, **Figure 2.1D**), the overall yield is relatively low compared to the cellular expression level of the same HA protein in Sf9 (~10-20 mg/L).[192] To enhance overall yield, we performed multiple rounds of genomic integration of the H1M1 expression cassette into the yeast genome (see methods). Consecutive rounds of integration yielded increasing copy numbers as determined by quantitative PCR (qPCR), with approximately 13 copies being introduced after three rounds (**Figure 2.2A**). The expression levels of H1 and M1 over the course of integration were compared by Western blot of cell lysates (**Figure 2.2B**), revealing a dramatic increase in the expression levels of H1 and M1 in agreement with the qPCR results. Notably, the unglycosylated lower band of H1 became very prominent in the third integration strain (**Figure 2.2C**, top), suggesting that the functional throughput of the yeast secretory pathway had likely been exceeded. Nevertheless, the quantity of the upper, glycosylated HA band increased nearly 10-fold over the plasmid strain to approximately 3 mg/L (**Figure 2.2C, Appendix A.3**).

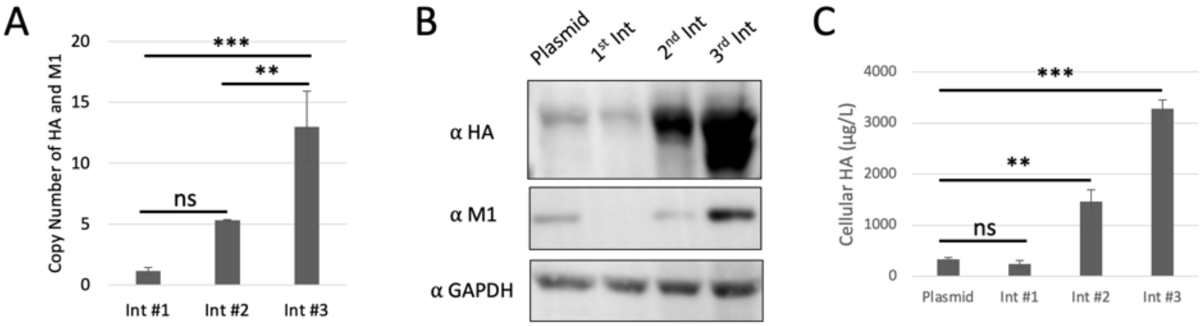

Figure 2.2. Integration of H1 and M1 enhances their cellular yield
(**A**) qPCR analysis of three consecutive integration rounds results in increases in genomic copy number of H1 and M1 proteins ($n = 3$). (**B**) Integration of HA and M1 expression cassette results in improved cellular expression of H1 and M1 proteins. (**C**) Western blot quantification indicates nearly 10-fold increase in cellular expression of H1 and M1 proteins in the 3rd integration strain (Int #3) compared to plasmid-based expression ($n = 2$). Data in (A) and (B) represent mean ± SEM; statistical comparisons computed by one-way ANOVA followed by post hoc Tukey's pairwise comparisons, *ns* p > 0.05, *$p < 0.05$, **$p < 0.01$, ***$p < 0.001$.

To gain more detailed insight into the differences in protein expression between the strains, we performed yeast intracellular staining (yICS). Developed in **Chapter 3**, the yICS technique enables intracellular proteins to be detected by flow cytometry following fluorescent antibody staining. Compared to Western blotting, yICS permits protein expression level to be detected in individual cells, allowing variation in protein expression level to be observed across a population.

yICS analysis revealed that the integrated strains had a relatively homogeneous distribution of H1 and M1 expression that increased with subsequent rounds of integration (**Figure 2.3**). On the other hand, the plasmid strain had a distinctly bimodal distribution with the positive population having a similar expression of H1 and M1 compared to the 3rd integration strain. These results reveal, counterintuitively, that the lower H1 yield in the plasmid strain observed by Western blot (**Figure 2.2B**) is due to the presence of a large population of non-expressing cells rather than a lower expression level in all cells.

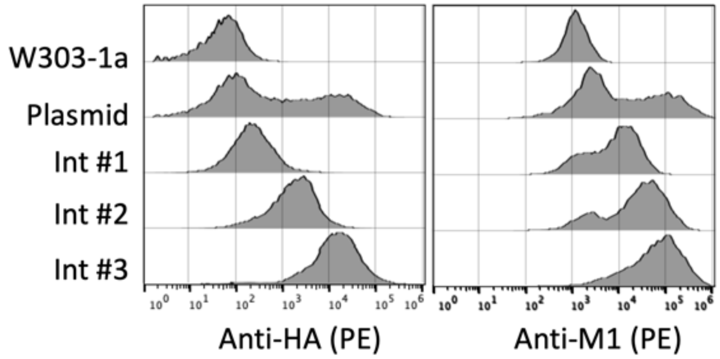

Figure 2.3. Detection of HA and M1 by yeast intracellular staining (yICS)
Flow cytometry of yeast cells stained with anti-H1 and anti-M1 antibodies followed by a fluorescently labeled secondary antibody (phycoerythrin (PE)). Integrated strains (Int) demonstrate a homogeneous expression pattern while the plasmid strain's staining profile is bimodal. HA and M1 increase with subsequent rounds of integration. W303-1a is the parent strain.

Following the increase in protein expression level of the H1 and M1 proteins by integration, we investigated if *S. cerevisiae* could support the production of influenza VLP. Influenza virus and VLP formation occurs on the plasma membrane in a process known as budding, however this budding process is inhibited in *S. cerevisiae* by its cell wall. As a solution to this problem, Morikawa *et al* demonstrated that removal of the cell wall through enzymatic treatment resulted in the budding of enveloped HIV-gag VLP following expression of the HIV-1 gag polyprotein in *S. cerevisiae*.[217] We were curious if such an approach could lead to the formation of influenza

VLP. Accordingly, both plasmid and integrated H1M1 constructs were induced, subjected to enzymatic cell wall removal to form spheroplasts, and then incubated overnight in osmotically stabilized media to allow the budding process to take place (**Figure 2.4A**). The supernatant was then harvested, subjected to 10,000 × g centrifugation to remove cell debris, and HA quantification was performed by Western blot (**Figure 2.4B**). Indeed, HA protein could be detected in the supernatant of all constructs, indicating that VLP formation could be taking place. HA yield in the supernatant (**Figure 2.4B**) directly mirrored cellular HA expression (**Figure 2.2C, Appendix A.3**), with the 3rd integration strain achieving a 6.5-fold improvement in extracellular HA yield compared to the plasmid strain ($p < 0.001$). These results reveal that increases in HA yield can be efficiently achieved *via* integration. Moreover, HA cellular and extracellular yields are almost directly proportional to the number of protein copies (**Figure 2.2A**), indicating that more integration rounds can likely drive further increases in protein expression level.

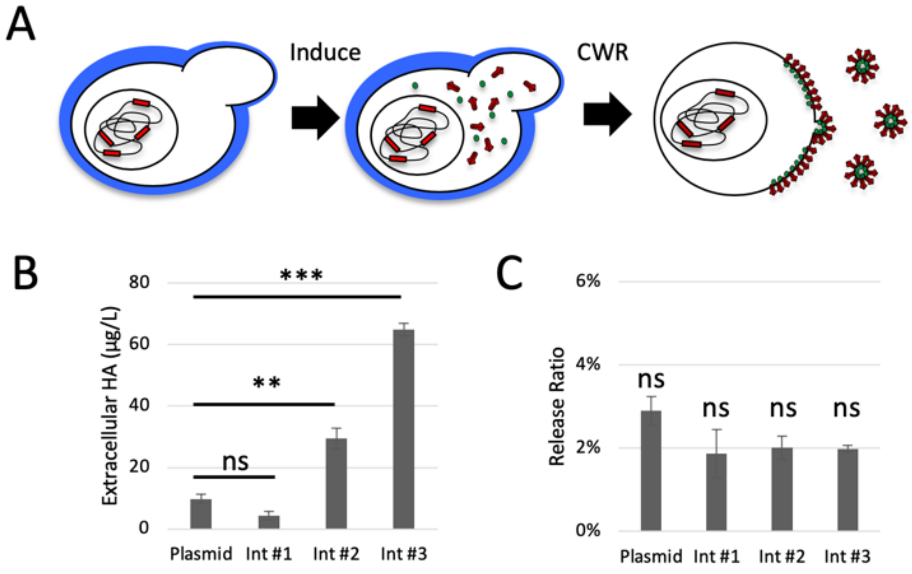

Figure 2.4. Detection of H1 and M1 proteins in yeast supernatants
(**A**) Influenza VLP procedure: yeast cells containing the H1M1 expression cassette are induced in galactose followed by cell wall removal (CWR). Cells are incubated overnight in osmotically stabilized media to allow for budding of influenza VLP. The supernatant is then harvested,

clarified by 10,000 x g centrifugation, and used for further analysis. (**B**) Western blot quantification of H1 in yeast supernatants. Integration improves yield 6.5-fold over plasmid expression. (**C**) Extracellular HA yield was divided by cellular HA yield to derive the release ratio. There is no significant difference in release ratio for any construct. Data in (B) and (C) represent mean ± SEM, $n = 2$; statistical comparisons computed by one-way ANOVA followed by post hoc Tukey's pairwise comparisons, $^*p < 0.05$, $^{**}p < 0.01$, $^{***}p < 0.001$.

We next compared the efficiency of VLP formation among the H1M1 strains by calculating the ratio of extracellular HA yield to cellular HA yield (hereafter referred to as the release ratio). Interestingly, there was no significant difference in the release ratio for any of the constructs (**Figure 2F**), with all constructs possessing a release ratio of approximately 2%. In comparison, the production of HIV gag particles in *S. cerevisiae* resulted in a release ratio of ~50%.[217] While these results conclusively show that large increases in H1 and M1 yields can be achieved by multicopy integration, the low release ratio suggests an additional defect in influenza VLP formation.

2.4.3. HA Fused to C-terminal Fluorescent Protein Enhances Plasma Membrane Targeting

As a first step towards identifying bottlenecks in VLP formation, we investigated the cellular localization of HA. To this end, we performed confocal microscopy on yeast spheroplasts expressing the H1M1 plasmid. Spheroplasts were fixed in 4% formalin, permeabilized with saponin, and stained with an anti-H1 antibody followed by a fluorescently labeled (AF647) secondary antibody. Images of cellular cross sections revealed that HA signal was predominantly intracellular (**Figure 2.5**), indicating that HA is not efficiently localizing to the plasma membrane. As HA plasma membrane localization is critical for influenza virus and VLP formation in higher eukaryotes,[5,6,218,219] increasing plasma membrane localization has the potential to greatly improve VLP budding efficiency (release ratio) and overall VLP yield.

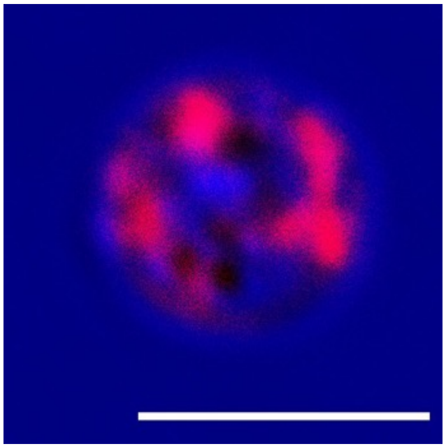

Figure 2.5. Confocal microscopy reveals inefficient plasma membrane localization of HA Representative confocal microscopy image of yeast spheroplasts expressing H1 and M1 proteins. Cells were labeled with anti-HA antibody followed by a fluorescent secondary antibody (AF647). This single focal plane image through the center of the cell indicates that HA signal is predominantly intracellular with very little plasma membrane localization. Scale bar is 5 µm.

To enable the cellular localization of HA to be readily determined without the need for intracellular antibody staining, we fused mUkg1 – a 25 kDa green fluorescent protein derived from a soft coral[220] – to either the N- or C-terminus of HA. The fluorescent protein mUkG1 was chosen due to reports of greater brightness and expression level in *S. cerevisiae* compared to green fluorescent protein (GFP) and its derivatives.[221] To ensure proper targeting of HA to the secretory pathway, the C-terminal mUkG1 was placed after the HA signal sequence. The N and C terminal HA fluorescent fusions – which will be denoted as FC and FN, respectively – were cloned in place of HA in the H1M1 plasmid to create plasmids FNM1 and FCM1, respectively (**Figure 2.6A**).

To verify successful expression of the fusion constructs, cells harboring plasmids H1M1, FCM1, or FNM1 were subjected to the VLP protocol (**Figure 2.4A**), and HA and M1 expression levels in cell lysates and cell supernatants were assessed by Western blot (**Figure 2.6B**). Compared to wild-type (WT) HA, the FC and FN fusion proteins possessed higher molecular weight, as expected. While statistically significant, differences in cellular expression levels between the constructs were small, with FC and FN expression levels within 30% of WT (**Figure 2.6C**). In contrast, Western analysis of the cell supernatants revealed that the quantity of FC was ~3 times greater than both FN ($p < 0.001$) and WT ($p < 0.01$) whereas the difference between WT and FN was not significant (**Figure 2.6D**). As a result, FC had ~2.5 times greater release ratio compared to WT and FN ($p < 0.01$, **Figure 2.6E**).

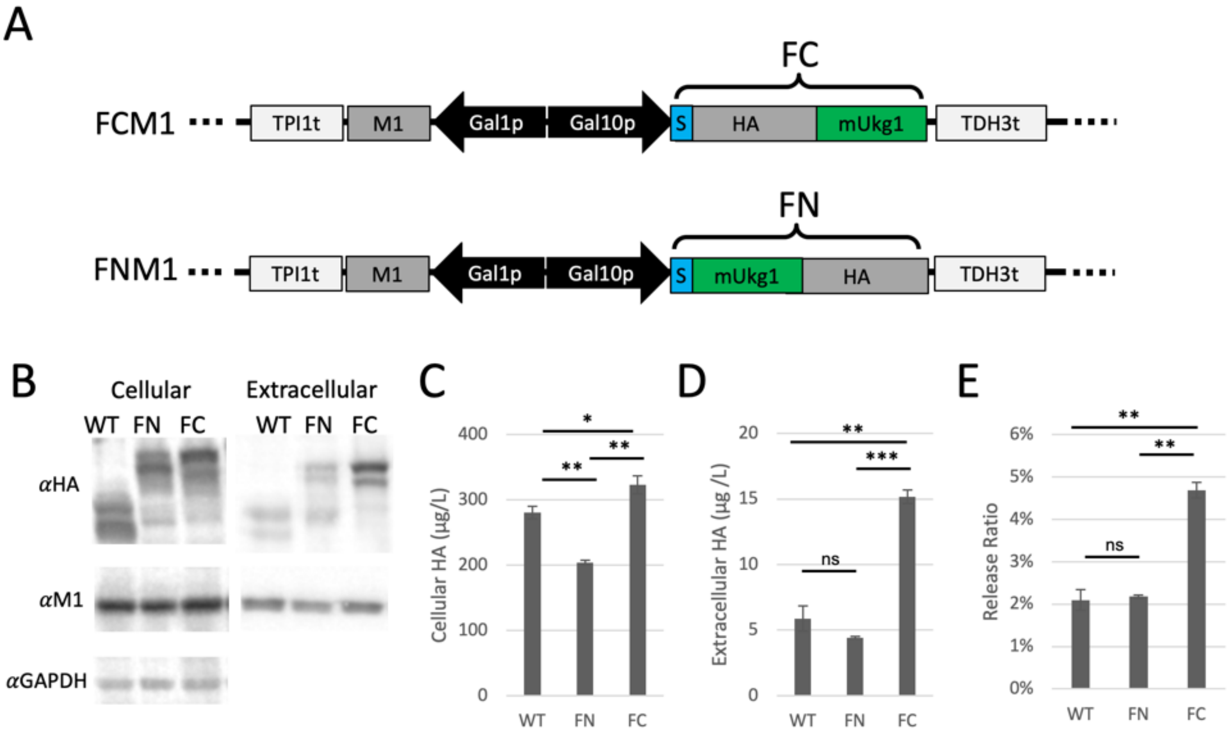

Figure 2.6. HA with C-terminal fluorescent fusion has improved release ratio
(**A**) FCM1 and FNM1 plasmids contain HA protein fused to fluorescent protein mUkg1 on the N- or C- terminus, respectively. The C-terminal fusion is after the HA signal sequence (denoted S). (**B**) Western blot of yeast cell lysates and supernatants expressing WT, FN, or FC HA proteins along with M1. FC demonstrates higher HA yield in the supernatant. HA was quantified in the cell lysates (**C**) and cell supernatants (**D**). The release ratio of the three constructs indicates ~2.5-fold improvement for FC. Data represent mean ± SEM, $n = 2$; statistical comparisons computed by one-way ANOVA followed by post hoc Tukey's pairwise comparisons, $*p < 0.05$, $**p < 0.01$, $***p < 0.001$.

Given the unexpected improvement in the release ratio, we investigated whether FC demonstrated improved plasma membrane targeting. To this end, we again performed HA intracellular staining as described previously followed by imaging of cellular cross sections by confocal microscopy. Whereas FN localization (**Figure 2.7**, upper left) was indistinguishable from WT (**Figure 2.5**), the FC construct demonstrated clear plasma membrane targeting (**Figure 2.7**, upper right). As fixation and permeabilization can possibly alter cellular morphology, we also performed live cell imaging of yeast spheroplasts and detected HA protein *via* the native mUkg1 signal. Again, the FC construct demonstrated clear plasma membrane targeting in contrast to the FN construct (**Figure 2.7**, bottom).

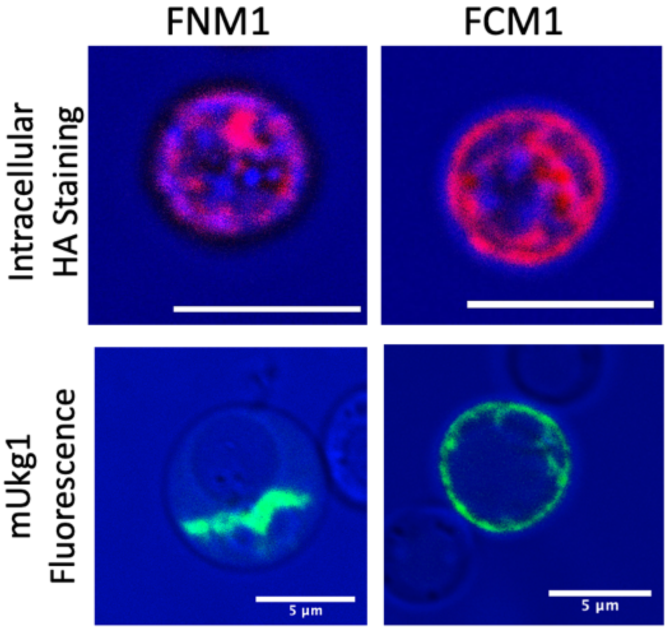

Figure 2.7. HA with C-terminal fluorescent fusion has improved plasma membrane targeting Confocal imaging of yeast spheroplasts expressing FNM1 and FCM1. Spheroplasts were either stained with anti-HA antibody (top) or viewed by live cell imaging (bottom) using native mUkg1 fluorescence. All scale bars are 5 µm (intracellular staining procedure reduces cell size).

In light of the notorious difficulties encountered when expressing mammalian glycoproteins in lower eukaryotes,[213,222-227] it is noteworthy that we were able to engineer such a stark change in glycoprotein localization. The mechanism resulting in improved plasma membrane targeting of FC is unclear. Recombinant protein fusions, especially with maltose binding protein (MBP), are commonly used to improve the folding of recombinant proteins expressed in bacteria[228] and even yeast.[229] However, the vast majority of these fusion partners are on the N-terminus because it is generally understood that this location is most effective.[228] Why a C-terminal fusion with HA is able to achieve plasma membrane localization in our case is unknown and warrants further investigation.

2.4.4. HA Fused to C-terminal Fluorescent Protein Results in VLP Formation

Next, we investigated whether the high release ratio oberved for FC results in influenza VLP production. To this end, we performed nanoparticle tracking analysis (NTA), a technology that is able to visualize and quantify nanoparticles in a flow cell using laser diffraction.[230] Aside from the ability to count total nanoparticles, the use of appropriate optical filters enables NTA to enumerate fluorescent particles containing the mUkg1 flurophore, allowing VLP to be visualized separately from contaminating yeast extracellular vesicles. To this end, clarified supernants from H1M1, FNM1, and FCM1 constructs were subjected to NTA analysis, and multiple 60 s videos were recorded as particles flowed through the laser beam. Strikingly, numerous brilliant particles were observed in the supernatant of the FCM1 construct (**Figure 2.8A**) but not in the FNM1 construct or in the H1M1 negative control (no fluorescence). When all video frames are combined into a single image using a maximum intensity projection, total particle "streaks" can be clearly observed, further revealing the numerous particles in the FCM1 construct (**Figure 2.8A**). Indeed quantification of total particles revealed that FCM1 had ~2 times more fluorescent particles compared to FNM1 ($p < 0.01$) and ~4 times more particles than the H1M1 background ($p < 0.001$) (**Figure 2.8B**). These results indicate that expression of FCM1 results in production of nanoparticles containing HA protein, demonstrating for the first time the successful production of infleunza VLP in yeast.

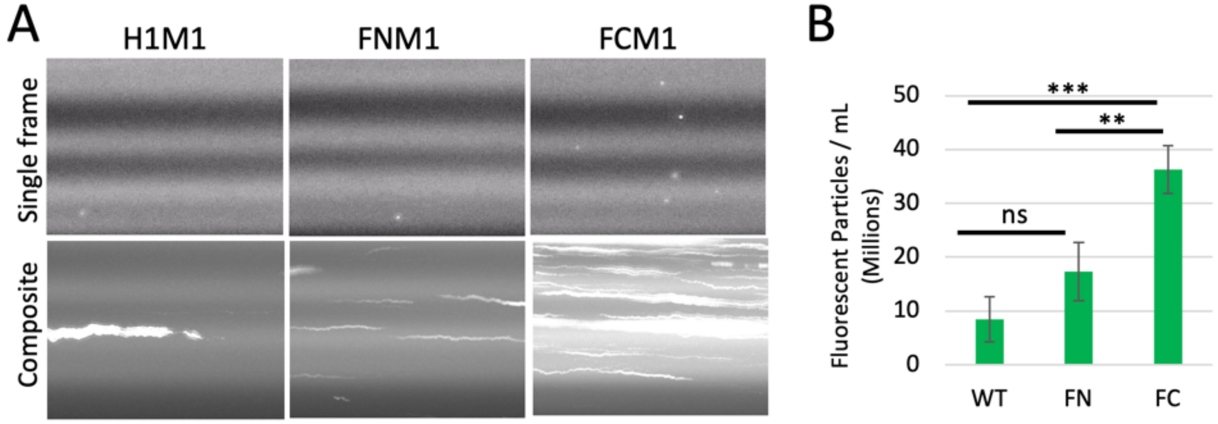

Figure 2.8. NTA analysis of yeast FCM1 supernatant reveals fluorescent nanoparticles
(**A**) Top: single frame of 60 s video acquired by nanoparticle tracking analysis (NTA) reveals numerous fluorescent FCM1 VLP compared to FNM1 and H1M1. Bottom: composite of all frames from 60 s video reveals all particle "streaks" over video duration. (**B**) Concentration of fluorescent particles quantified by NTA. Data represent mean ± SEM, $n = 3$; statistical comparisons computed by one-way ANOVA followed by post hoc Tukey's pairwise comparisons, *$p < 0.05$, **$p < 0.01$, ***$p < 0.001$.

To aid in the purification of yeast infleuzna VLP, a 10×His tag was added to the N-terminus of FC. No discernable difference could be observed between the expression of His-tagged FC and unmodified FC other than the ability of anti-His antibody to bind His-tagged FC by Western blot (**Appendix A.4**). His-tagged FCM1 (further denoted HisFCM1) supernatants were subjected to immobilized metal affinity (IMAC) on a nickel column and eluted with increasing concentrations of imidazole (**Figure 2.9A**). The majority of the loaded HA and M1 eluted in the flow through and with lower imidazole concentrations, perhaps due to steric hinderances that limit access to the N-terminal His tag at the base of the HA protein. Speicifcally the total yield of HA in the 100 mM, 250 mM, and 500 mM combined fracations is ~0.3 μg/L as opposed ~21 μg/L before purifcation (**Appenidx A.6**). In addition, there is no local maxima in the elution profile, suggesting that the

VLP are a heterogeneous mixture with a range of binding affinities. Furthermore, the similar elution profile of HA and M1 indicates their colocalization. Colocalization of HA and M1 was also corroboarated by immunoprecipitation (**Appendix A.7**). NTA analysis of the fractions eluted with 100 mM, 250 mM, and 500 mM of imidazole revealed that the purity of VLP improves with increasing concentrations of imidazole (**Figure 2.9B**). In particular, the 500 mM fraction achieved a VLP purity of nearly 10%, a ~100-fold increase compared to the starting material (**Figure 2.9B**). Thus, his-tagged VLP can be efficently enriched using IMAC, however at the expense of significant loss of total HA and M1 protein (**Figure 2.9A**).

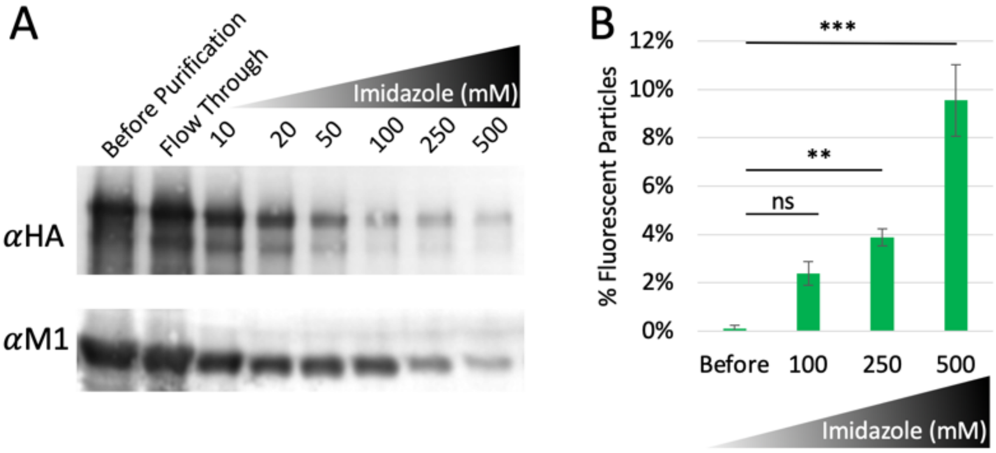

Figure 2.9. IMAC enhances purity of his-tagged VLP
(**A**) Western blot analysis of HisFCM1 VLP eluted with indicated concentrations of imidazole during IMAC. (**B**) NTA analysis of selected IMAC fractions indicates significant increase in VLP purity in fractions eluted at higher imidazole concentrations. Data represent mean ± SEM, n = 3; statistical comparisons computed by one-way ANOVA followed by post hoc Tukey's pairwise comparisons, $*p < 0.05$, $**p < 0.01$, $***p < 0.001$.

To investigate VLP morphology, we performed transmission electron microscopy (TEM) on HisFCM1 samples eluted with 500 mM imidazole. Immunolabeling was performed with anti-HA antibody followed by a gold-conjugated secondary antibody. Representative particles are indicated in **Figure 2.10**. Particle sizes ranged from approximately 100 – 500 nm and morphologies included spherical, elongated, and amorphous particles. The observation of varied

VLP morphogies suggests that multiple mechanisms of VLP formation may be at work. For example, spherical particles may form by traditional means of budding from the plasma membrane, while more irregular VLP may form through the rupture of yeast spheroplasts. Dense gold labeling can also be observed on the surface of VLP, demonstrating that the HA protein is in the correct orientation with high surface density, both critical components for vaccination.

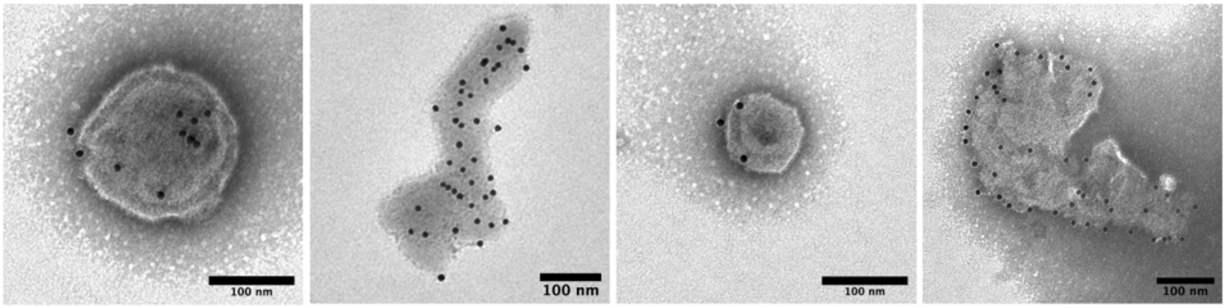

Figure 2.10. TEM reveals dense HA immunolabing on VLP
TEM imaging was performed on IMAC-purified HisFCM1 VLP followed by immunogold labeling of HA. Diverse particles with dense immunogold labeling can be observed.

2.4.5. Yeast-derived VLP Display Functional Characteristics of Influenza Virus

The HA protein serves several functional roles in the influenza virus life cycle. Notably, HA binds to sialic acid residues on the surface of cells, leading to viral entry through endocytosis. To test the ability of yeast-derived VLP to bind sialic acid, a hemagglutination assay was performed (**Figure 2.11**). IMAC elution fractions of HisFCM1 VLP were serially diluted and incubated with red blood cells (RBCs). Notably, the 500 mM elution fraction was able to agglutinate RBCs and prevent them from settling until diluted 8-fold, demonstrating that yeast-derived VLP possess the ability to bind sialic acid. However, the 250 mM and 100 mM elution fractions did not show any agglutination ability, indicating that these fractions possess lower VLP quality.

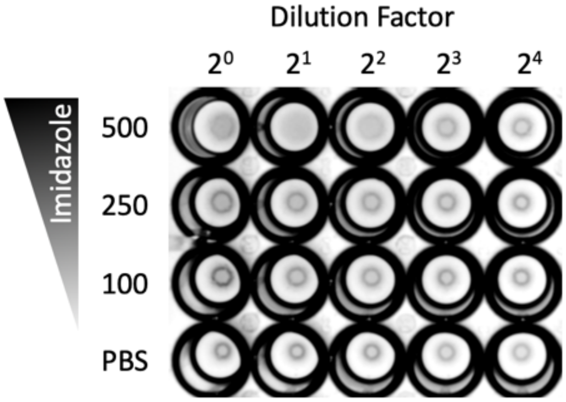

Figure 2.11. VLP can agglutinate red blood cells
Hemagglutination assay indcates the 500 mM elution fraction of HisFCM1 can agglutinate red blood cells until diluted 8 fold. This indicates that yeast-derived HA can bind sialic acid.

We next evaluated the ability of VLP to be endocytosed by cells *in vitro* (**Figure 2.12A**). HisFCM1 VLP were incubated with Madin-Darby Canine Kidney (MDCK) cells – a model epithelial cell line – followed by extensive washing. When cellular fluorescence was analyzed by flow cytometry, a substantial shift is observed for all VLP-treated cells compared to PBS treatment (**Figure 2.12B**). In contrast, when MDCK cells were pretreated with sialidase, an enzyme that cleaves sialic acid (**Figure 2.12A**), no fluoresence shift is observed (**Figure 2.12B**). Thus, VLP binding to MDCK cells is sialic acid dependent, further demonstrating the sialic acid binding ability of yeast-derived HA. To investigate cellular uptake of VLP, Z stacks of MDCK cells treated with HisFCM1 VLP were obtained by confocal microscopy. Numerous fluorescent VLP could be identified on the cells (**Figure 2.12C**). Furthermore, analysis of vertical cross sections (**Figure 2.12C**, periphery) revealed that VLP occupy different Z planes, a result consisitent with VLP internalization. Together these results indicate that yeast-derived influenza VLP display critical functional properties of HA that make yeast derived VLP a promising candidate for vaccination.

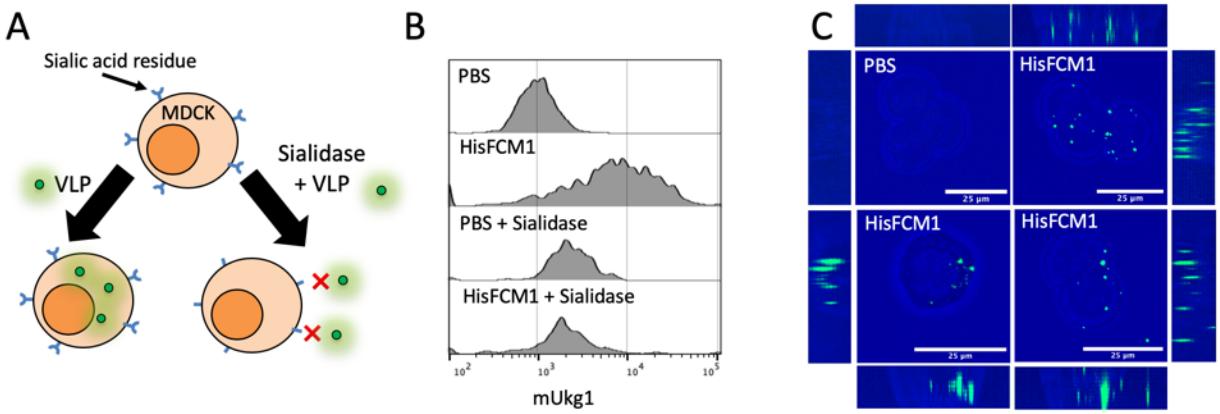

Figure 2.12. VLP bind MDCK cells in sialic acid dependent manner and are internalized (**A**) Design of uptake assay. Mammalian MDCK cells pre-treated with or without sialidase were incubated with HisFCM1 VLP. Sialidase will cleave sialic acid on the surface of the cells, preventing VLP from binding. (**B**) Flow cytometry of uptake assay samples indicates that (1) FCM1 VLP bind to MDCK cells as witnessed by the increase in MDCK cell fluorescence compared to PBS control, and (2) pre-treatment with sialidase prevents this binding. (**C**) Confocal microscopy images of MDCK cells incubated with PBS or HisFCM1 VLP. Central images are maximum intensity projections created from z stacks. Periphery images are z stack cross sections of central images. The varied depth of VLP within cells (periphery images) indicates VLP internalization.

2.5. Conclusion

In summary, we have demonstrated that the yeast *S. cerevisiae* possesses the capacity produce full length and glycosylated HA and M1 proteins from diverse influenza subtypes. We also discovered a critical defect in *S. cerevisiae* that prevents HA from efficiently localizing to the plasma membrane where VLP formation takes place. Importantly, we were able to re-engineer the localization of HA to efficiently target the plasma membrane by fusing a fluorescent protein to the C-terminus of HA. Upon subsequent removal of the yeast cell wall, we discovered numerous fluorescent nanoparticles in yeast supernatants. Furthermore, TEM analysis of these particles revealed varied particle morphologies that could be densely labeled with anti-HA antibodies, revealing for the first time the successful production of influenza VLP in *S. cerevisiae*. In addition, these VLP displayed functional characteristics of influenza virus due to their ability to agglutinate red blood cells, bind MDCK cells in a sialic acid dependent manner, and undergo endocytosis. Overall these results reveal that the lower eukaryote *S. cerevisiae* has the capability of producing functional influenza VLP with promising vaccination potential. Combined with the genetic manipulability and speed of recombinant protein production in *S. cerevisiae*, this system possesses the ability to rapidly synthesize both native and modified influenza VLP, greatly expediting the testing and engineering of influenza VLP vaccines. Finally, while overall VLP yield is relatively low, we demonstrate that multicopy integration has the potential to increase yields at least 10-fold. These findings outline an efficient path to further increasing VLP production capacity if tools are developed that can rapidly identify high expressing yeast integration clones (explored in **Chapter 3**).

2.6. Materials and Methods

2.6.1. Strains, Plasmids, and Reagents, and Cell Culture Conditions

All yeast strains were constructed from *S. cerevisiae* W303-1a (ATCC 208352). All chemicals and reagents were purchased from Sigma-Aldrich (St. Louis, MO) unless specified otherwise. Non-plasmid-bearing yeast strains were grown in either YPAD medium (10 g/L yeast extract, 20 g/L peptone, 100 mg/L adenine sulfate, 20 g/L glucose), and plasmid bearing strains or yeast synthetic complete (SC) medium (1.67 g/L of yeast nitrogen base (Difco, Detroit, MI), 5 g/L ammonium sulfate, 20 g/L glucose, 100 mg/L adenine sulfate, and 0.64 g/L of CSM (MP Biomedicals, Solon, OH)). Plasmid-bearing yeast strains were grown in appropriate SC dropout medium (same recipe as SC medium except that CSM dropout powder was used in place of the CSM powder). Cell concentrations were determined as OD measurements at 600 nm using a Spectramax M5 plate reader (Molecular Devices, Sunnyvale, CA) and standard curve (1 OD is calibrated to equal 25 million cells). All centrifugation steps were performed at 3200 × g for 3 minutes unless stated otherwise.

2.6.2. Growth, Induction, Cell Wall Removal, and VLP Harvest

Yeast cells were grown at 30 °C in an orbital shaker at 225 RPM to OD of 4.0 - 5.0. Next, 3 OD cells were then washed once in water and induced in 3 mL YPAG media (10 g/L yeast extract, 20 g/L peptone, 100 mg/L adenine sulfate, 20 g/L galactose, 100 mM sodium phosphate, pH 7.6) and cultured in 20 x 150 mm glass round bottom tube (Electron Microscopy Sciences, Hatfield, PA) at 20°C 225 RPM. Cells were harvested when they reached 3 – 4 OD (24 - 48 hrs) for cell wall removal. Cells were resuspended to 40 OD/mL in water with 30mM TCEP (Bond-Breaker™ Thermo Fisher Scientific, Waltham, MA) to reduce disulfide bridges and loosen the cell wall. After incubation at 30°C without shaking for 20 min, cells were resuspended in equal volume TMS buffer (50 mM Tris-HCl pH 7.4, 5 mM $MgCl_2$, 1 M sorbitol) with 3 mM TCEP and 320 U/mL of lyticase from *Arthrobacter luteus* and incubated at 30°C without shaking to initiate cell wall removal. After 45 min of lyticase treatment, the resulting spheroplasts were washed twice with 1 M sorbitol and resuspended in YPAG with 1 M sorbitol. Cells were incubated 16 hrs at 20°C 80 RPM in unbaffled flask. Spheroplasts were then pelleted and the supernatant was centrifuged at 10,000 x g for 20 min to remove large debris. VLP were then pelleted at 150,000 x g for 1 hr 4°C. VLP were resuspended in PBS (non-his tagged constructs) or binding buffer (10 mM imidazole, 20 mM sodium phosphate, 500 mM sodium chloride).

2.6.3. IMAC Purification

Ultracentrifuged VLP were incubated with Ni-NTA resin beads for 1 hr at 4°C. Beads were serially eluted with fractions of increasing imidazole concentration (20, 50, 100, 250 and 500 mM). To remove imidazole, fractions were buffer exchanged into 20 mM sodium phosphate buffer using a 10 kDa concentrator and stored at 4°C.

2.6.4. VLP Characterization

Western Blot: Cell lysates were prepared for SDS PAGE by incubating cells with 0.1 M NaOH for 5 min at room temperature followed by resuspension in Laemelli buffer (BioRad). For quantification, lysates and cell supernatants were compared to serial dilution of purified soluble H1, H3, or H7 proteins (Sino Biologicals, Beijing, China). SDS PAGE was performed followed by transfer to PVDF membrane. Western blotting was carried out with either anti-M1 (Thermofisher), anti-HA (Sino Biologicals), anti-GAPDH (Thermofisher), or anti-His (BioLegend) mAbs followed by species-specific IgG conjugated to alkaline phosphatase (Invitrogen).

PNGaseF Treatment: 0.25 OD cells were incubated in 0.1M NaOH for 5 min room temperature. Cells were resuspended in glycoprotein denaturing buffer (New England Biolabs) and subjected to PNGaseF protocol according to manufacturer’s instructions (New England Biolabs).

qPCR: The copy number of HA gene was determined using quantitative PCR (qPCR) by comparing the C_T values of the HA gene to the reference gene phosphoglucose isomerase (*PGI1*) using previously described methods.[74] qPCR was performed on 7900HT (Applied Biosystems, Warrington, UK) with SYBR Green qPCR Master Mix (Applied Biosystems, Warrington, UK) containing 200 nM of qPCR primers and 200 ng genomic DNA isolated from each strain using the Wizard Genomic DNA kit (Promega, Madison, WI).

Yeast Intracellular Staining and Confocal Microscopy: 0.5 OD yeast spheroplasts were fixed with 200 µL 4% formalin for 30 min at room temperature. The formalin-fixed spheroplasts were then permeabilized in 200 µL saponin-based permeabilization buffer (eBioscience, San Diego, CA) for 30 minutes at room temperature, pelleted, and stained with anti-HA mouse antibody (Sino Biologicals, Beijing, China) at 1:100 dilution in 50 µL permeabilization buffer for 1 hr at room temperature. Spheroplasts were then washed twice in 200 µL permeabilization buffer, resuspended in 50 µL of permeabilization buffer containing 1:100 anti-mouse AF647 secondary antibody (BioLegend, San Diego, CA) at the desired concentration, and incubated for 1 hr at room temperature. After washing twice in 200 µL permeabilization buffer, spheroplasts were resuspended to 0.5 million spheroplasts/mL in flow buffer (PBS pH 7.4, 0.5% bovine serum albumin). Samples were then analyzed by confocal microscopy using a Leica TCS SP8 MP inverted confocal microscope (Leica Microsystems, Wetzlar, Germany) or by flow cytometry on an Attune flow cytometer (Applied Biosystems, Foster City, CA). Flow cytometry data were analyzed using FlowJo (FlowJo LLC, Ashland, OR).

Nanoparticle Tracking Analysis (NTA): VLP were quantified using a NanoSight NS300 particle tracking system (Malvern Panalytical, Malvern, United Kingdom) using a 488 nm laser. Three videos of 60 s were recorded for each sample. Fluorescent VLP were recorded in the presence of a 500 nm long pass optical filter whereas total particles were recorded without the optical filter. Samples were diluted in PBS to maintain total particle concentration within manufacturer guidelines. Particle counts were obtained with nanoparticle tracking analysis (NTA) software provided with the NS300 system.

Transmission Electron Microscopy (TEM): VLPs were visually characterized by immunogold-labeling analysis using TEM. Briefly, VLP were absorbed on to glow discharged nickel grids (Electron Microscopy Sciences) and incubated with 20 ng/μL anti-HA antibody for 1 hr, followed by labeling with protein G conjugated 15 nm gold nanoparticle (Electron Microscopy Sciences) at a concentration of 10^{11} gold nanoparticles/mL for 30 min. Grids were stained with 2% phosphotungstic acid (PTA) and allowed to dry 1 hr prior to TEM analysis on a JEM-1400 Transmission Electron Microscope at 80 kV (JEOL, Peabody, MA).

HA Assay: 50 μL VLP samples were serially diluted in PBS. 50 μL 0.5% chicken red blood cells (Innovative Research, Novi, MI) were added to each dilution and incubated for 1 hr.

Uptake Assay: MDCK cells were plated at approximately 50,000 cells/well in a 24-well plate and allowed to attach overnight. The following day cells were washed twice with 1X HBSS (Invitrogen) and incubated in 1X HBSS with or without 2 U/mL neuraminidase (NA) for 30 minutes at 37°C. Following NA treatment, cells were washed once with 1X HBSS and 100 μl VLPs were added to each well for 1 hr at 37°C. Light shaking was applied to the plates every 15 minutes to ensure even distribution of the VLP and to prevent cells from drying out. Following particle uptake, cells were washed twice with 1X PBS without magnesium and calcium and incubated in 0.25% trypsin for 10 minutes to detach cells from the plate. Cells were centrifuged at 300 x g for 5 minutes and resuspended in flow buffer for analysis on an Attune NXT Acoustic Focusing Cytometer (Applied Biosystems) or on Leica TCS SP8 MP inverted confocal microscope (Leica Microsystems).

2.6.5.Design of Influenza Constructs

All plasmids were constructed by homologous recombination.[231] HA and M1 genes were PCR amplified from cDNA obtained by reverse transcription of H1N1 A/Puerto Rico/1934 and H3N2 A/Aichi/2/1968 viral RNA using Transcriptor First Strand cDNA Synthesis Kit (Roche, Basel, Switzerland) following manufacturer instructions. HA and M1 genes from H7N9 A/Shanghai/MH01/2013 were synthesized by IDT DNA Technologies (Coralville, IA). *Gal10 Gal1* bidirectional promoter, *TDH3* terminator, *TPI1* terminator, and yeast δ sequence were PCR amplified from yeast genomic DNA. Fragments were recombined into digested pRS426 plasmid (NEB) as indicated in **Figure 2.1A** to obtain H1M1, H5M1, and H7M1.

Fluorescent plasmids were also constructed by homologous recombination.[231] FNM1 plasmid was obtained by fusing ymUkG1[221] to the N-terminus of HA after the signal sequence. Additionally, a flexible linker (GGGSGGGS) and the first 9 aa of the H3 hemagglutinin were included between ymUkG1 and H1 as spacers as recommended elsewhere.[232] The FCM1 was obtained by fusing ymUkG1[221] to the C-terminus of HA with a flexible linker (GGGSGGGS). HisFCM1was obtained by fusing a 10×His tag to the N-terminus of FC after the signal sequence. In addition, the first 9 aa of the H3 hemagglutinin were included between 10×His tag and FC as a spacer as recommended elsewhere.[232]

Integrated H1M1 constructs were obtained by multicopy integration into the yeast δ site using a CRISPR multicopy integration. W303-1a was first transformed with p414-TEF1p-Cas9-CYC1t encoding a Cas9 expression cassette (a gift from George M. Church, Addgene plasmid #43802) and plated on SC-TRP. A single colony was picked from the plate and transformed simultaneously with p426gRNA-Delta (**Table 3.1**) encoding the guide RNA targeting the yeast δ site and linearized donor DNA containing the H1M1 expression cassette flanked by δ sites produced from PCR amplification of H1M1 plasmid (**Table 3.1**). Transformants were plated on SC-TRP-URA. Transformants were screened by Western blot for high expressing clones. The highest expressing clone was designated Int #1. The p426gRNA-Delta plasmid in Int #1 was lost by serial passaging in YPAD media. This entire process was then repeated to obtain Int #2 and again to obtain Int #3.

Chapter 3. Development of a Yeast Intracellular Staining (yICS) Approach for Accelerated Characterization and Screening of VLP Strains

3.1. Publication Information

Hill, B. D., Prabhu, P., Rizvi, S. M. & Wen, F. Yeast Intracellular Staining (yICS): Enabling High-throughput, Quantitative Detection of Intracellular Proteins via Flow Cytometry for Pathway Engineering. *ACS Synth. Biol.* acssynbio.0c00199 (2020). doi:10.1021/acssynbio.0c00199

The goal of this chapter is to develop an approach for high-throughput screening and characterization of *S. cerevisiae* influenza VLP strains using flow cytometry. As a proof of concept, the established technique was validated on a 3 enzyme model system that is well understood in our laboratory – the oxidoreductase xylose assimilation pathway – but is highly applicable for expediting the identification of clones expressing high levels of influenza proteins following multicopy integration as well as assisting in strain characterization. In fact, this tool was used for influenza VLP strain characterization in **Figure 2.2**. Dr. Prabhu Ponnandy and Dr. Syed Monem Rizvi assisted in library screening, performing fermentation analysis, and performing qPCR analysis.

3.2. Abstract

Optimizing expression of foreign genes in recombinant hosts often necessitates screening libraries to discover phenotypes of interest (*e.g.* high expressing clones). While *Saccharomyces cerevisiae* is a common host for expression of foreign proteins, current approaches for detection of intracellular proteins in yeast either have low throughput, can interfere with protein function, or lack the ability to detect multiple proteins simultaneously. To fill this need, we developed yeast intracellular staining (yICS) that enables fluorescent antibodies to access intracellular compartments of yeast cells while maintaining their cellular integrity for analysis by flow cytometry. Using the housekeeping proteins β actin and glyceraldehyde 3-phophate dehydrogenase (GAPDH) as targets for yICS, we demonstrated for the first time successful antibody-based flow cytometric detection of yeast intracellular proteins with no modification. Further, yICS characterization of a model 3-enzyme pathway showed 3-plexed, quantitative detection of all 3 pathway enzymes, revealing distinct enzyme expression profiles between plasmid-based and genome-integrated expression approaches. As a result of its high-throughput and quantitative capability, yICS enabled rapid screening of a multicopy integration library, identifying rare (1%) high expressing clones that led to an ~8-fold increase in target protein expression level. These results demonstrate the utility of yICS for greatly accelerating VLP engineering efforts, as well as any application where the high-throughput and quantitative detection of intracellular proteins is desired.

3.3. Introduction

Due to its model eukaryote status and ease of genetic manipulation, *Saccharomyces cerevisiae* remains one of the most popular organisms for production of therapeutic proteins (*e.g.,* VLP) and industrially relevant compounds.[214,233-238] The production of these products often necessitates the expression of foreign proteins sourced from diverse organisms. However, expression of foreign proteins in new hosts is rarely straightforward (see **Chapter 2**), often necessitating the screening of libraries to discover desirable phenotypes.[239-244] For example, integration of H1M1 into *S. cerevisiae* in **Section 2.4.2** yielded hundreds of colonies that needed to be screened to identify high expressing clones, an incredibly tedious task using the traditional method of Western blot. Therefore, high-throughput and quantitative protein detection methods that could facilitate the efficient screening of these libraries are of great interest.

The compatibility of *S. cerevisiae* with flow cytometry allows for a convenient, quantitative, and high throughput means of protein detection as long as the protein expression can be coupled to fluorescence. While surface-displayed proteins on the yeast cell wall can be conveniently labeled with fluorescent antibodies,[245-247] the vast majority of proteins (*i.e.* HA and M1) are not surface accessible and therefore require alternative labeling strategies,[248] the most common being fusing the protein of interest (POI) with a reporter protein.[249] The most ubiquitous reporters are fluorescent proteins of which there are a diverse range that allow choice of spectra, pH stability, brightness, and photostability.[250] Other commonly used reporters are "self-labeling" enzymes, such as the Halo tag[251,252] or SNAP/CLIP tag,[253,254] that covalently bind to their externally added substrates. These substrates are usually conjugated with organic dyes which offer superior photophysical properties compared to fluorescent proteins including greater brightness and broader spectral diversity.[255] However, both the fluorescent proteins and self-labeling enzymes are relatively large in size (20-33 kDa), and therefore their fusion with the POI often negatively affects protein function.[256-260] Moreover, the production of reporter protein fusions consumes additional cellular resources that can inhibit cell growth or detract from the production of pathway products.[261,262] Therefore, alternative methods for coupling fluorescence to POI expression that do not rely on large protein fusions are advantageous.

The tetracysteine-biarsenical system is one of the most proven methods for fluorescent labeling of POIs and only requires fusion of a small tag of 6-12 amino acids (aa) (~1 kDa). The tag contains four cysteines that bind to externally-added, cell-permeable FlAsH and ReAsH biarsenical ligands, resulting in fluorescence.[263,264] In several cases, this system results in less perturbation of POI localization[265,266] or enzymatic activity[267] compared to fusion with large fluorescent proteins. Additionally, protocols have been developed to allow for detection of two POIs simultaneously.[268] These advantages have resulted in the extensive use of the tetracysteine-biarsenical system for live-cell imaging of intracellular proteins in a wide variety of cellular systems.[269] However, there are surprisingly few examples of its application to high-throughput library screening,[270,271] most likely due to the fact that the sensitivity of the tetracysteine-biarsenical system is at least an order of magnitude lower than that of green fluorescent protein.[270] Consequently, the system may have limited signal-to-noise ratio when used for the detection of low expressing POIs, which is not uncommon when expressing heterologous proteins.

Examination of the aforementioned intracellular protein detection methods reveals a tradeoff between sensitivity and impact on POI expression and/or its function. We recognized that this tradeoff could be overcome by directly staining intracellular proteins with antibodies followed by flow cytometry analysis, however such an approach has not been developed for yeast. Compared to fusion of the POI with a large reporter protein, the use of antibodies for yeast intracellular POI detection minimizes the likelihood of perturbing POI function because antibody-POI binding can be accomplished by the use of small epitope tags (6-14 aa) commonly used in Western blot (i.e. c-myc, flag, V5, HA, His, etc.). In the event that even small tags unacceptably affect the POI, as has been reported in some cases,[272] detection can be accomplished with POI-specific antibodies, abolishing the need for any POI modification. In addition, the diversity of fluorophore-antibody conjugates offers a wide range of brightness and spectral properties, allowing for the detection of low expressing POIs as well as multiple POIs simultaneously. Coupled with flow cytometry, such an antibody-based yeast intracellular staining (yICS) approach represents a sensitive, multiplexed, and high-throughput means for library screening.

In this study, we developed the yICS method that allows antibodies to directly access yeast intracellular compartments while maintaining cellular integrity for analysis by flow cytometry. In the first successful attempt of antibody-based flow cytometric detection of yeast intracellular proteins, we demonstrate that yICS enables quantitative and reproducible detection of the yeast house-keeping proteins β actin and glyceraldehyde 3-phophate dehydrogenase (GAPDH). As a proof of concept, we applied yICS to characterize and enhance foreign protein expression in a model 3-enzyme system. The yICS technique enabled simultaneous detection of all three pathway enzymes. Furthermore, the single-cell nature and sensitivity of yICS revealed clear variation in expression profiles depending on whether the enzyme expression cassettes were present on plasmids or integrated into the genome. Finally, yICS screening of multicopy integration libraries rapidly identified rare (~1%) high copy integration clones possessing ~8-fold improvement in both enzyme expression level and enzyme activity. These results demonstrate the utility of yICS for both characterizing and enhancing foreign protein expression in *S. cerevisiae.*

3.4. Results and Discussion

3.4.1. Yeast Intracellular Staining (yICS) Design and Feasibility

The success of the yICS procedure hinges on enabling antibody access to intracellular compartments while maintaining cellular integrity for flow cytometry analysis. As the large size of antibodies prevents them from penetrating the cell wall of *S. cerevisiae,*[273] the first and most critical step of the yICS procedure is the complete removal of the cell wall by exposing the yeast cells to enzymes possessing mannase and β-1,3-glucanase activities (**Figure 3.1**, Step 1). Immediately following cell wall removal, a fixation step is performed to stabilize the resulting fragile spheroplasts and to immobilize intracellular antigens for subsequent procedures (**Figure 3.1**, Step 2). Next, antibody access to intracellular compartments is afforded by detergent permeabilization of cellular membranes (**Figure 3.1**, Step 2). Antibody staining of intracellular proteins of interest (POIs) can then proceed (**Figure 3.1**, Step 3), followed by detection of POIs using flow cytometry (**Figure 3.1**, Step 4).

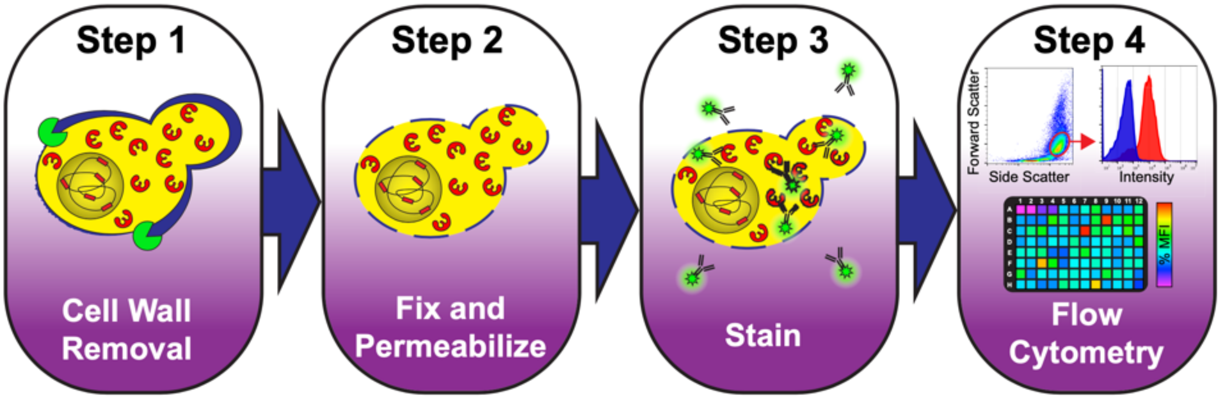

Figure 3.1. Design of the yeast intracellular staining (yICS) procedure
Step 1 of the yICS procedure is the enzymatic removal of the cell wall to form spheroplasts, which are then fixed in Step 2 to provide structural integrity and permeabilized to enable antibody access to intracellular compartments. Antibody staining of intracellular POIs is performed in Step 3, followed by flow cytometry in Step 4.

To test the feasibility of the yICS procedure, we first examined if fragile yeast spheroplasts could maintain their cellular integrity and be detected during flow cytometric analysis. To this end, yeast cells were grown to mid-log phase, treated with lyticase enzyme (see methods) to remove the cell wall, and observed under a microscope. In contrast to untreated cells (**Figure 3.2A**, left), lyticase-treated cells had a spherical shape and lacked protruding buds (**Figure 3.2A**, middle), both of which are characteristic of spheroplast formation.[274] In addition, the lyticase-treated sample showed some cellular debris (data not shown), presumably due to spheroplast lysis. This is not surprising as it is known that yeast cells lacking their cell wall are fragile and prone to lysis, especially when subjected to osmotic shock.[275,276] Indeed, lyticase-treated cells that were briefly exposed to hypotonic conditions (*i.e.* water) showed clumps of debris and were virtually absent of intact cells (**Figure 3.2A**, right), providing further evidence that lyticase treatment resulted in spheroplast formation.

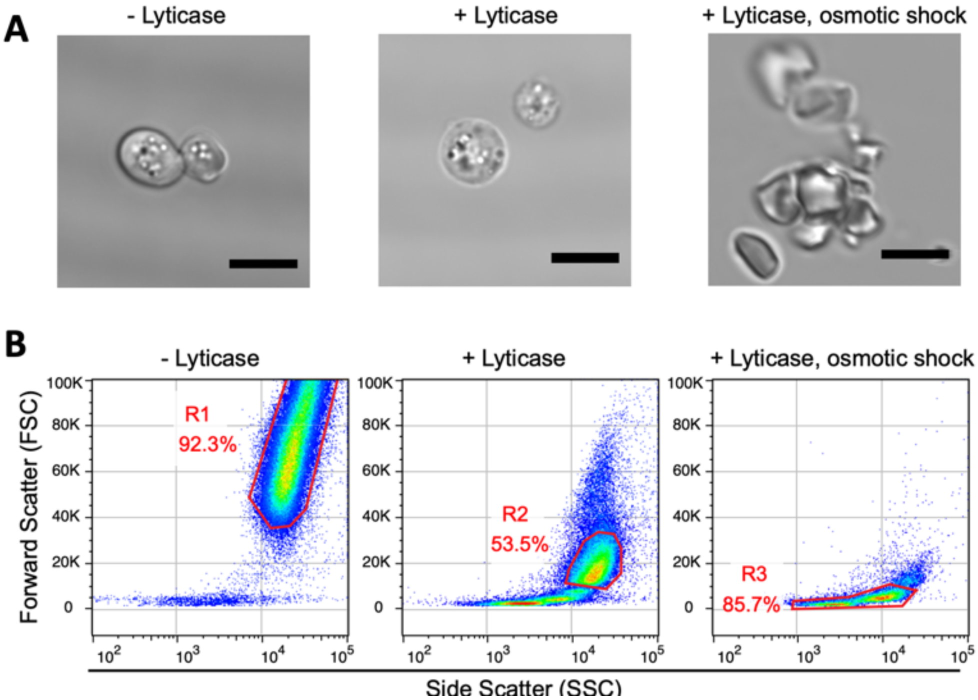

Figure 3.2. Spheroplast detection by flow cytometry

(**A**) Microscope images of cells before lyticase treatment (left), spheroplasts after lyticase treatment (middle), and lysed spheroplasts after osmotic shock in water (right). Scale bar is 5 µm. (**B**) Flow cytometry is able to differentiate cells with intact cell walls (left, R1 gate), spheroplasts (middle, R2 gate), and lysed spheroplasts (right, R3 gate). The frequency of events in each gated population is shown adjacent to the gate

After confirming spheroplast formation, samples were fixed with 1% formalin under isotonic conditions (*i.e.* 1 M sorbitol) and subjected to flow cytometry analysis. Examination of the forward scatter (FSC) and side scatter (SSC) revealed that, compared to untreated cells (**Figure 3.2B**, left, R1), lyticase-treated cells formed a distinct population (**Figure 3.2B**, middle, R2) characterized by lower FSC. This result was somewhat surprising because FSC intensity is generally thought to be indicative of cell size, yet the size of spheroplasts did not appear significantly altered when observed under a microscope (**Figure 3.2A,** left and middle). Instead, this reduced FSC intensity is likely due to altered optical properties of cells after cell wall removal, as supported by reports of spheroplasts appearing darker compared to non-spheroplasts when visualized by phase contrast microscopy.[277] Importantly, about 50% of lyticase-treated cells (**Figure 3.2B**, middle, R2) were distinct from the lysed spheroplast population (**Figure 3.2B**, right, R3), confirming that a substantial fraction of spheroplasts remain intact during flow cytometry analysis. Taken together, these results indicate that formalin-fixed yeast spheroplasts can maintain their structural integrity and are readily detectable by flow cytometry, demonstrating the feasibility of the yICS procedure (**Figure 3.1**).

3.4.2. Development of a High-throughput yICS Workflow

After verifying that intact spheroplasts can be detected by flow cytometry, we next sought to develop a high-throughput yICS procedure that would permit the screening of large libraries. While antibody staining and flow cytometry can all be performed in 96-well format, cell wall removal typically involves a time-consuming pre-culture step (~4 hrs) in tubes or flasks to grow cells to mid-log phase, limiting the throughput of yICS-based screening and extending the duration of the yICS procedure beyond the length of a conventional workday. A convenient solution is to culture picked colonies overnight directly in 96-well plates and perform the yICS procedure the following morning. However, a significant challenge of this approach is that the resulting cell growth (hereafter referred to as growth OD_{600}) exceeds the mid-log phase (~0.5 - 1.0 OD_{600}) that is optimal for cell wall removal.[275,276] Indeed, colonies picked directly into wells of a 96-well plate and grown overnight in rich YPAD media resulted in growth OD_{600} ranging from 3.4 to 5.6 (**Figure 3.3**), making complete cell wall removal more challenging. Therefore, it is essential to establish a robust cell wall removal protocol that can achieve satisfactory cell wall removal over a wide range of growth OD_{600}.

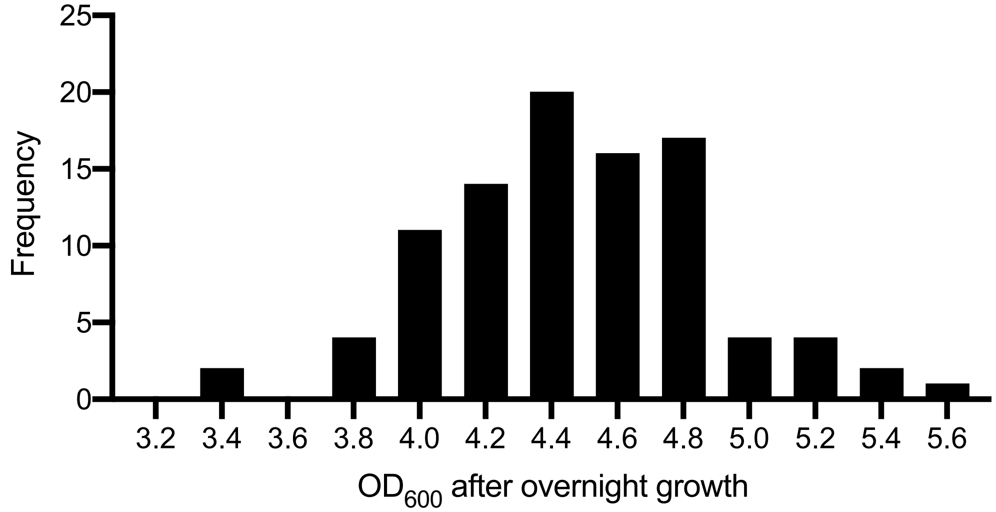

Figure 3.3. Histogram of cell growth after overnight culture in 96-well plate
Single colonies of strain W303-1a were seeded into individual wells of a 96-well plate in 250 μL YPAD and grown 16 hours at 30°C. Resulting cell growth ranges from 3.4 to 5.6 OD_{600}.

To this end, we first set out to define a quantitative metric for satisfactory cell wall removal. Cells were grown to a growth OD_{600} of 2.2 in rich YPAD media in a 96-well plate and then cell wall removal was performed on 5 million cells using a range of lyticase concentrations under hypotonic conditions. Cell wall removal efficiency was assessed using the ratio between the OD_{600} during lyticase treatment and the initial OD_{600} (OD/OD_{init}), as previously reported.[275,276] With no lyticase addition, the OD/OD_{init} ratio remained near 1 for the entirety of the 60 minutes (**Figure 3.4A**), suggesting that no cell lysis and hence no spheroplast formation had taken place. In contrast, the OD/OD_{init} ratio of lyticase-treated samples declined with increasing lyticase concentrations and longer treatment time. For lyticase concentrations ≥ 80 U/mL, the OD/OD_{init} ratio stabilized near 0.1, suggesting this value correlates with complete cell wall removal. Consequently, we designated that cell wall removal conditions achieving $OD/OD_{init} \leq 0.15$ (**Figure 3.4A**, dotted line) were satisfactory for future experiments. Furthermore, treatment with lyticase concentrations ≥ 160 U/mL were able to achieve $OD/OD_{init} \leq 0.15$ in less than 20 minutes, suggesting these conditions can accommodate higher growth OD_{600} within a reasonable timeframe.

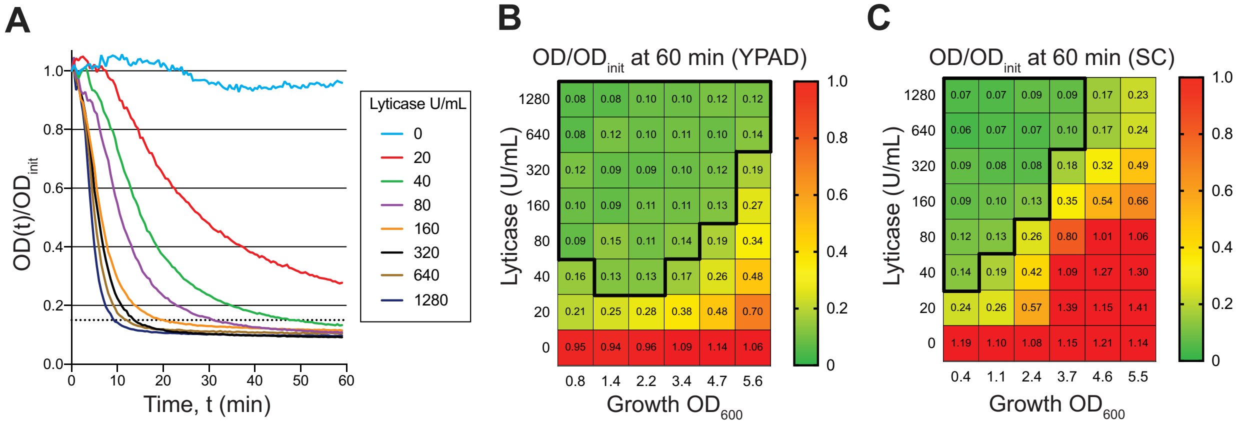

B: OD/OD$_{init}$ at 60 min (YPAD)

Lyticase (U/mL)	0.8	1.4	2.2	3.4	4.7	5.6
1280	0.08	0.08	0.10	0.10	0.12	0.12
640	0.08	0.12	0.10	0.11	0.10	0.14
320	0.12	0.09	0.09	0.10	0.12	0.19
160	0.10	0.09	0.11	0.11	0.13	0.27
80	0.09	0.15	0.11	0.14	0.19	0.34
40	0.16	0.13	0.13	0.17	0.26	0.48
20	0.21	0.25	0.28	0.38	0.48	0.70
0	0.95	0.94	0.96	1.09	1.14	1.06

Growth OD_{600}

C: OD/OD$_{init}$ at 60 min (SC)

Lyticase (U/mL)	0.4	1.1	2.4	3.7	4.6	5.5
1280	0.07	0.07	0.09	0.09	0.17	0.23
640	0.06	0.07	0.07	0.10	0.17	0.24
320	0.09	0.08	0.08	0.18	0.32	0.49
160	0.09	0.10	0.13	0.35	0.54	0.66
80	0.12	0.13	0.26	0.80	1.01	1.06
40	0.14	0.19	0.42	1.09	1.27	1.30
20	0.24	0.26	0.57	1.39	1.15	1.41
0	1.19	1.10	1.08	1.15	1.21	1.14

Growth OD_{600}

Figure 3.4. Development of high-throughput cell wall removal condition
(**A**) 5 million cells from a culture grown overnight in YPAD to an OD_{600} of 2.2 were subjected to varying lyticase concentrations under hypotonic conditions, and spheroplast formation was monitored over time using the ratio of the OD_{600} at time *t* and the initial OD_{600} at $t = 0$ of the reaction mixture ($OD(t)/OD_{init}$). The dotted line represents $OD(t)/OD_{init} = 0.15$, the selected benchmark for adequate cell wall removal. (**B, C**) OD/OD_{init} values after 60 min treatment with a

range of lyticase concentrations for cells grown to various OD_{600} in either YPAD media (**B**) or synthetic complete (SC) media (**C**). Color bar indicates OD/OD_{init} values. Cell wall removal conditions achieving $OD/OD_{init} \leq 0.15$ are outlined in bold.

We next evaluated the range of growth OD_{600} that could achieve satisfactory cell wall removal ($OD/OD_{init} \leq 0.15$) with 60 minutes of lyticase treatment, which we deemed was a reasonable duration for step 1 of the yICS procedure (**Figure 3.1**). Cells were grown in YPAD media from a serially diluted colony in a 96-well plate to yield growth OD_{600} values from 0.8 (mid-log phase) to 5.6 (the highest growth OD_{600} observed after overnight growth, **Figure 3.3**). The OD/OD_{init} ratio after 60 minutes of lyticase treatment is recorded and color coded in **Figure 3.4B**. As growth OD_{600} increases, a higher lyticase concentration is required to achieve $OD/OD_{init} \leq 0.15$ (**Figure 3.4B**, bold boundary). However, for the two highest lyticase concentrations tested (640 and 1280 U/mL), $OD/OD_{init} \leq 0.15$ was achieved for all growth OD_{600} values tested (**Figure 3.4B**, top two rows). Thus, satisfactory cell wall removal can be accomplished for cells grown overnight in 96-well format using a 60-minute treatment with 1280 U/mL lyticase. This condition was used for subsequent experiments for cells grown in YPAD.

A parallel analysis was conducted for cells grown overnight in synthetic complete (SC) media, which is commonly used to maintain plasmid selection pressure. Compared to cells grown in YPAD (**Figure 3.4B**), cells grown in SC media were overall more resistant to cell wall removal, requiring either more lyticase or a lower growth OD_{600} to achieve $OD/OD_{init} \leq 0.15$ (**Figure 3.4C**, bold boundary). Notably, no tested lyticase concentration was able to adequately remove the cell wall within 60 minutes for growth $OD_{600} > 3.7$ (**Figure 3.4C**, right two columns). Based on this finding, a dilution step was incorporated in subsequent experiments when seeding colonies in SC media to ensure growth OD_{600} is < 3.7 to allow satisfactory cell wall removal in a 96-well format.

These results indicate that efficient cell wall removal can be achieved over a wide range of growth conditions, but is highly affected by media choice and cell growth stage in agreement with other reports.[275,276] In particular, it appears the yICS procedure is incompatible with stationary phase cells, due to the difficulty in removing their cell wall. Potentially explaining these findings, it has been demonstrated that the composition and mass of the cell wall is highly dynamic, changing with media, growth phase, temperature, and carbon source.[278] Therefore, we recommend that investigators perform similar experiments to ensure satisfactory cell wall removal under their desired experimental conditions.

3.4.3. Validation of yICS Using Yeast Housekeeping Proteins

To validate the ability of yICS to detect intracellular POIs, we chose to detect the abundant yeast housekeeping proteins β actin and GAPDH, both of which have commercial antibodies readily available and thus allowing for their detection by yICS without any protein modification. Single yeast colonies were directly seeded into a 96-well plate in YPAD media and grown overnight. Following the yICS procedure shown in **Figure 3.1A**, the cell wall was removed using the optimal condition (i.e., 60-minute treatment with 1280 U/mL lyticase) to generate spheroplasts which were then fixed with formalin and permeabilized with saponin. Permeabilized spheroplasts were stained with primary antibodies specific for β actin, GAPDH, or with a non-specific isotype control followed by a phycoerythrin (PE)-conjugated secondary antibody and subjected to flow cytometry analysis. During the fixation step, a range of formalin concentrations (0.5 - 4% at room temperature for 30 minutes) was tested in anticipation of the opposing effects of fixation on antibody binding (i.e., fluorescence signal) and spheroplast structural integrity.

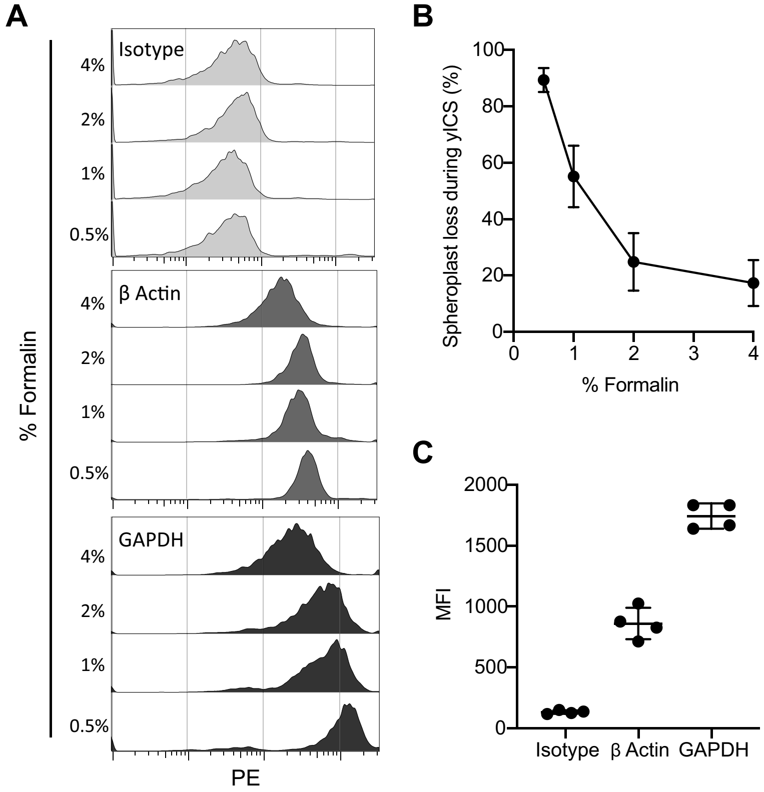

Figure 3.5. Detection of unmodified yeast intracellular housekeeping proteins by yICS
(**A**) Histograms of PE signal intensity of gated spheroplasts fixed with 0.5 - 4% formalin and stained for either a non-specific isotype control (top panel), anti-β actin (middle panel), or anti-GAPDH (bottom panel) antibodies followed by a PE-conjugated secondary antibody. (**B**) The mean percentage of spheroplasts lost during the yICS procedure was calculated as the ratio of the number of gated intact spheroplasts detected by flow cytometry and the number of cells subjected to yICS as measured by OD_{600}. (**C**) The median fluorescence intensity (MFI) of four replicates from a single overnight culture fixed with 0.5% formalin and stained as in **A**. For **B** and **C,** error bars represent standard deviation of $n = 3$ and $n = 4$, respectively.

Notably, under all fixation conditions tested, a positive staining population was observed for both β actin and GAPDH compared to the background autofluorescence peak for the isotype control (**Figure 3.5A**). This result validates the ability of yICS to detect unmodified intracellular proteins and, to our knowledge, is the first demonstration of antibody-based detection of yeast intracellular POIs using flow cytometry. Note that, although actin is the most abundant protein in eukaryotic cells,[279] the fact that β actin showed lower overall signal compared to GAPDH highlights that signal intensity is a function of several variables beyond protein abundance such as antibody affinity, antibody concentration, and antibody accessibility to its epitope. Therefore, comparing the abundance of different proteins using yICS requires an additional fluorescence quantification step.[247] As anticipated, fixation with higher formalin concentrations resulted in both slightly increased background autofluorescence signal (**Figure 3.5A**, top) and reduced fluorescence signal for both β actin and GAPDH (**Figure 3.5A**, middle and bottom), likely due to decreased antibody binding affinity for crosslinked epitopes as has been reported elsewhere.[280] As a result, the lowest formalin concentration (*i.e.,* 0.5%) yielded the best signal-to-noise ratio. However, a more significant loss of spheroplasts was observed at lower formalin concentrations, with the 0.5% formalin fixation losing nearly 85% of spheroplasts while the 4% formalin fixation lost about 10% (**Figure 3.5B**). We attributed this loss to the weaker structural integrity of the spheroplasts fixed at the lower formalin concentrations, leading to their lysis during the washing steps in the subsequent antibody staining process. Despite the significant spheroplast loss using 0.5% formalin fixation, the large number of stained yeast cells (0.2 OD_{600}, equivalent to 5 million cells) and the high acquisition rate of flow cytometry (5,000-10,000 events per second) still allow for rapid measurement of a sufficient number of intact spheroplasts for meaningful statistical analysis. Therefore, to ensure the best signal-to-noise ratio for quantitative measurement of yeast intracellular POIs, we chose to use the 0.5% formalin fixation condition and to acquire at least 30,000 events (~1 minute per sample) for future experiments. Note that, while this fixation condition was optimal for our experimental system, the tradeoff between signal-to-noise ratio and spheroplast loss should be evaluated on a case-by-case basis. Furthermore, while not investigated in this work, a fixation step can be performed before cell wall removal to minimize the effects of spheroplast formation on the metabolic and POI state in the cells.

Using the optimized 0.5% formalin fixation condition, the reproducibility of the yICS procedure was examined. A single colony was grown overnight in a 96-well plate and then split into four replicates. Following cell wall removal, formalin fixation, saponin permeabilization, and antibody staining (anti-GAPDH, anti-β actin, or an isotype control), the samples were subjected to flow cytometry analysis. The median fluorescence intensity (MFI) of the spheroplasts in each replicate showed a tight distribution with coefficients of variation (CVs) of 10.9%, 15.0%, and 6.0% for isotype control, β actin, and GAPDH, respectively (**Figure 3.5C**). Therefore, the yICS approach demonstrates the necessary reproducibility critical for characterizing and engineering recombinant pathways in yeast.

3.4.4. Characterization of a Recombinant Three-Enzyme Pathway Using yICS

As a proof of concept, we next applied yICS to characterize the heterologous oxidoreductase D-xylose assimilation pathway important for converting xylose, a major component of renewable biomass (30-40%),[281-283] into ethanol. Specifically, we investigated the relationship between the expression levels of the three enzymes in the pathway (i.e., XR, XDH, and XK) and the ability of the cells to grow when using xylose as the sole carbon source. Variations in these three enzyme expression levels were achieved in yeast W303-1a by expressing them from genes either (1) integrated into the genome (**Figure 3.6A**, FW439), (2) on their own individual plasmids (**Figure 3.6A**, 3 plasmid), or (3) all on the same plasmid (**Figure 3.6A**, 1 plasmid). As is often the case when expressing proteins from non-model organisms, commercial antibodies specific for XR, XDH, and XK are unavailable. Thus, small epitope tags His (HHHHHH), HA (YPYDVPDYA), and c-Myc (EQKLISEEDL) were appended to XR, XDH, and XK, respectively, to enable multiplexed yICS detection while minimizing the probability of affecting enzyme function (**Figure**

3.6A).

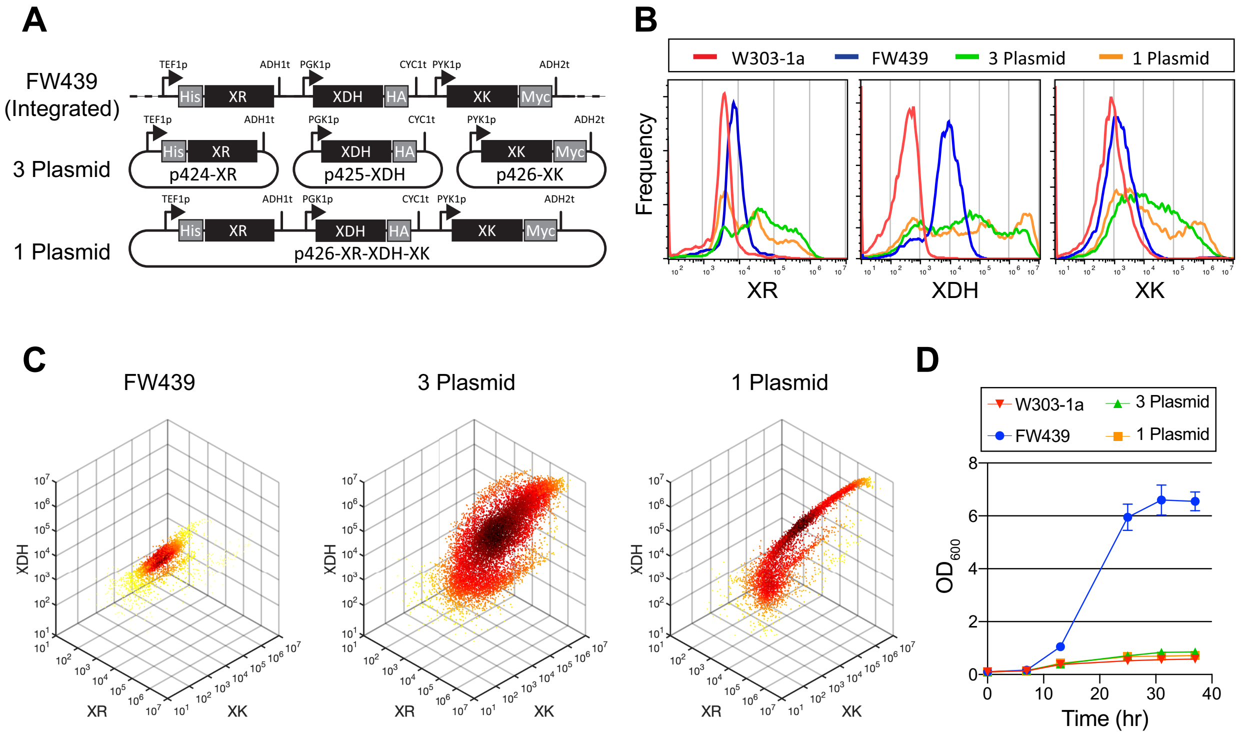

Figure 3.6. Simultaneous detection of 3 foreign proteins in model enzyme pathway
(**A**) XR, XDH, and XK pathway enzymes were tagged with His, HA, and c-Myc tags, respectively, and constitutively expressed from genes either integrated into the genome (top, strain FW439), on their own respective plasmid (middle, 3 plasmid), or on a single plasmid (bottom, 1 plasmid). Promoters and terminators for each gene are indicated by arrows and lines, respectively. (**B**) Histogram overlays of yICS signal for constructs in **A** simultaneously stained with anti-His, anti-HA, and anti-c-Myc antibodies to detect XR, XDH, and XK, respectively. Parental strain W303-1a was included as negative control. (**C**) Individual cells from **B** are plotted in three dimensions, with each axis representing the fluorescence signal intensity of XR, XDH, or XK. Coloring represents local cell density. (**D**) Aerobic growth curves with xylose as sole carbon source for constructs in **A**. Error bars represent mean ± standard deviation, *n* = 2.

Single colonies representing the three expression constructs as well as the W303-1a parental strain were diluted in appropriate glucose-containing SC dropout media and grown overnight in a 96-well plate. Spheroplasts were then prepared following the yICS procedure as described above, stained simultaneously for XR (anti-His PE), XDH (anti-HA Alexa Fluor 647), and XK (anti-c-Myc-biotin followed by streptavidin PE-Cy7), and analyzed by flow cytometry.

As shown in **Figure 3.6B**, all three expression constructs showed positive signals for all three enzymes when compared to the W303-1a parental strain, validating the use of epitope tags for multiplexed yICS detection of yeast intracellular POIs. The signal distribution for both plasmid-bearing strains was much broader with ~25-50% of the cells expressing enzyme at higher levels than that of the FW439 integration strain, likely due to the heterogeneity in the ability of yeast cells to maintain high copy number (40-60) of these 2μ plasmids. Interestingly, the 3-plasmid and 1-plasmid strains showed very similar expression profiles for each enzyme despite evidence in the literature that the maintenance of plasmids is burdensome.[284,285]

In addition to the insights gained by analyzing enzyme expression in isolation (**Figure 3.6B**), multiplexed yICS staining enables simultaneous evaluation of all enzyme levels in single cells, revealing further distinctions in the expression profile. When individual cells are visualized on a three-dimensional density plot with each axis representing the fluorescent signal intensity of XR, XDH, or XK (**Figure 3.6C**), all three constructs align along the same imaginary axis, signifying that, while the magnitude of enzyme expression varies, the relative ratio of the three enzymes in each cell is similar across these three constructs. Interestingly, the 3-plasmid strain clearly shows a looser distribution along the imaginary axis than the 1-plasmid strain (**Figure 3.6C**, middle and right), likely due to greater variations in maintaining three types of 2μ plasmids simultaneously across individual cells. Although an expected result, such an observation highlights the fidelity of the yICS method and demonstrates the power of multiplexed analyses to reveal additional findings that would not be possible studying single proteins individually.

To investigate how these different enzyme expression profiles affect the ability of the cells to grow on xylose, the various strains were grown in appropriate SC dropout media containing 2% glucose overnight and then inoculated into rich media containing 2% xylose in liquid shaking culture. Subsequent monitoring of cell growth revealed that, surprisingly, only the FW439 strain was able to grow on xylose (**Figure 3.6D**) despite the fact that the plasmid-bearing strains have ~25-50% of cells expressing higher levels of enzymes (**Figure 3.6B**). These results suggest that high expression of at least one of the enzymes is cytotoxic when the cells are grown on xylose. Supporting this, it has been reported that overexpression of XK from *S. stipitis* or its homologue in *S. cerevisiae* inhibits cell growth on xylose but does not affect growth on glucose,[286,287] potentially due to the generation of toxic byproducts and/or the depletion of ATP by XK activity.[288] Regardless of the mechanism, the data suggest that enzyme expression levels need to be tightly controlled to maximize xylose utilization, which is a challenging task using plasmid-based expression due to their highly heterogeneous expression profile. Therefore, we chose FW439 for further engineering of the pathway to improve the xylose-to-ethanol conversion.

3.4.5. Engineering a Xylose Assimilation Pathway Using yICS

One of the frequently reported bottlenecks of the oxidoreductase D-xylose assimilation pathway is the low activity of XDH relative to XR, resulting in xylitol accumulation and limiting ethanol yield.[289,290] In an attempt to increase the XDH expression level and relieve this metabolic bottleneck, we performed CRISPR-mediated genome integration of XDH into the FW439 strain (see methods). While high copy integrants are commonly identified by G418 resistance afforded by co-integration of the KanMX gene,[291] strain FW439 already contained several copies of KanMX by utilizing this technique, necessitating an alternative screening approach.

To this end, single colonies resulting from the transformation were grown overnight in YPAD media in a 96-well plate (94 transformants plus W303-1a and FW439) and subjected to yICS analysis to identify high XDH producers. As shown in **Figure 3.7A** – CRISPR Round 1, 68 of the 94 XDH transformants (i.e., ~72%) showed statistically increased MFI compared to the parental FW439 strain ($p < 0.05$, assuming a CV of 15%). The highest XDH-expressing clone, FW706, showed nearly a 4-fold increase in MFI and was chosen for a second round of CRISPR-mediated genome integration of XDH. yICS screening was performed on the resulting library, including W303-1a and FW439 as controls to account for batch variation. Following normalization to FW439, about half of the transformants had a considerably lower relative MFI than the FW706 parent strain (**Figure 3.7A**, CRISPR Round 2), potentially due to the unstable nature of tandem multicopy integrations.[291] Nevertheless, the best clone, FW707, showed nearly a 9-fold increase in MFI over the FW439 strain. The rarity of these "jackpot" clones expressing very high levels of XDH (~1% in each round) would make their identification very laborious, if not impossible, using common but lower-throughput approaches such as Western blot[292,293] or *in vitro* activity assays.[294,295] Therefore, the use of yICS can greatly accelerate the clonal selection process based on the expression level of POIs.

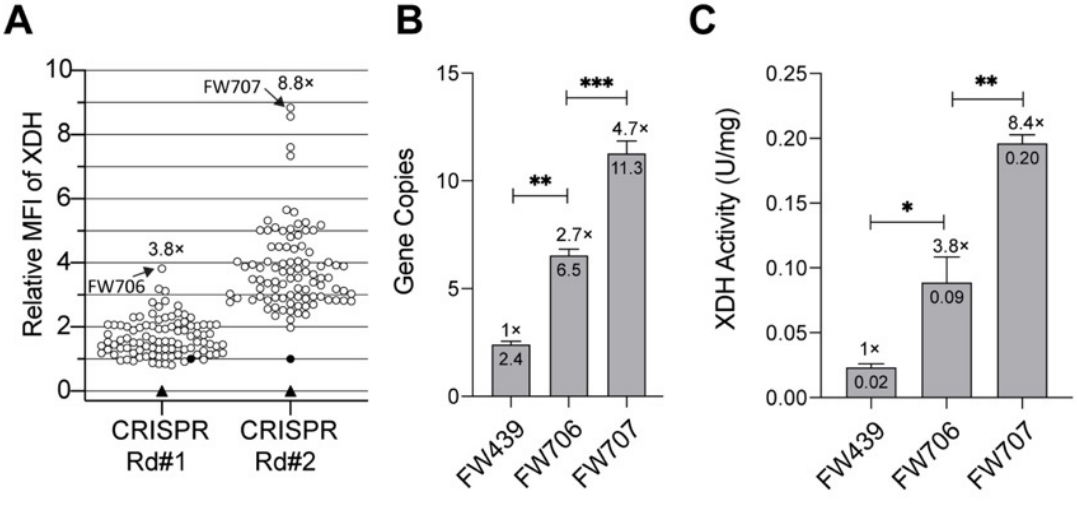

Figure 3.7. yICS identifies rare high-expressing clones in multicopy integration library
(**A**) XDH MFI of clones resulting from CRISPR-mediated integration of XDH expression cassette into FW439 (CRISPR Rd#1) and FW706 (CRISPR Rd#2) normalized to FW439. FW439 and W303-1a are indicated by filled black circles and triangles, respectively. (**B**) XDH gene copy

numbers of selected strains quantified by qPCR. (**C**) Units of XDH activity per mg of protein in cleared cell lysate for selected strains. One unit of XDH activity is defined as the amount of XDH that reduces 1 μmol of NAD^+ to NADH per minute (see methods). Fold change of FW706 and FW707 compared to FW439 is indicated in each figure. For **B** and **C,** data represent mean ± standard deviation, $n = 3$; statistical comparisons computed by one-way ANOVA followed by post hoc Tukey's pairwise comparisons, $*p < 0.05$, $**p < 0.01$, $***p < 0.001$.

Subsequent qPCR analysis of the selected strains revealed that the increase in MFI following each round of CRISPR integration was accompanied by a significant increase in the XDH copy number ($p < 0.01$), with about 4 additional XDH copies being introduced in the highest expressing clone per round (**Figure 3.7B**). Note that within the CRISPR Round 2 library, the best clone, FW707, was confirmed to have two more copies than the second-best clone ($p < 0.05$) highlighting the superb resolution of yICS for identifying subtle changes in POI expression level. The best clones from each CRISPR round were then evaluated for their XDH activity *in vitro* (see methods), revealing a 2-4 fold increase in activity with each round of XDH integration ($p < 0.05$) (**Figure 3.7C**). Taken together, these results demonstrate the ability of yICS to rapidly and accurately identify clones of interest based on protein expression level, reducing the library size to more manageable levels that allow further pathway evaluation using more direct, but typically lower throughput, functional assays such as fermentation.

Accordingly, the selected strains FW706 and FW707 were next subjected to low-throughput anaerobic xylose fermentation to compare their performance to the FW439 parental strain. While strains with higher XDH expression had a slightly increased rate of xylose consumption (**Figure 3.8A**, top), xylitol accumulation was significantly reduced (**Figure 3.8A**, middle), signifying increased *in vivo* activity of XDH. Specifically, xylitol accumulation was reduced by 24% in FW707 compared to FW439 upon xylose depletion (96 hours) (0.516 versus 0.390 g/g xylose consumed, **Figure 3.8B**). More importantly, increased XDH expression led to improved ethanol production (**Figure 3.8A**, bottom) with FW707 achieving a 33% increase in ethanol yield compared to FW439 (0.280 versus 0.210 g/g xylose consumed, **Figure 3.8C**). While these data clearly demonstrate that the XDH activity is indeed a bottleneck in the pathway, they raise the question of whether further increases in XDH activity can continue to drive efficient increases in ethanol yield. To this end, the relative MFI of XDH was plotted against the relative ethanol yield for each strain (**Figure 3.8D**). While the number of data points is small, these data indicate that further XDH integrations will likely lead to diminishing returns and suggest the use of alternative strategies beyond tuning XDH expression to achieve further improvement of xylose-to-ethanol conversion. Taken together, these results demonstrate that the knowledge of protein expression level, as provided by yICS, can give significant insights into clone performance and highlight the use of yICS in the pathway engineering pipeline as a versatile tool that can fulfill both rapid screening as well as detailed strain characterization.

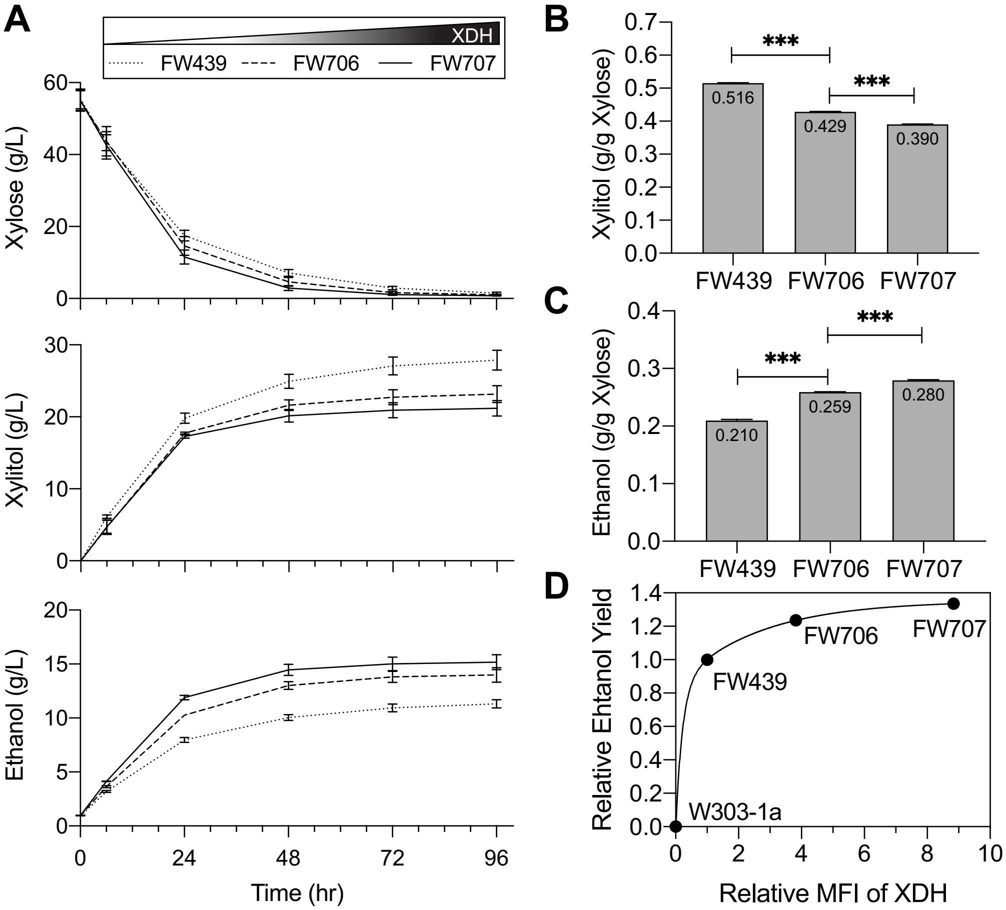

Figure 3.8. Clones identified by yICS screening demonstrate enhanced performance
(**A**) Concentrations of xylose (top panel), xylitol (middle panel), and ethanol (bottom panel) at indicated timepoints during anaerobic xylose fermentation. (**B**) Xylitol and (**C**) ethanol generated at 96 hours of fermentation per xylose consumed (wt/wt). (**D**) Relative ethanol yield versus the relative XDH MFI normalized to FW439 for each strain fit with a two-phase association model. Data in **A**, **B**, and **C** represent mean ± standard deviation, $n = 2$; statistical comparisons computed by one-way ANOVA followed by post hoc Tukey's pairwise comparisons, ***$p < 0.001$.

3.5. Conclusion

In conclusion, foreign protein expression in yeast often requires the ability to efficiently screen large libraries for desirable phenotypes (*e.g.* high expression level). However, current methods for measuring the expression level of intracellular proteins in yeast, such as Western blot, do not have the throughput to handle large libraries. To this end, we developed and demonstrated for the first time a flow cytometric approach that enables the rapid detection and quantification of yeast intracellular POIs *via* antibody staining with little (**Figure 3.6B, C**) to no (**Figure 3.5A**) POI modification. The compatibility of this yICS approach with multi-well plate format enabled the rapid identification of rare (~1%), high producing clones from a multicopy integration library (**Figure 3.7A**), a feat that would have been especially tedious using Western blot. Furthermore, the single-cell resolution of flow cytometry coupled with the diversity of available fluorophores enables multiplexed characterization of several POIs simultaneously (**Figure 3.6B, C**), revealing valuable information on population heterogeneity and the relative ratio of multiple proteins in individual cells. Such a technique will be valuable for the rapid engineering of yeast influenza VLP strains. Aside from the ability to identify clones with high expression levels of HA following multicopy integration, there are numerous possibilities. For example, yeast mutant libraries can be screened to discover genes that increase influenza protein expression levels. Combined with imaging flow cytometry[296] mutations could also be identified that lead to HA plasma membrane localization. Based on these possibilities, we believe that yICS is an incredibly versatile technique with a wide variety of applications.

3.6. Materials and Methods

3.6.1. Strains, Plasmids, Reagents, and Cell Culture Conditions

The strains and plasmids used in this study are summarized in **Table 3.1**. All yeast strains were constructed from *S. cerevisiae* W303-1a (ATCC 208352) as described in **Section 3.6.9**. All chemicals and reagents were purchased from Sigma-Aldrich (St. Louis, MO) unless specified otherwise. Non-plasmid-bearing yeast strains were grown in either YPAD medium (10 g/L yeast extract, 20 g/L peptone, 100 mg/L adenine sulfate, 20 g/L glucose), YPAX medium (10 g/L yeast extract, 20 g/L peptone, 100 mg/L adenine sulfate, 20 g/L xylose), or yeast synthetic complete

(SC) medium (1.67 g/L of yeast nitrogen base (Difco, Detroit, MI), 5 g/L ammonium sulfate, 20 g/L glucose, 100 mg/L adenine sulfate, and 0.64 g/L of CSM (MP Biomedicals, Solon, OH)). Plasmid-bearing yeast strains were grown in appropriate SC dropout medium (same recipe as SC medium except that CSM dropout powder was used in place of the CSM powder). Yeast cells were grown at 30°C in an orbital shaker at 225 RPM unless specified otherwise. Cell concentrations were determined as OD_{600} measurements using a Spectramax M5 plate reader (Molecular Devices, Sunnyvale, CA) and standard curve (1 OD_{600} is calibrated to equal 25 million cells). All centrifugation steps were performed at 3200 × g for 3 minutes.

Table 3.1. Strains and plasmids used in yICS study.

Strain/plasmid	*Description*	*Reference*
Strains		
W303-1a	*MATa, ade2-1, ura3-1, his3-11, trp1-1, leu2-3, leu2-112, can1-100*	ATCC 208352
FW439	W303-1a integrated with XR, XDH and XK	This study
FW706	FW439 integrated with additional XDH	This study
FW707	FW706 integrated with additional XDH	This study
Plasmids		
p414-TEF1p-Cas9-CYC1t	Constitutive expression of Cas9	[297]
p426-SNR52p-gRNA.CAN1.Y-SUP4t	Template for gRNA cassette	[297]
p426gRNA-Delta	gRNA cassette targeting δ site	This study
p423gRNA-Delta	gRNA cassette targeting δ site	This study
p426-XR-XDH-XK	Constitutive expression of XR, XDH, and XK, and the template for XR-XDH-XK donor DNA for δ site integration	This study
p426-XDH	Constitutive expression of XDH	This study
p426-d-XDH-d	Template to obtain XDH donor DNA for δ site integration	
p426-XK	Constitutive expression of XK	This study
p426-XR	Constitutive expression of XR	This study

3.6.2. General yICS Procedure

To perform cell wall removal in 96-well plate format, yeast strains were seeded directly from a single colony into individual wells of the plate and grown for 16 hours at 30°C without shaking. For strains grown in SC or SC dropout medium, colonies were diluted 10-fold before seeding to ensure growth $OD_{600} < 3.7$. Aliquots of 5 million cells (0.2 OD_{600}) were then transferred to wells of another 96-well plate, pelleted, and resuspended in 200 μL of 30mM TCEP (Bond-Breaker™ Thermo Fisher Scientific, Waltham, MA) to reduce disulfide bridges and loosen the cell wall. After incubation at 30°C without shaking for 20 minutes, cells were washed once in MilliQ water (18.2 mΩ•cm at room temperature), resuspended in 200 μL TMS buffer (50 mM Tris-HCl pH 7.4, 5 mM $MgCl_2$, 1 M sorbitol) with 3 mM TCEP and 1280 U/mL of lyticase from *Arthrobacter luteus* and incubated at 30°C without shaking to initiate cell wall removal. To observe the progress of cell wall removal, cells were taken at desired time points and imaged using a Leica TCS SP8 MP inverted confocal microscope (Leica Microsystems, Wetzlar, Germany) in differential interference contrast (DIC) mode. After 60 minutes of lyticase treatment, the resulting spheroplasts were washed twice with 1 M sorbitol and fixed in 200 μL 1 M sorbitol with 0.5% formalin for 30 minutes at room temperature.

The formalin-fixed spheroplasts were then permeabilized in 200 μL saponin-based permeabilization buffer (eBioscience, San Diego, CA) for 30 minutes at room temperature, pelleted, and stained with primary antibodies at desired concentrations in 50 μL permeabilization buffer for 1 hour at room temperature. If a secondary antibody staining was required, spheroplasts were then washed twice in 200 μL permeabilization buffer, resuspended in 50 μL of permeabilization buffer containing the secondary antibody at the desired concentration, and incubated for 1 hour at room temperature. After washing twice in 200 μL permeabilization buffer, spheroplasts were resuspended to 0.5 million spheroplasts/mL in flow buffer (PBS pH 7.4, 0.5% bovine serum albumin) for flow cytometry analysis on either a MoFlow Astrios cell sorter (Beckman Coulter, Indianapolis, IN) or an Attune flow cytometer (Applied Biosystems, Foster City, CA). Flow cytometry data were analyzed using FlowJo (FlowJo LLC, Ashland, OR).

The 1280 U/mL lyticase concentration used for cell wall removal and the 0.5% formalin concentration used for spheroplast fixation were optimized for the specific system reported in this study as detailed in **Figure 3.4** and **Figure 3.5**. Note that both concentrations should be optimized under new experimental conditions such as when investigating a different yeast strain or cell culture condition as detailed below.

3.6.3. Optimization of Lyticase Concentration

5 million (0.2 OD_{600}) yeast cells grown from each new culture conditions are transferred to wells of a 96-well plate, and the cell wall removal protocol is performed as described above except for the following changes: 1) the lyticase digestion step is performed in 200 μL TM buffer without sorbitol (50 mM Tris-HCl pH 7.4, 5 mM $MgCl_2$) to promote spheroplast lysis, 2) varying concentrations of lyticase is added to the TM buffer, and 3) during lyticase digestion, the OD_{600} of the cells is measured and recorded every 30 seconds using a Spectramax M5 plate reader at 30°C with shaking to prevent cell settling. The OD/OD_{init} values are then evaluated to determine the optimal lyticase concentration as illustrated in **Figure 3.4**.

3.6.4. Optimization of Formalin Concentration via Detection of Yeast Housekeeping Proteins

After cell wall removal, spheroplasts are fixed with varying concentrations of formalin. Formalin concentrations of 0.5%, 1%, 2%, or 4% are commonly used in literature for different types of cells.[298,299] Note that other fixation reagents could also be considered[300,301]. Formalin-fixed spheroplasts are then permeabilized and stained for housekeeping proteins such as GAPDH and β actin as described above. The fluorescence intensity of housekeeping proteins and the autofluorescence intensity of the isotype control are next evaluated to determine the optimal formalin concentration as illustrated in **Figure 3A**. In this study, 20 μg/mL of either mouse anti-GAPDH antibody (clone MA5-15738, Invitrogen, Waltham, MA), mouse anti-β actin antibody (clone MA1-744, Invitrogen), or mouse IgG1κ isotype control (clone P3.6.2.8.1, eBioscience) were used as the primary antibodies; 2 μg/mL of PE-conjugated goat anti-mouse antibody (clone Poly4053, BioLegend, San Diego, CA) was used as the secondary antibody.

3.6.5. Detection and Characterization of XR, XDH, and XK

To detect XR, XDH, and XK enzymes all at once, the general yICS procedure was performed for W303-1a, FW439, 3-plasmid, and 1-plasmid strains as described above using a primary antibody cocktail containing 20 μg/mL each of PE-conjugated anti-His (clone J095G46, BioLegend), biotin-conjugated anti-c-myc (clone 9E10, BioLegend), and Alexafluor647-conjugated anti-HA (clone 16B12, BioLegend). Secondary antibody staining was performed with 2 μg/mL PE-Cyanine7-conjugated streptavidin (eBioscience). MATLAB (MathWorks, Natick, MD) was used for three-dimensional visualization of flow cytometry data.

3.6.6. yICS of CRISPR Integration Library

FW439 was first transformed with p414-TEF1p-Cas9-CYC1t (**Table 3.1**) encoding a Cas9 expression cassette (a gift from George M. Church, Addgene plasmid #43802) and plated on SC-TRP. A single colony was picked from the plate and transformed simultaneously with p426gRNA-Delta (**Table 3.1**) encoding the guide RNA targeting the yeast δ site and linearized donor DNA containing the XDH expression cassette flanked by δ sites produced from PCR amplification of p426-d-XDH-d (**Table 3.1**). Transformants were plated on SC-TRP-URA. FW439 and 95 transformants were subjected to the yICS procedure using 20 µg/mL of Alexafluor647-conjugated anti-HA. The clone with the highest XDH expression was designated FW706. A second round of XDH integration into FW706 was performed as described above but with gRNA plasmid p423gRNA-Delta (**Table 3.1**). Transformants were plated on SC-TRP-HIS and screened using yICS to yield the best clone FW707.

3.6.7. Characterization of High XDH-expressing Clones Selected by yICS Screening

The copy number of the XDH gene in strains FW439, FW706, and FW707 was determined using quantitative PCR (qPCR) by comparing the C_T values of the XDH gene to the reference gene phosphoglucose isomerase (PGI1) using previously described methods.[302] qPCR was performed on 7900HT (Applied Biosystems, Warrington, UK) with SYBR Green qPCR Master Mix (Applied Biosystems, Warrington, UK) containing 200 nM of qPCR primers (**Table 3.2**) and 200 ng genomic DNA isolated from each strain using the Wizard Genomic DNA kit (Promega, Madison, WI).

The *in vitro* XR, XDH, and XK activities were evaluated using the cell lysates of strains FW439, FW706, and FW707 prepared by Y-PER treatment (Yeast Protein Extraction Reagent, Pierce, Rockford, IL) following the manufacturer’s protocol. Protein concentrations in cell lysates were determined using the BCA Protein Assay Kit (Thermo Fisher Scientific) following the manufacturer’s protocol. Enzyme activities were determined by adapting previously described methods.[303-305] Briefly, enzyme reactions were carried out at room temperature in 96-well plates in a total volume of 200 µL. XR activity was evaluated in 50 mM potassium phosphate buffer (pH 7), 350 mM D-xylose, 0.02 mM NAD(P)H, and 50 µg cell extract; XDH activity was evaluated in a reaction mixture containing 50 mM Tris buffer (pH 9), 300 mM xylitol, 2 mM NAD^+, and 25 µg cell extract; and XK activity was evaluated in 50 mM Tris buffer at pH 7.5 containing 2 mM magnesium chloride, 8 mM sodium fluoride, 2 mM ATP, 1 mM phosphoenolpyruvate, 3 mM red glutathione, 0.3 mM NADH, 10 units of pyruvate kinase, 10 units of lactate dehydrogenase, 5 mM D-xylulose, and 10 µg cell extract. Reduction of NAD^+ to NADH was monitored continuously by absorbance measurements at 340 nm for 5 min using a SpectraMax M5 plate reader. The absorbance change per minute ($\Delta A\ min^{-1}$) was divided by the molar absorptivity of NAD(P)H ($6.22\ cm^{-1}mmol^{-1}$) to calculate substrate consumption per minute. One unit of enzyme activity is defined as the amount of enzyme that reduces 1 µmol of NAD^+ per minute in the reaction conditions described above.

The xylose-to-ethanol conversion capability of FW439, FW706, and FW707 was evaluated using anaerobic fermentation at 30°C and 225 RPM. 10 OD_{600} of yeast cells were inoculated into anaerobic YPA medium containing 55 g/L xylose with 0.01 g/L ergosterol and 0.4 g/L Tween-80 in an anaerobic chamber and sealed in serum bottles with butyl rubber stoppers. The glucose, xylose, xylitol, glycerol, acetate and ethanol concentrations of fermentation samples were analyzed at indicated time points by high performance liquid chromatography (HPLC, Agilent Technologies 1200 Series, Santa Clara, CA) equipped with a refractive index detector and a Rezex ROA Organic Acid H^+ (8%) column (Phenomenex Inc., Torrance, CA). The column was eluted with 0.005 N H_2SO_4 flowing at 0.6 mL/min at 60°C.

3.6.8.Plasmid Construction

Primers were synthesized by Integrated DNA Technologies (Coralville, IA) and listed in **Table 3.2**. All plasmids were constructed using either the DNA assembler method based on homologous recombination in W303-1a[231] or ligating the target genes into digested plasmid backbones in *Escherichia coli* strain Mach1 (Thermo Fisher Scientific, Waltham, MA). Restriction enzymes and DNA polymerase were purchased from New England Biolabs (Beverly, MA). Yeast-assembled plasmids were isolated using Zymoprep II Yeast Plasmid Miniprep kit (Zymo Research, CA). Plasmids were isolated from *E. coli* using QIAprep Spin Miniprep Kits (Qiagen, Hilden, Germany). *E. coli* was grown in LB medium (Sigma-Aldrich, St. Louis, MO) at 37°C in an orbital shaker at 225 RPM. LB was supplemented with 50 µg/mL ampicillin for plasmid propagation.

Construction of p426-XR-XDH-XK: Plasmid p426-XR-XDH-XK contains expression cassettes for XR, XDH, XK, and the KanMX resistance gene flanked by δ homology sequences that enable genomic integration into yeast δ sites. Fragments Delta-Left, Delta-Right, promoters (*TEF1, PGK1* and *PYK1*), and terminators (*ADH1, CYC1* and *ADH2*) were PCR amplified from *S. cerevisiae* W303-1a genomic DNA (**Table 3.2**). The KanMX cassette was amplified using plasmid pRS-TEFp-KanMX-TEFt as a template (a gift from Zengyi Shao, Iowa State University). The genes for XR, XDH, and XK were amplified from *S. stipitis* genomic DNA. All PCR fragments were assembled into plasmid pRS426 linearized with *XhoI* and *NotI* using the DNA assembler method. W303-1a cells were transformed with p426-XR-XDH-XK by electroporation and plated on SC-URA.

Construction of single gene plasmids p424-XR, p425-XK, and p426-XDH: Expression cassettes for XR, XK, and XDH were PCR-amplified from plasmid p426-XR-XDH-XK and cloned into plasmids pRS424, pRS425, and pRS426, respectively, by digestion and ligation using restriction enzymes listed in **Table 3.2**. W303-1a cells were transformed with p424-XR, p425-XK, and p426-XDH by electroporation and plated on SC-TRP, SC-LEU, and SC-URA, respectively.

Construction of p426gRNA-Delta and p423gRNA-Delta plasmids: The p426gRNA-Delta and p423gRNA-Delta plasmids generate a guide RNA (gRNA) for the Cas9 nuclease that is specific for the *S. cerevisiae* δ site with the sequence *tatactagaagttctcctcg*. To produce plasmid p426gRNA-Delta, fragments gRNA F1 and gRNA F2 (**Table 3.2**) were PCR amplified from SNR52p-gRNA.CAN1.Y-SUP4t[2] (a gift from George M. Church, Addgene plasmid #43803), assembled by overlap extension PCR[3], and ligated into p426-SNR52p-gRNA.CAN1.Y-SUP4t after digestion with *NheI* and *BsrGI*. Plasmid p423gRNA-Delta was generated by PCR amplification of the gRNA fragment using g426RNA-Delta plasmid as template (**Table 3.2**). The amplified fragment, gRNA F3, was ligated into p423 after digestion with *SalI* and *NotI*.

Construction of p426-d-XDH-d: Fragments Delta-Left and Delta-Right were PCR amplified from *S. cerevisiae* W303-1a genomic DNA (**Table 3.2**). The XDH expression cassette was PCR amplified from plasmid p426-XR-XDH-XK. All PCR fragments were assembled into plasmid pRS426 linearized with *XhoI* and *NotI* using the DNA assembler method.

3.6.9. Strain Construction

3-plasmid strain: W303-1a was transformed with p424-XR, p425-XK, and p426-XDH and plated on SC-URA-LEU-TRP.

1-plasmid strain: W303-1a was transformed with p426-XR-XDH-XK and plated on SC-URA.

FW439 strain: W303-1a was integrated with the XR, XDH, and XK expression cassette by conventional integration methods.[231,306] Briefly, plasmid p426-XR-XDH-XK was digested with *KpnI* and *NotI* to obtain an expression cassette containing all three enzymes and the KanMX gene flanked by the δ homology arms. This fragment was transformed into W303-1a by electroporation and the transformants were plated on YPAD containing 200 mg/mL G-418 selection (Life Technologies, Carlsbad, CA). Of the resulting colonies, one was found to have a high level of XDH activity using the XDH enzyme activity assay and was designated FW439.

Strains FW706 and FW707: Strains FW706 and FW707 were produced by CRISPR-mediated integration of XDH into the yeast δ site followed by yICS screening as described above.

Table 3.2. Primers used in cloning of yICS constructs

Description	Amplicon	PCR Template	Homologous Recombination (HR) or Digestion and Ligation (DL)	Plasmid Backbone	F/R	Sequence (5'-3')
p426gRNA-Delta	gRNA F1	p426-SNR52p-gRNA.CAN1.Y-SUP4t**	DL, NheI/BsrGI	p426-SNR52p-gRNA.CAN1.Y-SUP4t** digested with NheI/BsrGI	F	CAACTCTAGATTTTGTAGTGCCCTCTTGGGCTAGCGGTAAAGGTGCGCAT
					R	GATCATTTATCTTTCACTGCGGAGAAGTTT
	gRNA F2	p426-SNR52p-gRNA.CAN1.Y-SUP4t**			F	GAAACTTCTCCGCAGTGAAAGATAAATGATCGTATACTAGAAGTTCTCCTCGGTTTTAGAGCTAGAAATAGCAAGT
					R	ATAATGTTACATGCGTACACGCGTCTGTACAGAAAAAAAAGAAAAATTTGAAATA
p423gRNA-Delta	gRNA F3	p426gRNA-Delta	DL, SalI/NotI	pRS423 digested SalI/NotI	F	CGAGGTCGACTCTTTGAAAAGATAATG
					R	GTGGCGGCCGCCCGCAAATTAAAGCCTTC
p426-XR-XDH-XK	Delta - Left	W303-1a Genomic DNA	HR	pRS426 digested with XhoI/NotI	F	CTATAGGGCGAATTGGGTACCGGGCCCCCCCTAGGTGGAAGCTGAAACGTCTAACGGAT
					R	GTAAAAAAGGAGTAGAAACATTTTGAAGCTATCCCGGGGAGAACTTCTAGTATATTCTGT
	TEF1p	W303-1a Genomic DNA	HR		F	ACAGAATATACTAGAAGTTCTCCCCGGGATAGCTTCAAAATGTTTCTACTCCTTTTTTAC
					R	TCTTCTCCTTTTTGGTGGCAGAGCAGGAGGAGGCATTTTGTAATTAAAACTTAGATTAGA
	XR	*Scheffersomyces stipitis* Genomic DNA	HR		F	TGCTCTGCCACCAAAAAGGAGAAGACATCATCACCATCACCATCCTTCTATTAAGTTGAA
					R	AAACCTCTGGCGAAGAAGTCCAAAGCTTTAGACGAAGATAGGAATCTTGTCCCAGTCCCA
	ADH1t	W303-1a Genomic DNA	HR		F	TGGGACTGGGACAAGATTCCTATCTTCGTCTAAAGCTTTGGACTTCTTCGCCAGAGGTTT
					R	TCTGTGCGTCTTGAGTTGAAGTCAGGAATCCATGCCGGTAGAGGTGTGGTCAATAAGAGC
	PGK1p	W303-1a Genomic DNA	HR		F	GCTCTTATTGACCACACCTCTACCGGCATGGATTCCTGACTTCAACTCAAGACGCACAGA
					R	GGAAGGGTTAGCAGTCATTGTTTTATATTTGTTG
	XDH	*Scheffersomyces stipitis* Genomic DNA	HR		F	CAACAAATATAAAACAATGACTGCTAACCCTTCC
					R	ACTAATGATTCTTTCACGCCAGCATAATCTGGAACATCATATGGATACTCAGGGCCGTCAATGAGACACTTG
	CYC1t	W303-1a Genomic DNA	HR		F	AGATTATGCTGGCGTGAAAGAATCATTAGTATAAATCATGTAATTAGTTATGTCACGCTT
					R	ACTGAGATTAATCTCCAAAATAGTAGCATTGCAAATTAAAGCCTTCGAGCGTCCCAAAAC
	PYK1p	W303-1a Genomic DNA	HR		F	GTTTTGGGACGCTCGAAGGCTTTAATTTGCAATGCTACTATTTTGGAGATTAATCTCAGT
					R	CAAATGGGGTAGTGGTCATTGTGATGATGTTTTATTTG
	XK	*Scheffersomyces stipitis* Genomic DNA	HR		F	CAAATAAAACATCATCACAATGACCACTACCCCATTTG
					R	TGAGCCTCCACCTCCGGAGCCTCCACCTCCTGAGTGTTTCAATTCACTTTCCATCTTGGC
	ScaA	*Ruminococcus flavefaciens* Genomic DNA	HR		F	TCAGGAGGTGGAGGCTCCGGAGGTGGAGGCTCAGGAGGTGGAGGCTCACCCGGCACAAAGCTCGTTCCTACATGGGGCGATAC
					R	CAAACCTTACAAGTCCTCTTCAGAAATGAGCTTTTGCTCCTGAGGAAGTGTGATGAGTTC
	ADH2t	W303-1a Genomic DNA	HR		F	GAGCAAAAGCTCATTTCTGAAGAGGACTTGTAAGGTTTGCTGAGAAGCTTGCCAAATGATTG
					R	ATAACTTCGTATAGCATACATTATACGAAGTTATGGATCCAGCTACTAATAGGATAAATTATAG
	TEF2p-KanMX- TEF1t	pRS-TEFp-KanMX-TEFt plasmid	HR		F	CTTCGTATAATGTATGCTATACGAAGTTATATGGGTAAGGAAAAGACTCACGTTTCGAGG
					R	CTTCGTATAGCATACATTATACGAAGTTATATTAAGGGTTCTCGAGAGCTCGTTTTCGAC
	Delta - Right	W303-1a Genomic DNA	HR		F	ATAACTTCGTATAATGTATGCTATACGAAGTTATCTCGAGGATATAGGAATCCTCAAAAT
					R	AAGCTGGAGCTCCACCGCGGTGGCGGCCGCTGTTGGAATAGAAATCAACTATCATCTACT
p426-d-XDH-d	Delta - Left	W303-1a Genomic DNA	HR	pRS426 digested with XhoI/NotI	F	CTATAGGGCGAATTGGGTACCGGGCCCCCCCTAGGTGGAAGCTGAAACGTCTAACGGAT
					R	GCGTCTTGAGTTGAAGTCAGGAATCGAGAACTTCTAGTATATTCTGTATA
	PGK1p-XDH-CYC1t	p426-XR-XDH-XK	HR		F	TATACAGAATATACTAGAAGTTCTCGATTCCTGACTTCAACTCAAGACGC
					R	TTTGAGGATTCCTATATCCTCGAGGCAAATTAAAGCCTTCGAGCGTCCCA
	Delta - Right	W303-1a Genomic DNA	HR		F	TGGGACGCTCGAAGGCTTTAATTTGCCTCGAGGATATAGGAATCCTCAAA
					R	CCCTCACTAAAGGGAACAAAAGCTGGAGCTCCACCGCGGTGGCGGCCGCTGTTGGAATAGAAATCAACTATCATCTAC
p426-XDH	PGK1p-XDH-CYC1t	p426-XR-XDH-XK	DL, XhoI/XmaI	pRS426 digested with XhoI/XmaI	F	CCCCCCCTCGAGGATTCCTGACTTCAACTCAA
					R	GGATCCCCCGGGGCAAATTAAAGCCTTCGAGC
p425-XK	PYK1p-XK-ADH2t	p426-XR-XDH-XK	DL, XhoI/BamHI	pRS425 digested with XhoI/BamHI	F	CCCCCCCTCGAGGATTCCTGACTTCAACTCAA
					R	AACTAGTGGATCCAGCTACTAATAGGATAAATT
p424-XR	TEF1p-XR-ADH1t	p426-XR-XDH-XK	DL, XhoI/BamHI	pRS424 digested with XhoI/BamHI	F	CCCCCCCTCGAGATAGCTTCAAAATGTTTCTA
					R	TAGTGGATCCCATGCCGGTAGAGGTGTGGT
XDH Donor DNA	d-XDH-d	p426-d-XDH-d	N/A	N/A	F	TGGAAGCTGAAACGTCTAACGGATC
					R	TGTTGGAATAGAAATCAACTATCATC
qPCR primers	XDH	N/A	N/A	N/A	F	CCACTTCTACGCCCATGGTAGAAT
					R	GTCACCAACCTTAAGAGAGGTGACA

Chapter 4. Mass Cytometry Enables In-depth Characterization of Immune Landscape Upon Influenza Virus Infection

4.1. Publication Information.

Hill, B. D., Zak, A. J., Raja, S., Rizvi, S. M., Bugada, L. F., Roslan, S., Jiang, H., Goldstein, D.R., Wen, F. Single-cell Immune Landscape of Influenza Virus Infection: Implications of Aging and Genetic Background. (*In Prep*)

The goal of this chapter is to validate mass cytometry for rapidly and comprehensively characterizing an immune response. While relevant to numerous applications, such an approach is especially useful for vaccine development including the testing of yeast derived influenza VLP. Many individuals assisted in this project. Andrew Zak performed all mouse work and assisted in the single-cell infectivity analysis. Sanjeev Raja developed the probabilistic SVM classifier under the guidance of Dr. Hui Jiang. Dr. Syed Monem Rizvi performed antibody staining and ran samples on the CyTOF mass cytometer. Luke Bugada and Saiful Roslan assisted with figure generation. This work was performed in collaboration with Daniel Goldstein M.D. who advised experimental design and assisted in the interpretation of results.

4.2. Abstract

The ability to comprehensively assess an immune response is critical for discovering immune mechanisms that lead to protection as well as evaluating vaccine candidates that aim to elicit these protective responses. In this work we demonstrate the ability of mass cytometry (CyTOF) to comprehensively characterize the early response to influenza virus infection in the lungs of young and aged mice. To aid in the evaluation of such a large dataset, we developed a probabilistic SVM classifier that enables efficient, automated gating of cells into 24 highly specific cellular subsets. Analysis of the resulting data captured in detail the highly inflammatory response on day 3 post infection and its transition to the early adaptive immune response on day 6 post infection. In addition to tracking dynamic changes in cell populations, we developed an experimental procedure that preserves cytokine expression of cells activated *in vivo*. This approach revealed the significant contribution of effector T cells to the overall production of interferon gamma (IFNg), interleukin-10 (IL-10), and tumor necrosis factor alpha (TNFa) in the lung. Moreover, we quantitatively determined the susceptibility of the 24 immune subsets to viral infection and viral replication, revealing that monocytes and macrophages are the least susceptible cells to viral replication while neutrophils and CD11b+ dendritic cells are the most susceptible. We further correlated this susceptibility to low expression of both the activation marker CD69 and the interferon-inducible marker CD317 (*i.e.,* tetherin).

In comparison to young mice, we observed that aging resulted in reduced cellular infiltration of nearly all cellular subsets in response in influenza virus infection. In particular, aged CD8 effector memory (EM) T cells were at half the levels of their young counterparts. In addition,

activation and cytokine production by effector T cells and natural killer T cells (NKT) was severely reduced in aged mice. Despite all the deficiencies associated with aging, upregulation of type I IFN response – as indicated by CD317 – was largely unaffected by aging, displaying nearly identical levels to young mice. Furthermore, aging did not result in significant changes in the susceptibility of cell subsets to viral replication. Overall these results demonstrate the substantial depth and breadth of the immune response that can be revealed by CyTOF analysis.

4.3. Introduction

Despite being the topic of enormous research interest and funding, a broadly protective universal influenza vaccine remains elusive. A key problem for the development of such a vaccine is that surprisingly little is known about what mechanisms lead to the generation of long-term immunity. For example, it has been largely assumed that the genetic drift of influenza virus is responsible for its ability to re-infect individuals from season to season, however recent evidence suggests that young healthy individuals can be re-infected with the same exact influenza strain one year later.[307] This finding is not just limited to influenza. Immunity towards circulating *betacoronaviruses* – the viral genus of SARS CoV2 and other viruses the cause the common cold[308] – also wanes appreciably within one year,[309] rendering the host susceptible to reinfection with the same coronavirus strain.[310] These findings emphasize a gap in our understanding of why some infections and vaccines lead to a durable, protective immune response (*e.g.,* measles, hepatitis B, and smallpox vaccines) whereas others only provide short-term immunity. Thus, a better understanding of protective immune responses and the mechanisms through which they are generated is critical for the development of next generation vaccines to combat influenza virus and other diseases.

The elucidation of protective immune signatures requires comprehensive evaluation of the immune response. However, due to the incredible complexity of the immune landscape, it has been challenging to comprehensively characterize an immune response following infection or vaccination. Technological limitations have restricted studies to either bulk measurements with limited resolution (*e.g.,* serum antibody levels) or highly focused investigations into specific immune components (*e.g.*, individual cellular subsets). While much progress has been made using these methods, they fail to provide a holistic, systems-level understanding of how cellular systems operate in concert to eliminate pathogens. In contrast, the recent advent of "omics" approaches – genomics, transcriptomics, proteomics, *etc.* – now allow high-dimensional measurements to be performed on an unprecedented number of biological variables, enabling the global architecture of biological systems to be revealed with extraordinary resolution and breadth.[311] These powerful systems immunology approaches, combined with computational and machine learning tools to extract meaning from the resulting high-dimensional datasets, have revealed new insights into methods of stimulating and shaping the immune response,[312-314] ultimately enabling a more methodical and predictive approach to vaccine design.

In this work we apply time-of-flight mass cytometry (CyTOF) to comprehensively profile the immune response to influenza infection in young and aged mice. Compared to conventional fluorescence-based flow cytometry approaches, which are limited to the measurement of < 20 markers,[315] CyTOF allows for the simultaneous detection of ~40 unique biomarkers on single cells with minimal channel spillover.[316] This technology enabled us to quantitatively track 24 cellular subsets over the course of influenza virus infection including their expression of activation, cytokine, and influenza-related markers, making this study the most comprehensive flow-based analysis of the influenza immune landscape to date. To support the rapid analysis of such a large high-dimensional dataset and to reduce human bias, we also developed a customizable and automated gating approach based on a probabilistic support vector machine (SVM) classifier to enable efficient, automated classification of 29 million cells into the 24 defined cellular subsets with high accuracy (96%). In addition to anticipated changes in cellular subsets, we also identified dynamic changes in cell types not traditionally associated with viral infection. We also tracked the expression of several functional markers. Notably, we were able to detect cytokine production in cells without *ex vivo* stimulation, giving an accurate snapshot of cytokine production resulting from *in vivo* activation. Furthermore, influenza marker expression data revealed that cell types possess differential susceptibilities to influenza virus infection and replication. Moreover, the data also revealed significant discrepancies in immune cell infiltration, cellular activation, and cytokine production due to aging. Taken together, we show that such a high-resolution approach, combined with high-dimensional data analysis methods, permits a systems-level exploration of the immune landscape, laying the groundwork for future testing of conventional and experimental influenza vaccines.

4.4.Results and Discussion

4.4.1. SVM Classifier Enables Efficient Automated Gating of Large High-dimensional CyTOF Dataset

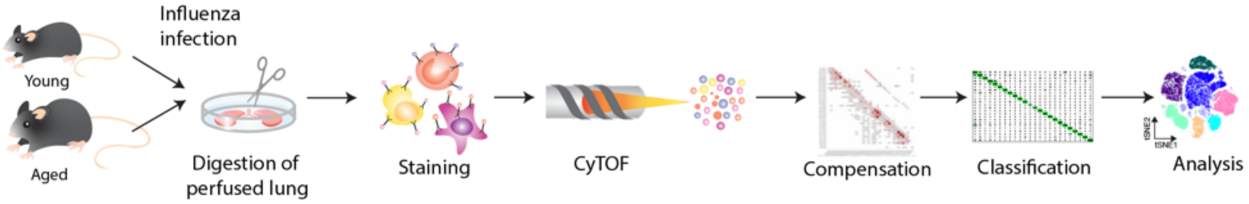

Figure 4.1. Experimental design and data analysis approach
Young (9 weeks) and aged (76 weeks) C57BL/6 mice were intranasally infected with H1N1 A/PR/8/34 virus. Perfused lungs were harvested at 3- or 6-days post infection (*n* = 10 per group), stained with a 40-marker panel, and analyzed by CyTOF. After correcting for channel spillover

and pre-gating to obtain live singlets, cells were classified into 24 cellular subsets using a probabilistic SVM classifier.

Preliminary experiments revealed that aging results in decreased survival following influenza viral infection (**Appendix B.1**). In order to investigate differences in the immune response with aging, young (9 weeks) and aged (76 weeks) C57BL/6 mice were intranasally infected with 1.2×10^4 PFU of H1N1 A/PR/8/34 virus (**Figure 4.1**). Lungs from mock-treated mice (PBS) and infected mice were perfused and harvested at 3- or 6-days post infection (n = 10 per group) and homogenized into single cell suspension. Following ficoll gradient purification to remove dead cells and debris, remaining cells were stained with a 40-marker panel purposefully designed to identify 24 diverse immune cell subsets from both myeloid and lymphoid lineages (**Table 4.1**) including markers for activation, cytokine, and influenza-specific proteins (**Appendix B.2**). Approximately 0.5 to 1.0 million cells were acquired by CyTOF per sample, and resulting events were compensated to account for spillover due to metal impurities.[317] After gating to remove debris, dead cells, and doublets (**Appendix B.3**), 29 million CD45+ live cells remained for data analysis.

Table 4.1. Immune subsets identified by CyTOF and their marker definitions

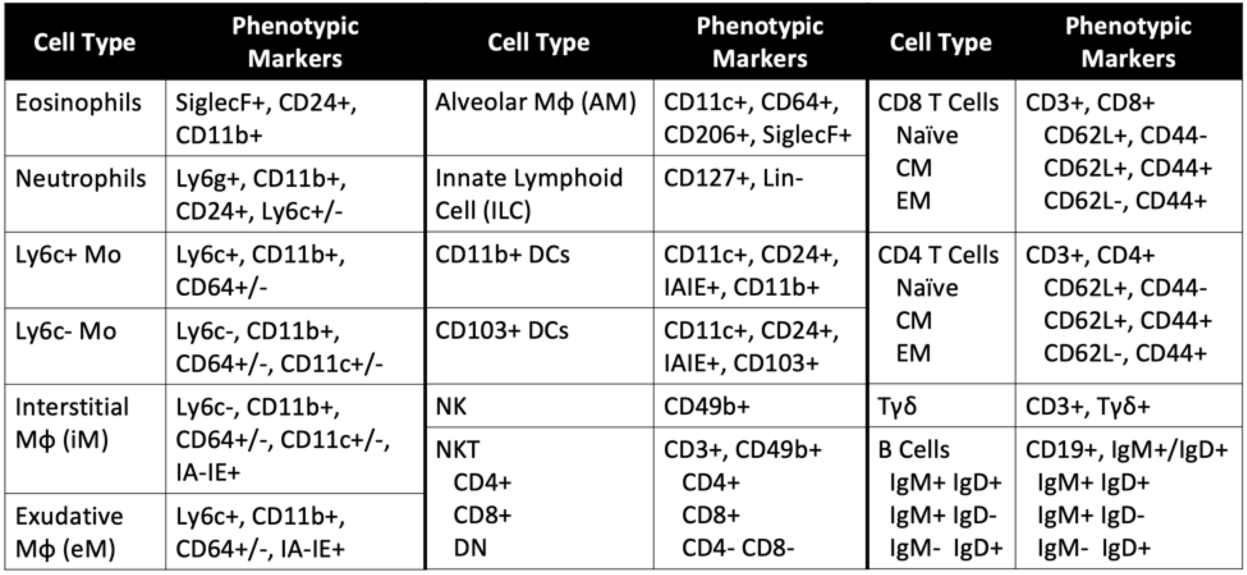

Cell Type	Phenotypic Markers	Cell Type	Phenotypic Markers	Cell Type	Phenotypic Markers
Eosinophils	SiglecF+, CD24+, CD11b+	Alveolar Mϕ (AM)	CD11c+, CD64+, CD206+, SiglecF+	CD8 T Cells Naïve CM EM	CD3+, CD8+ CD62L+, CD44- CD62L+, CD44+ CD62L-, CD44+
Neutrophils	Ly6g+, CD11b+, CD24+, Ly6c+/-	Innate Lymphoid Cell (ILC)	CD127+, Lin-		
Ly6c+ Mo	Ly6c+, CD11b+, CD64+/-	CD11b+ DCs	CD11c+, CD24+, IAIE+, CD11b+	CD4 T Cells Naïve CM EM	CD3+, CD4+ CD62L+, CD44- CD62L+, CD44+ CD62L-, CD44+
Ly6c- Mo	Ly6c-, CD11b+, CD64+/-, CD11c+/-	CD103+ DCs	CD11c+, CD24+, IAIE+, CD103+		
Interstitial Mϕ (iM)	Ly6c-, CD11b+, CD64+/-, CD11c+/-, IA-IE+	NK	CD49b+	Tγδ	CD3+, Tγδ+
Exudative Mϕ (eM)	Ly6c+, CD11b+, CD64+/-, IA-IE+	NKT CD4+ CD8+ DN	CD3+, CD49b+ CD4+ CD8+ CD4- CD8-	B Cells IgM+ IgD+ IgM+ IgD- IgM- IgD+	CD19+, IgM+/IgD+ IgM+ IgD+ IgM+ IgD- IgM- IgD+

Compared to unsupervised data analysis approaches (*e.g.,* Phenograph,[318] SPADE,[319] and CITRUS[320]), supervised analyses can be advantageous for better extracting biological meaning in well-defined systems by tracking changes in canonical cell populations. Given that our panel was designed to identify cellular subsets known to play a crucial role in the immune response to influenza, we pursued a supervised approach. The most traditional form of supervised analysis, manual gating of cells on biaxial plots into user-defined subsets, is highly time-consuming, subjective, and not scalable to very large datasets such as those generated by mass cytometry. To address these shortcomings and facilitate rapid, reproducible data processing, we developed an automated gating framework based on a Support Vector Machine (SVM) classifier.[321] Given a set of training data with class labels, SVM learns hyperplanes (*i.e.*, linear decision boundaries) that optimally divide the data by user-defined classes. Following training and validation, the classifier can be deployed on large datasets in a computationally efficient manner, enabling rapid classification into cellular subsets. The complex and highly heterogeneous nature of the immune landscape inevitably leads to the presence of numerous non-canonical and boundary cell populations, a situation that is exacerbated in mass cytometry due to the granularity and high resolution afforded by the large number of detected markers. In order to accommodate this complexity, we modified the classical SVM classifier by incorporating a rejection option following classification based on posterior probabilities (**Appendix B.9**). In this scheme, the posterior probability of each cell belonging to its predicted class is computed, and cells not meeting a set probability threshold are rejected. Such an approach has the added benefit of providing finer control over the classification, enabling the user to balance classification accuracy and the proportion of rejected cells by fine-tuning the posterior probability threshold (**Appendix B.4**).

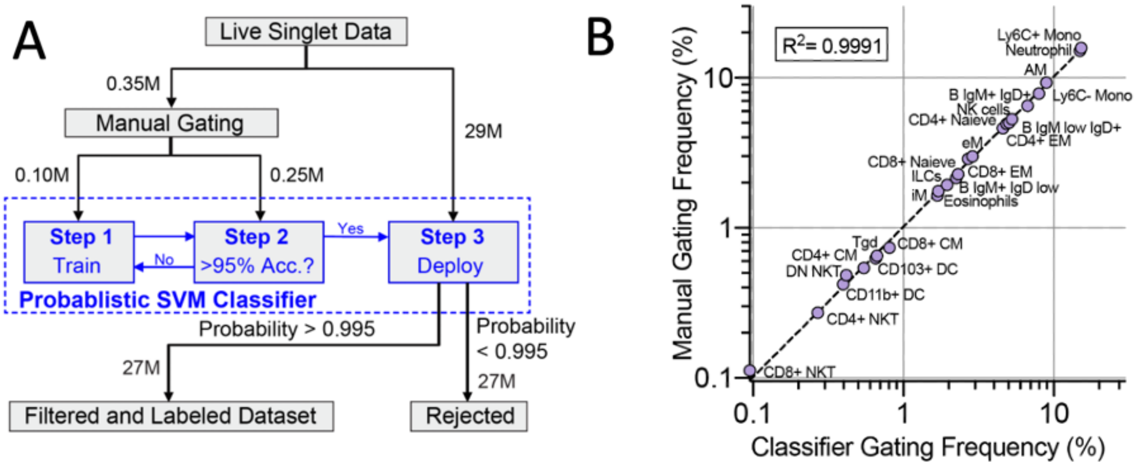

Figure 4.2. SVM classifier training and comparison to manual gating
(**A**) Analysis pipeline for probabilistic SVM classifier training and dataset classification. Following SVM classification, cells with probability < 0.995 of belonging to a class were removed from analysis. (**B**) Comparison of manual gating and SVM classifier gating reveals high accuracy of SVM classifier.

To establish ground truth for classifier training, 350,000 cells were uniformly sampled and manually gated into 24 cellular subsets. The probabilistic SVM classifier was trained on 100,000 of these cells and subsequently validated on the remaining 250,000 (**Figure 4.2A**). The classifier achieved a validation accuracy of 96.4%, and the confusion matrix reveals that most per-class accuracies are above 95% (**Appendix B.5**), with most large off-diagonal terms corresponding to misclassifications between similar cellular subsets such as CD4 and CD8 effector memory (EM) T cells. Note that no cells were rejected based on posterior probabilities in these validation results, which thus constitutes a worst-case estimate of classifier performance. Comparison of cell type frequencies resulting from manual gating and SVM classification revealed that the classifier achieves a high degree of accuracy across a frequency range encompassing nearly two orders of magnitude (**Figure 4.2B**), validating its use for the identification of both abundant and rare cell populations. Consequently, the classifier was deployed on the entire 29 million cell dataset, and the resulting cell label predictions were used in all subsequent analysis. It was found that a posterior probability threshold of 0.995 yielded a cell rejection rate of 7% (**Appendix B.4**), which is consistent with the 5-10% rejection rate resulting from manual gating. Thus, this threshold was chosen for analysis of the entire dataset. Note that the optimal threshold will vary across datasets and should be tuned according to the needs of a given analysis. These data will be explored in the following sections.

4.4.2. Deep Profiling of Immune Subsets During Influenza Infection in Young Mice

We chose to first comprehensively characterize the immune response in young C57BL/6 mice (C57Y) as a baseline for subsequent comparison to aged C57BL/6 (C57A) mice. A systems-level map of the immune landscape was generated *via* the viSNE (visual stochastic neighbor embedding)[322] dimensionality reduction algorithm (**Figure 4.3A**) based on preselected phenotypic markers (**Appendix B.6**). When the viSNE is colored by the SVM cellular classifications, the SVM cell types separate into distinct areas of the map, demonstrating that SVM classification based on manually gated subsets is largely in agreement with the unsupervised viSNE approach. To gain a preliminary understanding into cellular changes over the course of influenza virus infection, the viSNE map was overlaid with cell density contour plots representing day 0, day 3, or day 6 C57Y samples (**Figure 4.3B**). Influenza virus infection led to rapid lung inflammation as observed by substantial increases in monocyte/macrophage (dark blue) and neutrophil (purple) frequencies while alveolar macrophage (AM) frequencies (dark green) were substantially diminished.

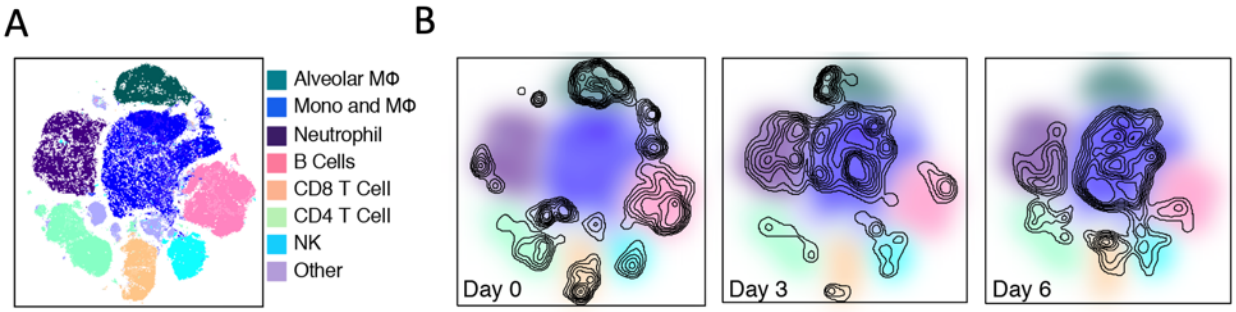

Figure 4.3. High-level overview of changing immune landscape revealed by ViSNE
(**A**) Immune landscape revealed by ViSNE analysis. Cells are colored based on broad classifications from Table 4.1. (**B**) Density plots representing cellular distribution on day 0 (mock), day 3, and day 6 post infection overlaid on viSNE plot reveals substantial changes in immune cell composition over the course of infection.

Next, cell-type frequency information was combined with lung cell counts to obtain absolute changes in lung cellular makeup over the indicated time points (**Figure 4.4A**). Significant immune cell infiltration is observed, with CD45+ cells more than doubling by day 3 ($p < 0.05$) and nearly tripling by day 6 ($p < 0.01$) compared to day 0. Inflammatory monocytes, macrophages and neutrophils primarily drive the increase in cellularity, whereas lymphoid lineage cells contribute relatively little to total cellular accumulation. Furthermore, it can be observed that the kinetics of cellular accumulation differs by cell type. For example, neutrophil counts peak on day 3 while monocytes and macrophages continue to increase through day 6.

Following this preliminary analysis, the broad cellular classes were subdivided into the 24 highly specific cellular subsets (definitions in **Table 4.1**) to gain a high-resolution snapshot of the changing immune landscape. Cell subset counts per mouse lung spanned nearly four orders of magnitude, and the increased resolution reveals several additional cellular subsets undergoing dynamic changes in response to influenza viral infection such as effector memory (EM) T cells, eosinophils, and dendritic cell (DC) subsets (**Figure 4.4B**). To better observe changes in cellular expansion or depletion, the fold changes in absolute cell counts compared to day 0 (hereafter referred to as the accumulation score) were computed for all subsets **(Figure 4.4C)**. On day 3, phagocytic cell types had the highest infiltration scores, (**Figure 4.4C**, light blue bars), with exudative macrophages (eM, *i.e.,* monocyte-derived dendritic cells), Ly6C+ monocytes (Ly6C+ Mo), and neutrophils increasing approximately 30-fold, 10-fold, and 7-fold, respectively. More modest increases were observed in other innate immune cell populations including interstitial macrophages (iM), Ly6C- monocytes (Ly6C- Mo), and natural killer (NK) cells. In contrast, many cellular subsets involved in the adaptive immune response, such as T cell subsets (with the exception of EM populations), DCs, and B cells were depleted, likely due to their trafficking to draining lymph nodes.

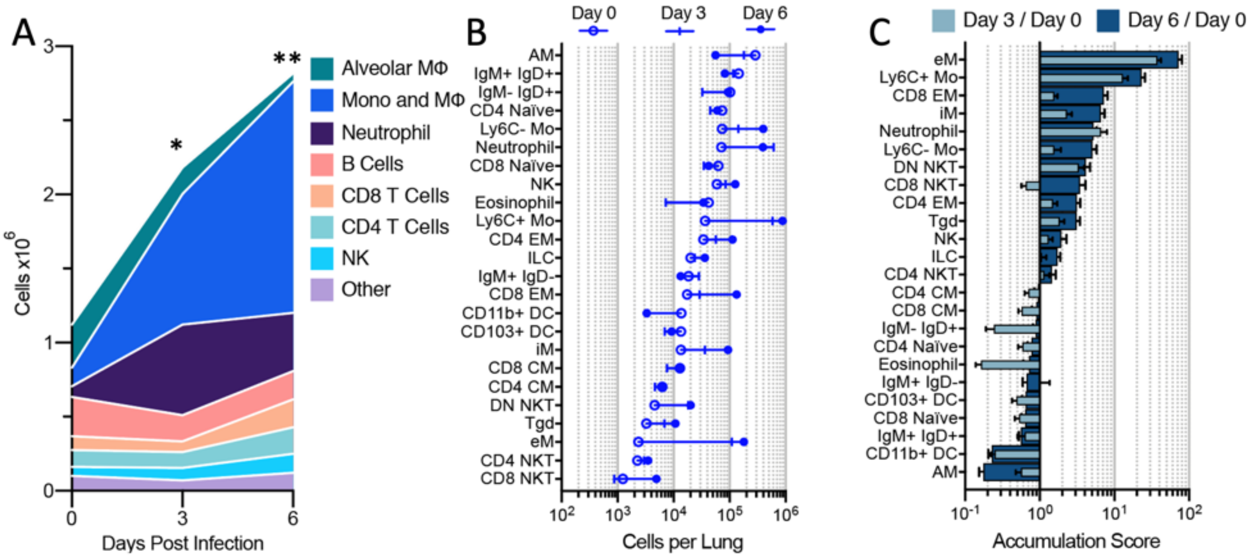

Figure 4.4. Quantitative analysis of changing immune subsets
(**A**) Absolute cell counts of broad cell classifications on day 0, day 3, and day 6 indicate substantial immune infiltration. Indicated significance is in reference to day 0. (**B**) Mean absolute cell counts of 24 cellular subsets on day 0, day 3, and day 6. Cell types are ordered based on day 0 frequencies. (**C**) Mean fold change in absolute cells for each cell type compared to day 0 (accumulation score). Cell types ordered based on day 6 accumulation score. Data represent mean ± SEM, $n = 10$; statistical comparisons in (A) computed by two-tail T test, $*p < 0.05$, $**p < 0.01$, $***p < 0.001$.

At day 6, accumulation of inflammatory subtypes waned whereas strong increases in CD8+ EM T cells (8-fold), Ly6C- Mo (6-fold), and iM (7-fold) were observed. Ly6C- Mo and iM macrophages are suggested to play a role in tissue repair as opposed to their inflammatory Ly6C+ Mo and eM counterparts.[323] Therefore, their accumulation along with CD8 EM T cells on day 6 indicates a transition from the non-specific inflammatory response towards an influenza-specific adaptive response. While the aforementioned changes in cellular subsets are largely consistent with literature,[324] we unexpectedly observed large changes in gamma delta T cells (Tgd) and eosinophils, cell types not traditionally associated with clearance of viral infections. Eosinophils, in particular, displayed complex behavior, decreasing nearly 10-fold on day 3 before rebounding back to basal levels on day 6. Such dynamic behavior of Tgd and eosinophils suggests a potentially unappreciated role for these cell types in the antiviral immune response.

In addition to the granular changes in cellular composition, cellular populations undergo dynamic alterations in marker expression to interact and respond to their environment. Thus, we next evaluated changes in activation (CD69 and CD25), cytokine (Granzyme B, TNFa, IFNg, IL-10, IL-4), and interferon-inducible (CD317) markers in bulk CD45+ cells (**Figure 4.5A**). Positive gates were set according to functional marker expression on day 0 samples (**Figure 4.5A**, top row). As expected, the frequency of CD69, CD25, Granzyme B (GzmB), and CD317 positive cells was significantly increased on days 3 and 6 compared to day 0 mice, demonstrating cellular activation and the initiation of effector functions in response to viral infection. Notably, although we did not stimulate cells *ex vivo,* we were also able to detect cytokine producing cells, enabling a real-time snapshot of *in vivo* cytokine production in single cells that has rarely been investigated. Day 0 mice predominantly expressed the cytokine interleukin (IL) 4, indicating the basal level lung environment is skewed towards a Th2-type response. Upon infection, IL-4 positive cells dropped precipitously, giving rise to increased levels of the Th1 inflammatory cytokines tumor necrosis factor alpha (TNFa) and interferon gamma (IFNg). IL-10, an anti-inflammatory cytokine, was largely absent until day 6. Given that IL-10 is known to play a critical role in protecting the host from tissue damage,[325] its upregulation on day 6 further indicates a reigning in of the highly inflammatory immune response. This data reveals that cytokine detection *via* CyTOF intracellular staining can reveal the cytokine milieu of the infected lung with the added ability to tie functional marker expression back to individual cellular subsets.

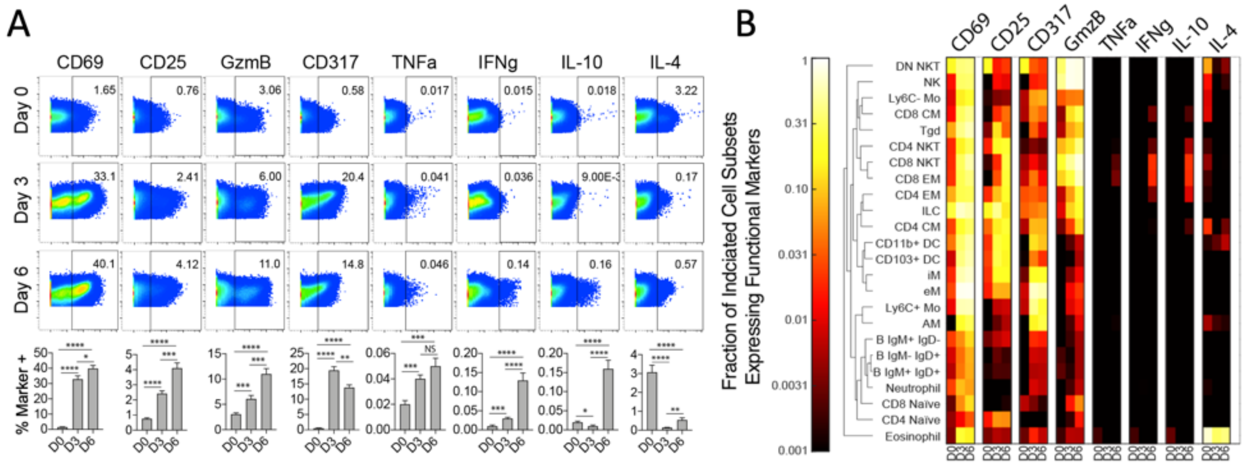

Figure 4.5. Analysis of functional marker expression
(**A**) Biaxial plots of functional marker expression *vs.* CD45. Bar charts summarize marker frequency out of total CD45+ cells on day 0 (D0), day 3 (D3), and day 6 (D6). (**G**) Clustergram analysis of marker expression frequency for each cell type on D0, D3, and D6. CD4 and CD8 EM and NKT populations have relatively high frequency of TNFa, IFNg, and IL-10 positive cells on D6. Data represent mean ± SEM, $n = 10$; statistical comparisons computed by one-way ANOVA followed by post hoc Tukey's pairwise comparisons, $*p < 0.05$, $**p < 0.01$, $***p < 0.001$, $****p < 0.0001$.

To this end, we next assessed the frequency of functional marker expression on individual cell types (**Figure 4.5B**). As expected, activation markers CD69 and CD25 were upregulated in most cell types upon infection. GzmB expression, while traditionally believed to be exclusive to NK and cytotoxic T cells, has recently been discovered in many immune and non-immune subsets, with newly identified roles in cellular signaling, chemotaxis, and cytokine release, among others.[326] Accordingly, we detected increases in GzmB expression in nearly all cellular subsets by day 6, with the highest frequencies occurring in T cell, NK, and NK T cell (NKT) populations. These cell types also had the highest frequencies of TNFa, IFNg, and IL-10 expression, further confirming the important roles of these effector cell types in orchestrating the antiviral immune response. Despite the clear Th1-type cytokine environment, high frequencies of eosinophils produced IL-4 throughout the course of infection. While the significance of this is unknown, this IL-4 production may help regulate the strong Th1-type response in conjunction with IL-10.[327]

Next, we examined the contribution of each cell type to total cytokine positive cells on days 3 and 6 (**Figure 4.6**). Monocytes, macrophages and neutrophils substantially contributed to overall TNFa, IFNg, and IL-10 cytokine production, despite their very low (<0.1%) cytokine positive frequencies (**Figure 4.6**). However, in agreement with the previous analysis, CD4 and CD8 EM T cells together are the major contributors of IL-10 (92%), IFNg (86%), and TNFa (44%) cytokine positive cells on day 6. These results reveal the marked contribution of effector T cells to overall cytokine production, demonstrating their capacity to greatly influence the immune response.

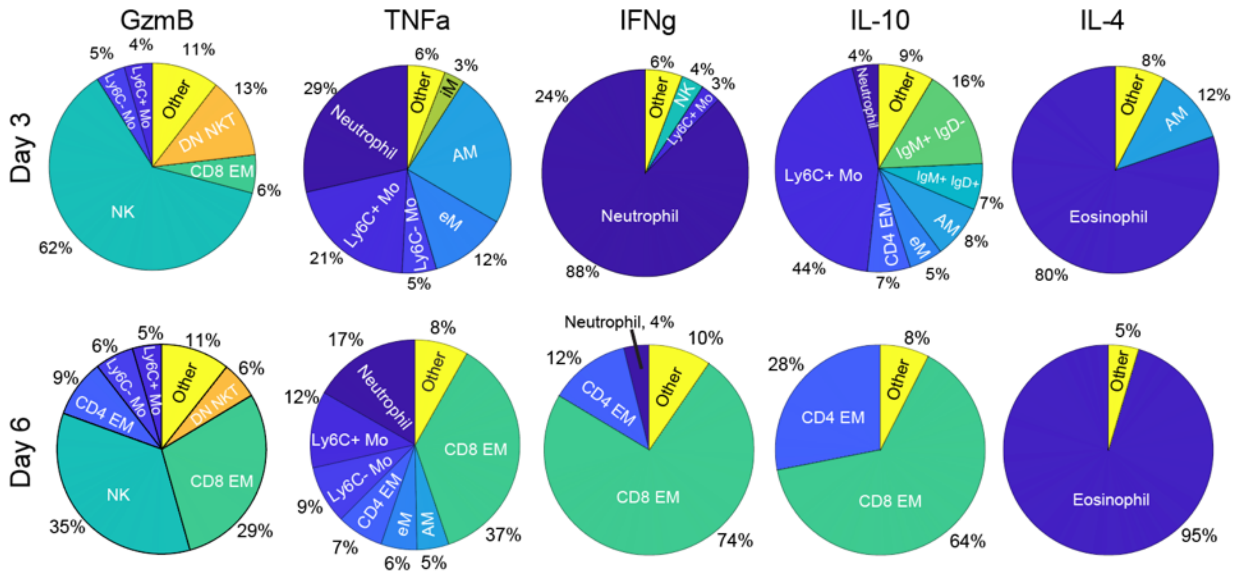

Figure 4.6. Contribution of each cell type to total cytokine production
Contribution of each cell type to total cytokine positive cells indicates substantial contribution of CD4 and CD8 EM T cells to total TNFa, IFNg, and IL-10 on day 6. Contributions < 3% are grouped into "other".

Given the considerable cytokine activity of CD4 and CD8 EM T cells (**Figure 4.5B and 4.6**), we further investigated the co-production of cytokines in these cellular subsets on day 6. While CD8 EM T cells demonstrated greater overall cytokine activity, both subsets demonstrate IFNg and TNFa single positive populations as well as IFNg and IL-10 double positive cells (**Figure 4.7**). Considering their significant activation (**Figure 4.5B**) and accumulation (**Figure 4.5C**) of these cell types, it is notable that relatively few of these effector cells are expressing cytokines during infection. This cytokine release profile is indicative of small bursts of cytokine from very few cells at a time, demonstrating the exceptionally tight regulation of these potent immune regulators. Furthermore, it is intriguing that IL-10, considered to be a master negative regulator of inflammation,[325] is co-expressed with IFNg, a proinflammatory cytokine[328] (**Figure 4.5B**).

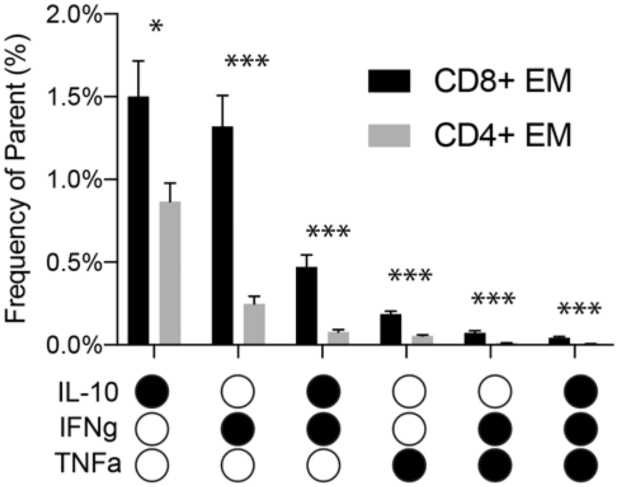

Figure 4.7. Cytokine co-production by CD4 and CD8 EM T cells
Co-production of cytokines by CD4 and CD8 EM T cells indicates significant fraction of cells co-expressing IL-10 and IFNg. Data represent mean ± SEM, $n = 10$; statistical comparisons computed by two-sided T test with FDR = 10%, $*p < 0.05$, $**p < 0.01$, $***p < 0.001$.

Overall, the aforementioned changes in cellular frequencies are indicative of a strong Th1 inflammatory immune response (neutrophil, eM, and Ly6C+ Mo) between day 0 and day 3 that wanes by day 6, giving rise to cells involved in tissue repair (Ly6C- Mo and iM) and the adaptive immune response (CD4 and CD8 EM T cells). Functional marker expression further supports this narrative, with innate immune cells producing nearly all cytokines on day 3 whereas adaptive CD4 and CD8 T cells takeover the majority of TNFa, IFNg, and IL-10 production by day 6 (**Figure 4.6**). Such results are largely in agreement with progression of influenza disease,[329] validating the CyTOF approach for comprehensive analysis of the immune landscape.

4.4.3. Susceptibility of Immune Subsets to Viral Infection and Replication

Epithelial cells lining the lung and airway are considered to be the primary source of influenza replication during infection, where it is estimated that a single infected cell can produce on the order of 10,000 progeny virions.[12] In addition, it is also recognized that immune cells can become infected.[330,331] Experiments utilizing GFP reporter viruses[331] and single cell RNA sequencing[330] were able to identify immune cells susceptible to influenza infection *in vivo*. However, identification of susceptible cell types in these experiments was limited to crude immune subsets (*e.g.,* bulk B cell, T cell, NK, and granulocyte populations). In addition, while these methods can identify infected cell types, they are not able to identify whether or not cells support viral replication. Aside from these studies, the relative susceptibility of immune cells to influenza viral infection and replication *in vivo* remains largely unexplored. Furthermore, it has not been reported whether cellular susceptibility to influenza virus infection changes with age.

To enable the identification and tracking of infected immune cells over the course of influenza infection, we included two antibodies in the CyTOF panel against the influenza hemagglutinin (HA) protein: one used for cell surface staining (HA^{S}) and the other used for intracellular staining (HA^{IC}). We hypothesized that HA^{IC} signal could result from either infection or phagocytosis of infected cells, whereas HA^{S} signal could only result from productive infection. Biaxial plots of HA^{S} *vs.* HA^{IC} support this premise, where very few cells are $HA^{S+}HA^{IC-}$ (Q1) compared to $HA^{S+}HA^{IC+}$ (Q2) (**Figure 4.8A**). Based on this data, we assumed Q2 cells to be infected and supporting viral replication at least up to the point of viral surface expression whereas Q3 cells were either (1) infected and not supporting viral replication or (2) had phagocytosed infected cells.

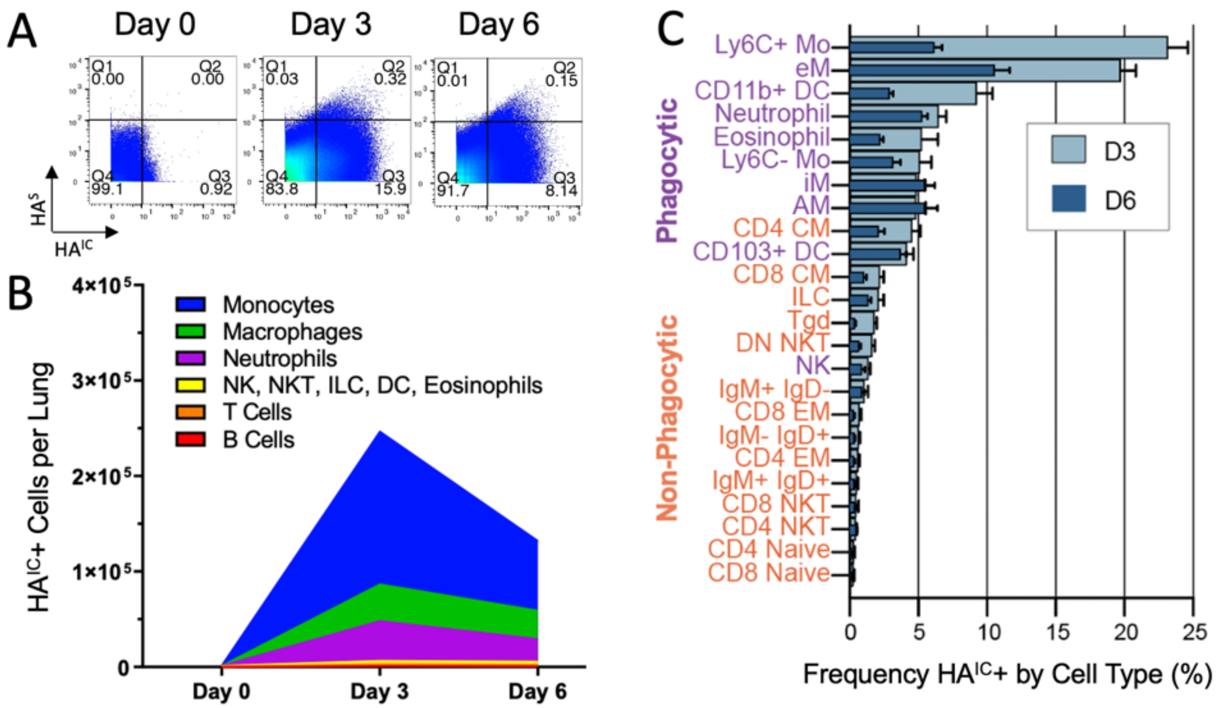

Figure 4.8. Influenza HA marker expression on immune subsets
(**A**) Biaxial plots of HA surface (HA^{S}) and intracellular (HA^{IC}) staining. Q2 cells are infected and permitting viral replication (at least up to the point of HA^{S} expression). Q3 cells are either (1) infected and not permitting viral replication or (2) have phagocytosed infected cells. (**B**) Total HA^{IC+} cells per lung by cell type. (**C**) Frequency HA^{IC+} cells by cell type sorted by day 3 frequency reveals nearly perfect division between phagocytic and non-phagocytic cell subsets.

The absolute number of HA^{IC+} immune cells was plotted over the three timepoints (**Figure 4.8B**). Total HA^{IC+} immune cells were found to peak on day 3 and diminished towards day 6, with neutrophils, monocytes, and macrophages comprising the vast majority (> 98%) of HA^{IC+} cells at both time points. Next, the percentage of HA^{IC+} cells within each cell subtype was analyzed on day 3 and day 6 (**Figure 4.8C**). A clear division in cellular subsets is observed, with phagocytic cells possessing the highest HA^{IC+} frequencies (~2% – 23%, purple labels) compared to non-phagocytic cells (0.03% – 5.0%, orange labels). While the relative contribution of phagocytosis and infection to HA^{IC} signal cannot be determined in phagocytic cells, HA^{IC} signal in non-phagocytic cells can only result from infection. Thus, the broad range of HA^{IC} frequency in non-phagocytic cells (0.03% - 5.0%) indicates that cells possess a range of infection susceptibility, with CM T cells, ILCs, and Tgd being the most susceptible and naïve T cells being the least. We considered that the large variation in HA^{IC+} frequency in both phagocytic and non-phagocytic cells (**Figure 4.8C**) might be related to cellular abundance in the lung, with more abundant cell types potentially having a higher probability of being infected or participating in phagocytosis. However, there is no positive correlation between relative cell abundance and HA^{IC+} frequency (**Appendix B.7**). Based on this data, we conclude that the variation in HA^{IC+} frequency must be a result of immune subsets having differential phagocytic capacity and/or susceptibility to infection.

To gain more insight into cellular susceptibility to viral infection and replication, we investigated the relationship between Q2 frequency and Q3 frequency for each cell type. We focused on day 3 due to the elevated HA frequency at this timepoint (**Figure 4.8B**). In non-phagocytic cells, Q2 frequency is highly correlated to Q3 frequency ($R^2 = 0.837$, **Figure 4.9A**), suggesting they share a similar susceptibility to viral replication. Indeed Q2/Q3 frequency is not significantly different in non-phagocytic cells (**Figure 4.9B**). The analysis of phagocytes is slightly more complicated due to Q2 signal having contributions from both infection and phagocytosis. Nevertheless, several observations can be made. The correlation between Q2 and Q3 is much weaker for phagocytic cells ($R^2 = 0.001$, **Figure 4.9C**). Specifically, neutrophils and CD11b+ DCs have relatively high Q2 frequency relative to Q3 frequency, especially in comparison to eM and Ly6C+ Mo (**Figure 4.9C**). Indeed, the ratio of Q2 over Q3 frequency for CD11b+ DCs and neutrophils is significantly higher than nearly every other phagocytic cell (**Figure 4.9D**). As increased phagocytic capacity would only be expected to lower the Q2/Q3 ratio (larger Q3), we conclude that the high Q2/Q3 ratio of CD11b+ DCs and neutrophils indicates an increased susceptibility to viral replication relative to other phagocytic cell types. Using similar reasoning, Ly6C+ Mo and eM are the most resistant cell types to viral replication.

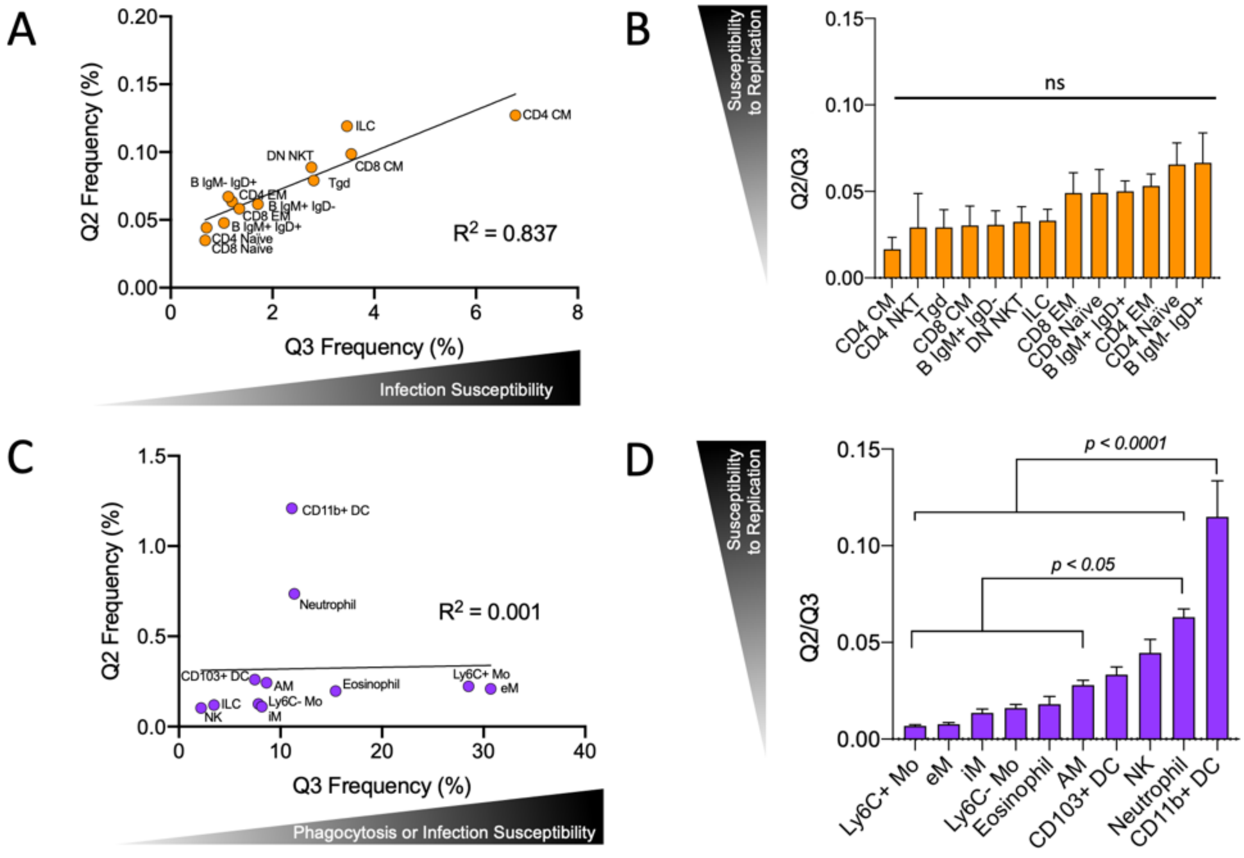

Figure 4.9. Susceptibility of cell types to infection and replication
(**A**) Q2 (HA^{S+}HA^{IC+}) *vs.* Q3 (HA^{S-}HA^{IC+}) frequencies for non-phagocytic cells. (**B**) Ratio of Q2 over Q3 for non-phagocytic cells indicates they all have similar susceptibility to infection. (**C**) Q2 *vs.* Q3 frequencies for phagocytic cells. (**D**) Ratio of Q2 over Q3 for phagocytic cells indicates neutrophils and CD11b+ DCs have higher susceptibility to viral replication compared to other phagocytic cells. Data represent mean ± SEM, $n = 10$; statistical comparisons computed by one-way ANOVA with post hoc Tukey's pairwise comparisons.

Finally, we investigated whether functional marker expression varied depending on whether cells occupied Q2, Q3, or Q4 (**Figure 4.10A**). Perhaps most noticeably, cells in Q3 generally had higher frequency of CD317 and CD69 than cells in Q2 or Q4. CD317 (*i.e.,* tetherin), is an IFN-inducible protein known to play a critical role in preventing the release of enveloped viruses from the cell surface.[332] The only cell types to possess high frequencies of CD317 in Q4 were Ly6C+ Mo and eM, perhaps explaining their exceptional resistance to viral infection (lowest Q2/Q3, **Figure 4.9D**). Furthermore, cell types with higher expression of CD317 and CD69 in any quadrant generally had a lower Q2/Q3 ratio. Indeed, Spearman correlation analysis revealed Q2/Q3 significantly correlated with frequency of CD317 and CD69 in Q2, Q3, or Q4 ($p < 0.05$) (**Figure 4.10B**). Thus, these results indicate that cellular activation and expression of IFN inducible proteins inhibits HA from reaching the cell surface, thwarting viral replication.

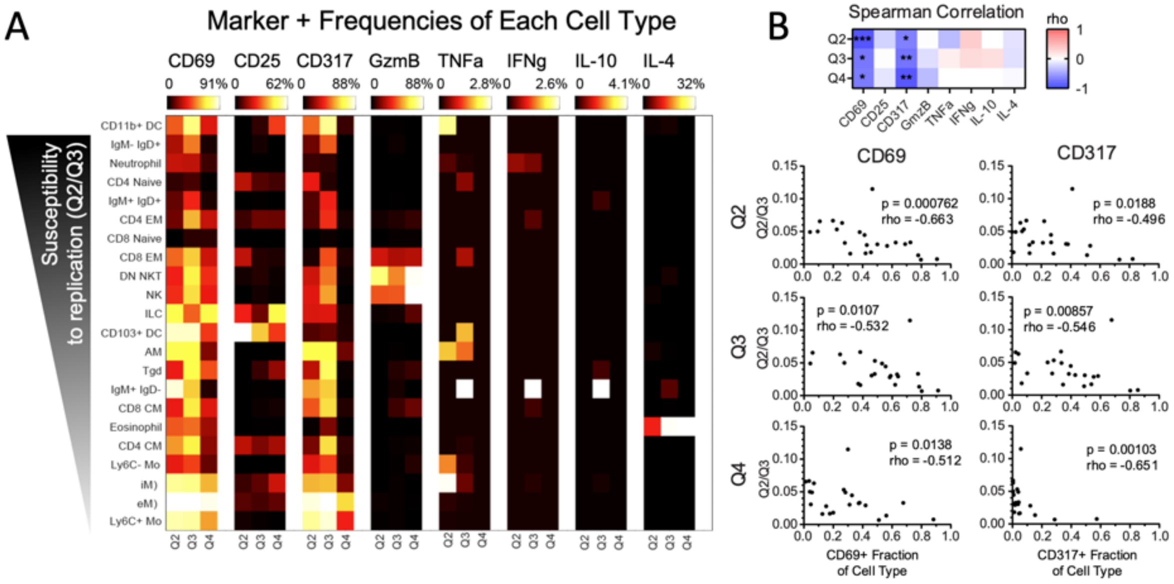

Figure 4.10. Functional marker comparison in uninfected, infected, and replicating cells
(**A**) The relative frequency of functional marker expression was compared for each cell type in Q2 ($HA^{S+}HA^{IC+}$), Q3 ($HA^{S-}HA^{IC+}$), and Q4 ($HA^{S-}HA^{IC-}$). Cells are sorted based on their susceptibility to viral replication (Q2/Q3, Figure 4.9B, D). The activation marker CD69 and IFN-inducible marker CD317 (tetherin) are generally highest in Q3, followed by Q2, then Q4. (**B**) Spearman correlation analysis between each cell type's susceptibility to viral replication (Q2/Q3) and marker expression for that cell type in Q2, Q3, or Q4. CD69 and CD317 expression in Q2, Q3, and Q4 are significantly correlated with susceptibility to replication. $^{*}p < 0.05$, $^{**}p < 0.01$, $^{***}p < 0.001$.

Overall this data reveals that performing both HA surface and intracellular staining can provide detailed information on infection and/or phagocytic behavior in individual cells. Immune subsets possess varying *in vivo* susceptibility to both viral infection (**Figure 4.9A, C**) and viral replication (**Figure 4.9B, D**). Furthermore, cells have clearly altered marker signatures depending on whether cells possess HA signal inside the cell or on the cell surface (**Figure 4.10**). Thus, in conjunction with previous results, CyTOF analysis successfully provides comprehensive information on the dynamic changes in cell populations, marker expression, and infection parameters that are necessary to deeply interrogate the immune response.

4.4.4. Aged Mice Display Altered Cellular Accumulation and Functional Marker Expression

After detailed characterization of the immune landscape in C57Y mice, we next compared the response to that of C57A mice. To understand basal level differences between the resting state of young (9 weeks) and aged (76 weeks) mice, we compared cell type frequencies between the two groups on day 0 (**Figure 4.11A**). Analysis revealed that 11 of the 24 cellular subsets undergo significant changes in frequency upon aging. The greatest variation resided in the T cell compartment, where C57A mice expectedly had significantly greater frequencies of CD4 and CD8 EM T cells while young mice had significantly greater naïve T cells. In addition, we identified greater AM frequencies in C57Y as has been previously reported.[333]

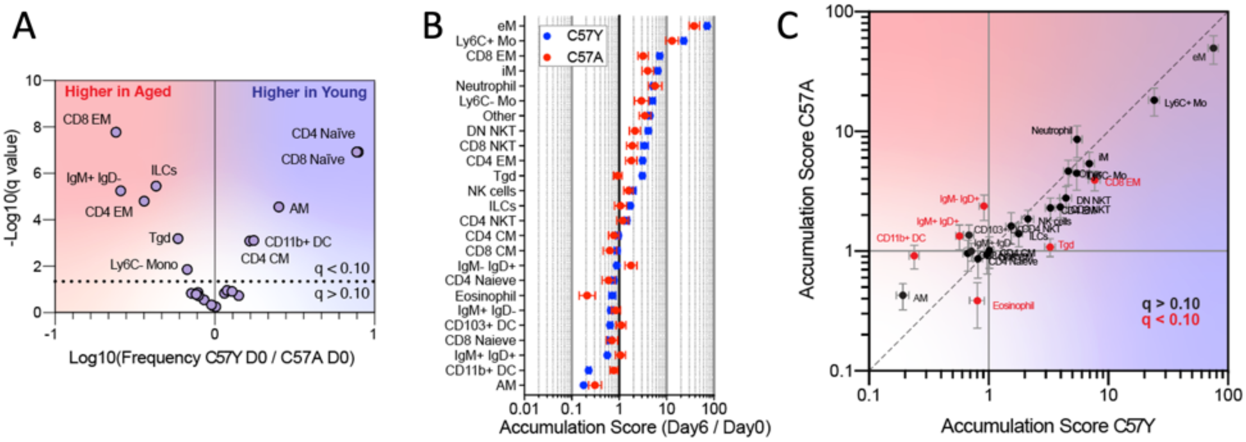

Figure 4.11. Aging results in reduced cellular accumulation
(**A**) Volcano plot indicates the fold change in cell type frequency between young (C57Y) and aged (C57A) mice on day 0. (**B**) Comparison of accumulation score of C57Y and C57A mice on day 6

indicates aging leads to reduced cellular infiltration in response to viral infection. Cell subtypes are sorted based on C57Y. Significance is indicated in (C). (**C**) Accumulation scores of C57A *vs.* C57Y cell types. Significantly different subsets are indicated in red. Significance computed by two-sided T test with FDR = 10%.

Following influenza viral infection, the fold change in cellular subsets between day 0 and day 6 (accumulation score) was compared between young and aged mice (**Figure 4.11B**). While overall trends are similar between the two groups, C57A generally displayed less responsiveness to influenza viral infection, with lesser increases in cellular subsets with positive accumulation scores and lesser decreases is cellular subsets displaying negative accumulation scores. To better visualize changes in cellular accumulation between the young and aged groups, the accumulation scores for young and aged mice were plotted against each other (**Figure 4.11C**) with significantly different subsets (FDR < 10%) highlighted in red. In particular, C57A mice had significantly lower accumulation of CD8 EM T cell populations, a critical cell type known to directly participate in the killing of virus-infected cells.[334] In addition, C57A mice saw significantly greater depletion of eosinophils on day 6 but less depletion CD11b+ DCs and B cell populations. Overall these results demonstrate that aging leads to altered enrichment of important cellular subsets through either altered trafficking to and from the lungs and/or defective cellular proliferation.

Next, we investigated changes in functional marker expression with aging. Consistent with reports of elevated basal level activation and inflammation associated with aging (*i.e.* "inflammaging"),[335] aged mice on day 0 had increased frequencies of CD69, CD25, TNFa, and IFNg expression in bulk CD45+ cells (**Figure 4.12A**). However, the low-level activation of the aging immune system on day 0 did not translate to enhanced activation during infection. Aged mice had no statistically significant difference in CD25, GzmB, TNFa, IFNg marker frequencies between day 0 and day 6, whereas significant changes were observed in these markers in young mice. To determine the affected cell types, we compared functional marker expression in individual cellular subsets by taking the ratio of functional marker frequency in aged mice and young mice for each cell type (**Figure 4.12B**). Note only significant changes (FDR < 0.10) are displayed in **Figure 4.12B**. Hierarchical clustergram analysis largely separated T cells and NKT cells from the other subsets due to substantial age-associated changes in marker expression in this group. In particular, CM, EM, and NK T cells displayed reduced levels of CD25 and GzmB along with significantly reduced IFNg and IL-10 expression compared to their young counterparts. To better visualize changes in these subtypes, their frequency of functional marker expression for is plotted in **Figure 4.12C**. Indeed, CM, EM, and NK T cells subsets display significantly lower frequencies of activation markers CD69 and CD25. Furthermore, aged CD8 EM and CD8 NKT subsets demonstrate severely reduced cytokine production in contrast to their young counterparts. Thus, aged T cells exhibit defects in both accumulation (**Figure 4.11C**) and function (**Figure 4.12B, C**) in their response to influenza viral infection.

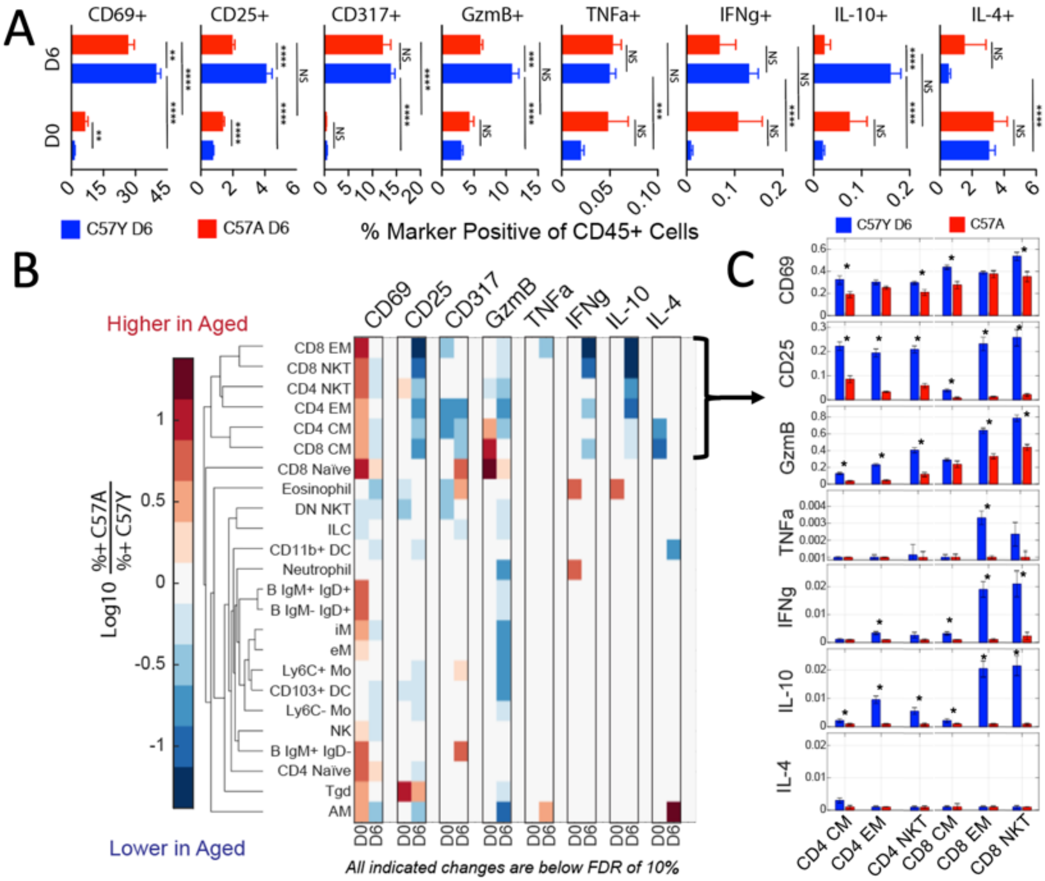

Figure 4.12. Aging affects functional marker expression
(**A**) Bar charts comparing C57Y and C57A marker frequency out of total CD45+ cells. (**B**) Log fold change of marker expression frequency for each cell type on day 0 and day 6. (**C**) NKT and T cell frequencies of functional marker expression on day 6. Data represent mean ± SEM. C57Y D0 *n* = 10, C57Y D6 *n* = 10, C57A D0 *n* = 10, C57A D6 *n* = 9. Statistical comparisons in (A) computed by one-way ANOVA followed by Tukey's pairwise comparisons or (C) two-sided T test with FDR = 10%, $*p < 0.05$, $**p < 0.01$, $***p < 0.001$.

Finally, we investigated HA expression on aged immune cells. Overall very little difference was observed between young and aged mice (**Appendix B.8**). No significant difference was observed in the fraction of CD45+ cells that were HA^{IC+} or HA^{S+} positive. Furthermore, no significant difference was observed in the ratio of Q2/Q3 compared to young mice for all cell types, indicating susceptibility to viral replication is largely unaffected by aging. Finally, any difference in marker expression in Q2 and Q3 were either not significant or the same as in **Figure**

4.12B, with few exceptions (**Appendix B.8**). These results indicate that infection kinetics and infection-induced marker expression are very similar for young and aged mice.

4.5. Further Discussion

The 40-marker panel and SVM classifier allowed over 90% of CD45+ cells to be classified into highly specific immune subsets, giving a global overview of the immune landscape during these critical early stages of influenza virus infection in the mouse lung. Our approach reveals in detail the early inflammatory response at day 3 followed by the initiation of the adaptive arm of the immune system by day 6. In addition to expected changes in cellular frequencies, we encountered unanticipated changes in cellular subsets not normally associated with viral infections. First, we observed a 4-fold increase in the frequency of Tgd over the course of infection (**Figure 4.4C**). Tgd occupy both innate and adaptive roles in the influenza immune response due to their diverse ability to be innately activated by influenza HA,[336] present influenza viral peptides to alpha beta T cells via MHC-II,[337] and kill virus-infected cells.[338] Confirming the important role of Tgd in the influenza immune response, the depletion of Tgd has been shown to result in reduced survival and increased lung injury in mice following H5N1 infection,[339] and higher Tgd cell counts in the lungs were responsible for improved protection against lethal H1N1 challenge observed in mice fed a high-fat ketogenic diet.[340] Second, we also identified dramatic shifts in eosinophil populations, which dropped nearly 10-fold on day 3 before subsequently rebounding on day 6 (**Figure 4.4C**). While eosinophils have been historically associated with the clearance of helminth infections and antagonists in allergic and asthmatic responses, there is accumulating evidence that eosinophils play a protective role in antiviral immunity. For example, mouse eosinophils become activated in the presence of influenza virus,[341] secrete RNases that decrease viral infectivity *in* *vitro,*[342] undergo piecemeal degranulation upon virus exposure,[341] and present influenza antigen *via* MHC-I and MHC-II that results in activation and proliferation of CD4 and CD8 T cells.[341,343] Furthermore, the transfer of lung eosinophils from allergen sensitized mice into influenza infected mice resulted in reduced viral burden, increased numbers of CD8 T cells, and improved survival.[341] The accumulation scores of eosinophils and Tgd was also significanlty lower in aged mice (**Figure 4.11C**). Therefore these cell types may possess uanpprecated roles in antiviral immunity.

In addition, our method enabled detection of rare cytokine positive cells without the need for *ex vivo* stimulation (**Figure 4.5A**), providing an accurate and quantitative picture of cytokine production resulting from *in vivo* cellular activation. These results revealed that cells producing IFNg, TNFa, and IL-10 *in vivo* are exceedingly rare (0.01-0.15% of immune cells, **Figure 4.7**), despite the drastic changes occurring in the immune environment (**Figure 4.5**). We also discovered populations of CD4 EM and CD8 EM T cells that co-produce the inflammatory cytokine IFNg as well as the anti-inflammatory cytokine IL-10. As approximately one fourth of IFNg expressing CD8 EM T cells also co-expressed IL-10 (**Figure 4.7**), co-production of these cytokines is not a rare event. Intriguingly, these results point towards regulation of inflammatory and anti-inflammatory responses on both the *inter*cellular level (IFNg and IL-10 single positive cells) and *intra*cellular level (IFNg and IL-10 double positive cells), revealing multiple mechanisms for the immune system to fine-tune the balance between antiviral activity and tissue damage.

The measurement of HA^S and HA^{IC} signal reveals that cell types have differential susceptibilities to viral infectivity and viral replication *in vivo*. In particular, we noted Ly6C+ Mo and eM were incredibly resistant to viral replication (lowest Q2/Q3) while neutrophils and CD11b+ DCs were the most susceptible. We believe that it is unlikely this difference in resistance can be attributed to differential exposure to influenza virus *in vivo* as these cell types are all highly phagocytic and therefore in direct contact with virus infected cells. Therefore, susceptibility to viral replication is likely an intrinsic cellular property. We were in fact able to correlate higher expression of CD317 and CD69 with improved resistance to viral replication, providing a mechanistic underpinning for the observed effects. However, it is unclear why these markers are not as upregulated in certain cell types. In addition, CD11b+ DCs were an exception to this trend, with high Q2/Q3 ratio but also high CD317 and CD69 expression. Although unknown, perhaps the high levels of activation and IFN-inducible proteins in DCs help to control and prolong viral replication in order to generate more antigen for presentation to T cells and B cells. We also noted that CD317 and CD69 were generally lower in cells undergoing active viral replication (Q2) compared to cells expressing only intracellular HA (Q3). This suggests that viral replication is only permitted in cells with low expression of these markers. Supporting this, mutant influenza viruses that are unable to suppress cellular IFN responses through knockout of viral protein NS1 have impaired viral replication.[344]

We next applied our approach to the study of how aging affects the influenza immune response. Overall, aged mice demonstrated a less sensitive response to viral infection, displaying lesser magnitude changes in cellular accumulation and depletion as well as reduced cellular activation (**Figure 4.11B and 4.12A, B**). Most notably, aged mice displayed severe defects in CD4 and CD8 EM, CM and NKT populations. In particular, CD8 EM T cells had ~2-fold lower accumulation ($p < 0.05$) compared to young mice by day 6 (**Figure 4.11C**) and had severely reduced (undetectable) expression of IFNg, TNFa, and IL-10 (**Figure 4.12C**). In fact, the overall frequency of cytokine positive immune cells in aged mice was largely unchanged (not significant) between day 0 and day 6 (**Figure 4.12A**). With all the observed cellular changes between young and aged mice, it was surprising that analysis of HA surface and intracellular expression yielded very few significant differences with aging. This suggests that the cellular mechanisms for detecting viral infection (*e.g.*, toll-like receptors) and upregulation of the IFN pathway remains largely intact with age. Indeed, our results showed that CD317 expression – indicative of the IFN response – was the least affected functional marker with aging (**Figure 4.12A**). Thus, it appears that the major defects with aging that lead to the reduced cellular infiltration and cytokine production are not due to deficiencies in the cellular IFN response.

4.6. Conclusions

It is essential to understand protective immune responses in order to design next-generation vaccines that attempt to elicit these protective responses. However, the complexity of the immune landscape makes it challenging to fully evaluate an immune response. In this work we investigate the ability of high-dimensional mass cytometry to fully characterize the early stages of the influenza immune response in young and aged mice. To efficiently classify cells in the large 40-dimensinal dataset, we developed a probabilistic SVM classifier that enabled automated supervised learning with minimal human intervention. Analysis of the resulting dataset reveals in detail the early inflammatory response at day 3 followed by the initiation of the adaptive arm of the immune system by day 6. Moreover, we were able to detect cytokine positive cells activated *in vivo*, revealing the substantial role effector T cells play in affecting the overall cytokine environment. We also demonstrate that simultaneous detection of intracellular and surface HA reveals that cell types have differential susceptibility to influenza infection and replication. We further show that the susceptibility of cells to viral replication is highly correlated to their expression of activation marker CD69 and IFN-inducible marker CD317.

These results reveal the incredible depth of immune interrogation provided by CyTOF that make it a highly useful tool for probing the immune response to viral infection or vaccination. In particular, the ability to detect single-cell cytokine expression data in combination with staining for the vaccine immunogen will be especially valuable for evaluating vaccine response. This information will answer questions about which cells are interacting with the vaccine immunogen and how they are responding in terms of functional marker and cytokine expression. It will be incredibly interesting to compare the responses elicited by vaccination and infection.

Furthermore, this study reveals the challenges associated with stimulating the aged immune system. In comparison to young mice, aged mice had reduced cellular infiltration – especially CD8 EM T cells – in response to influenza viral infection. Furthermore, effector T cells in aged mice displayed severe defects in IFNg, TNFa, and IL-10 production. Due to the critical roles of effector T cells and these cytokines, aged mice are deficient in key components of antiviral immunity. While it is well known that aging leads to reduced functionality in effector T cells, it is noteworthy that this analysis – which is the most comprehensive flow-based analysis of influenza immune response to date – identified T cell defects as the greatest deficiency in the aged immune response. As T cell immunity is highly important in many diseases, including influenza, deriving mechanisms of stimulating T cells will be essential for achieving enhanced efficacy in aged individuals.

4.7. Materials and Methods

4.7.1. Animal Handling, Infection, and Sample Collection

Mice were housed in an AAALAC-accredited facility, in compliance with the Public Health Service Policy on Humane Care and Use of Laboratory Animals and the *Guide for the Care and Use of Laboratory Animals*.[345] All procedures were approved by the IACUC at the University of Michigan.

Female C57BL/6 mice of 9 weeks and 78 weeks (C57BL/6) of age were obtained from the Jackson Laboratory. Mice were infected with influenza virus strain A/Puerto Rico/8/34 (H1N1) (ATCC VR-1469). Mice were anesthetized with isoflurane and instilled intranasally (i.n.) with 40 μl PBS containing 1.2 X 10^4 PFU of PR8 virus as determined by standard plaque assay in MDCK cells. Mock-infected mice (Day 0) were instilled intranasally with 40 μl PBS alone. Following infection, mice were monitored daily for changes in weight and mortality. Mice were euthanized at indicated timepoints (Day 0, 3 and 6) with an overdose of CO_2. To remove circulating cells in the vasculature the chest cavity was opened, and the lungs were perfused by cutting the left atrium with scissors and slowly injecting 20ml cold PBS into the right ventricle with a vacutainer needle (BD Biosciences, Franklin Lakes, NJ). Perfused lung tissues were harvested from PR8-infected mice at 0 (Mock), 3- and 6-days post infection and stored in PBS with Golgi block cocktail of monensin and brefeldin (BioLegend, San Diego, CA) solution on ice prior to processing into single cell suspensions.

To obtained single-cell suspension, lungs were perfused, harvested from mice, minced, and then digested with 1 mg/ml Collagenase D (Roche, Penzberg, Germany) and 1 mg/ml DNase I (Roche, Penzberg, Germany) in PBS with Golgi Block without calcium and magnesium for 45 min at 37°C. After digestion, lung tissue was disrupted into single-cell suspension and filtered through a 70 μm strainer (Fisher Scientific, Waltham, MA). Cell yields and viability were measured using Trypan blue staining and a hemocytometer. Live cells were isolated over Ficoll-Paque (Cytiva, formerly GE Healthcare Life Sciences, Marlborough, MA) centrifugation media spun at 800 RPM for 15 minutes at room temperature. The band of live cells near the top of the gradient was resuspended in PBS with Golgi block, pelleted, and resuspended into fresh PBS with Golgi block prior to mass cytometry staining.

4.7.2. Antibody Conjugation with Lanthanide Metal

The lanthanide metals were purchased from Fluidigm and conjugated to the antibodies using Maxpar antibody labeling kit (Fluidigm Corp., San Francisco, CA) following manufacturer's instructions. Briefly, 2.5 mM Maxpar polymer was preloaded with lanthanide metal at 37C for 1h, purified and buffer exchanged to conjugation buffer using a 3 kDa Nanosep concentrator (PALL Life Sciences). The antibody was partially reduced using TCEP at 37°C for 30 min, purified and buffer exchanged to conjugation buffer using 50 kDa concentrator (Amicon Ultra, Millipore). The lanthanide-loaded polymer was conjugated to partially reduced antibody following overnight incubation at room temperature. The unbound metal was removed from the metal-tagged antibody by washing with wash buffer in 50 kDa concentrator. The final concentration of metal-tagged antibody was determined by measuring the absorbance at 280 nm against the wash buffer.

4.7.3. Sample Staining and CyTOF Acquisition

Cell-ID Cisplatin-195Pt and Cell-ID Intercalator Iridium-191/193 (Fluidigm) were used to identify live cells. The cells were washed once with pre-warm serum-free media by pelleting at 300 x g for 5 min at room temperature and stained with 1.25 μM live/dead stain (Cell-ID Cisplatin-195Pt diluted in serum-free media from 500 mM stock) at room temperature for 5 min. Free cisplatin was quenched by washing the cells with serum-containing media. The cells were than washed with CyFACS buffer and incubated with TruStain FcX (anti-mouse CD16/32, BioLegend, San Diego, CA) for 10 min at room temperature to block the Fc receptors. For cells surface marker staining, the metal-tagged antibody cocktail was made in CyFACS buffer and added to the cells in the presence of TruStain FcX (BioLegend) and incubated on ice for 60 min. Following cell surface markers staining the cells were washed twice with CyFACS buffer and fixed with 1.6% formalin in CyPBS for 20 min at room temperature. The cells were than washed and stored overnight at 4C in CyFACS buffer.

Next day, the cells were pelleted at 800 x g for 5 min and permeabilized with bioscience permeabilization buffer for 30 min at room temperature. The cells were than stained with 50 μL of intracellular staining metal-tagged antibody cocktail (made in eBioscience permeabilization buffer) at room temperature for 60 min. Following intracellular staining the cells were washed once with permeabilization buffer, twice with CyFACS buffer, and then stained with 62.5 nM Cell-ID Intercalator Iridium-191/193 (diluted in 1.6% formalin in PBS from 500 μM stock) at room temperature for 40 min or left at 4°C until ready for acquisition on CyTOF.

The samples were acquired using CyTOF Helios system (Fluidigm Corp., San Francisco, CA). The system was maintained and tuned according to the manufacturer's instructions. In addition, internal vendor-set calibration was performed before acquiring samples. The fixed cells were washed twice with CyPBS and deionized distilled Milli-Q water (Millipore), and filtered through 40 μM cell strainer. Recommended concentration of EQ Four Element Calibration Beads (Fluidigm) were added to the samples before acquiring them on CyTOF. The samples were acquired on CyTOF at approximately 300-400 events/s. The EQ Four Element Calibration Beads were used to normalize data using a bead-based passport specific to the manufactured bead lot.

After acquisition, the instrument software applied a signal correction algorithm based on the calibration bead signal to correct for any temporal variation in detector sensitivity.

4.7.4.Data Analysis

Signal spillover correction was applied using measured metal impurities as described by Chrevrier *et al.*[317] Total events were gated on gaussian parameters, DNA intercalator, cisplatin, event length, and CD45 to obtain high quality CD45+ live singlets (**Appendix B.3**) using FlowJo software package (FlowJo, LLC, Ashland, OR) . In total, 29 million events across the 80 samples were obtained for data analysis. 350,000 events were then equally sampled from the 80 mice (4,375 events per mouse) and subjected to manual gating into 24 cellular subsets (**Appendix B.3**). This subset of cleaned and gated cells was used for SVM classifier training. Classifier training is described in **Appendix B.9**. Following confirmation of the high correlation of SVM classification and manual gating (**Figure 4.2**), SVM classification was the applied to the entire 29 million cell dataset. 7% of cells were below the posterior probability threshold of 0.995 and were removed from the analysis, resulting in 27 million cells across all samples.

Chapter 5. Future Directions

In this work we established *S. cerevisiae* as a new recombinant host for influenza VLP production that has the potential for rapid manufacture of influenza vaccines. Furthermore, we developed the yICS tool that enables quantitative detection of yeast intracellular proteins in single cells and showed its utility for detailed strain characterization as well as high-throughput screening. In combination with the yeast influenza VLP system, these approaches will enable rapid prototyping of influenza VLP vaccines. Finally, to lay the groundwork for testing these vaccines, we validated mass cytometry for deep immune profiling of the mouse lung in response to influenza virus infection. These projects combine to form an accelerated platform for designing, building, and testing yeast-derived influenza VLP vaccines with the goal of enhancing influenza vaccine immunogenicity, improving heterosubtypic protection, and shortening manufacturing timelines. Here, we will discuss the future directions of these projects.

5.1. Engineering Yeast Influenza VLP and Enhancing Yield

In **Chapter 2**, we engineered *S. cerevisiae* to enable the production of functional influenza VLP. This is only the second instance that enveloped VLP production has been demonstrated in *S. cerevisiae*.[217] Despite the significance, the yield of high quality VLP after IMAC purification (~ 300 ng/L of HA) requires further improvement in order to establish yeast as a viable host for industrial influenza VLP production. Notably, the cellular yield of intracellular HA after multicopy integration (~3 mg/L) approaches that of Sf9 (~10 – 20 mg/L). Therefore, relieving further bottlenecks in yeast VLP formation has great potential to increase overall VLP yields to levels that are industrially relevant.

Elucidating the mechanism(s) of influenza VLP formation in yeast will give critical insight into potential strategies to improve VLP budding efficiency. Although we provide evidence that M1 interacts with HA in yeast (**Supplemental A.5**), further experiments are needed to determine if M1 plays a significant role in VLP formation. If so, the inclusion of other influenza viral proteins may improve influenza budding efficiency, as has been shown for production of influenza VLP in mammalian cells.[189]

In addition, the ability of HA to concentrate in lipid raft domains on the plasma membrane is considered critical for efficient budding of influenza VLP and virus. Engineering HA localization into yeast lipid rafts, if deficient, may further improve VLP yield. It is thought that lipid raft association of HA is enabled by two mechanisms: palmitoylation and cholesterol association. HA possesses a cholesterol recognition motif (CRAC domain) in its transmembrane domain that directly interacts with the cholesterol in lipid rafts.[346] However, yeast do not synthesize cholesterol, instead producing ergosterol. While the chemical structures of ergosterol and cholesterol only slightly differ, there is evidence that CRAC domains do not interact with ergosterol.[347,348] Both chemical[349] and genetic engineering methods[350] exist for introducing cholesterol into yeast and such approaches may increase influenza budding efficiency. The second complimentary mechanism of HA raft association is the post-translational functionalization of the HA cytoplasmic tail with palmitic acid residues that have affinity for the sterol-rich lipid rafts.[346] Yeast do perform palmitoylation, however their palmitoylation behavior can vary from mammalian cells. For example, vesicular stomatitis virus (VSV) glycoprotein is palmitoylated when expressed in mammalian cells but not in yeast cells.[351] Therefore, palmitoylation may represent another bottleneck in influenza VLP production.

While the aforementioned methods of increasing VLP yield rely on supporting the intrinsic self-assembly mechanisms of influenza virus, implementing and optimizing such approaches may be challenging due to the evolutionary distance between yeast and mammalian cell systems. Therefore, a more straightforward strategy for enhancing VLP yield may be to purify HA directly from yeast cell lysates and to incorporate HA into lipid nanoparticles *in vitro*. The construction of these so called "virosomes" from detergent-solubilized influenza virus is well documented.[352-355] In such a scheme, yeast cell lysates containing his-tagged HA could be detergent solubilized and purified by IMAC. Then, the detergent could be removed in the presence of lipids through either dilution or with detergent-absorbing beads (*i.e.*, Bio-Beads SM-2) to form nanoscale lipid vesicles containing HA (VLP). Such an approach has numerous advantages for industrial production. First, cell wall removal is not necessary, lowering the costs and complexity of the VLP procedure. Second, the resulting VLP contain highly purified HA with minimal contaminating yeast proteins. Finally, the resulting VLP are highly tunable. For example, immunostimulatory molecules (see **Section 1.4.1**) or HA proteins from multiple influenza subtypes can be easily mixed and matched during the detergent removal process to form customized VLP concoctions with enhanced properties.

5.2.Increasing yICS Throughput

In **Chapter 3**, we developed and validated an approach for antibody-based flow cytometric detection of intracellular yeast proteins. This method has several advantages over Western blot including higher throughput, simultaneous detection of multiple proteins, and single cell resolution that make it useful for both strain characterization and screening. While such a method is an important step forward, the yICS procedure is currently limited to multi-well plate format. However, it would be highly desirable to make yICS compatible with fluorescence activated cell sorting (FACS), which would increase throughput by orders of magnitude. To enable FACS compatibility, antibody labeling approaches must be developed that do not require cell wall removal because the resulting spheroplasts cannot be regenerated following FACS sorting. While conventional antibodies cannot penetrate the cell wall due to their large size (150 kDa),[47] camelid antibodies are much smaller (15 kDa),[356,357] and it has been demonstrated that these camelid "nanobodies" conjugated to fluorescent dyes can penetrate the intact yeast cell wall.[358] Thus, a nanobody-based yICS approach (yNICS) may be feasible.

yNICS would further improve on the yICS technique. First, without the need for cell wall removal, it would not be necessary for cells to be in the exponential growth phase, and the length of the procedure would be significantly cut down to only a few hours. More importantly, the compatibility of yNICS with FACS opens the door to numerous opportunities. For example, yNICS combined with FACS could identify and sort high expressing clones in a single tube directly following multicopy integration, precluding the need for plating cells, picking colonies, and growing up the clones separately. The greatly increased throughput would allow yNICS to take advantage of a key benefit of yeast: the ability to easily generate vast mutational libraries for screening of desirable phenotypes. For example, cellular mutations could be discovered that lead to enhanced HA expression level. Or perhaps screening libraries of mutated HA proteins could identify mutants that lead to enhanced plasma membrane targeting. yNICS opens up numerous possibilities that make such an approach worth exploring.

5.3. CyTOF Evaluation of Vaccines

In **Chapter 4** we demonstrated the ability of CyTOF to systematically characterize the immune response to influenza virus during the early stages of influenza infection in young and aged mice. Notably, our work extended the capabilities of CyTOF by demonstrating (1) the detection of cytokine production in single cells activated *in vivo* and (2) the identification of influenza infected and replicating cells by co-staining for HA inside the cell and on the cell surface. These innovative approaches will prove useful in the next stage of this project: studying the immune response to vaccination. Following immunization, intracellular HA staining will identify cells that have taken up VLP through either receptor mediated endocytosis or through phagocytosis. This information can then be combined with upregulation of activation markers or cytokine production in these cells to assess vaccine immunogenicity.

In addition, it will be enlightening to investigate how incorporation of TLR-stimulating molecules into VLP affects the immune response. It is understood that the type of TLRs stimulated and the magnitude of that stimulation can heavily influence the nature of cellular proliferation, cytokine production, and the formation of immunological memory.[359,360] Furthermore, TLR-stimulating adjuvants have been shown to increase antibody secreting cells (ASCs), the progenitors of long-lived bone-marrow plasma cells (BMPCs) that lead to long term immunity.[361,362] As it has been recently discovered that BMPCs wane appreciably within one year of influenza vaccination,[361] stimulating BMPC generation through TLR adjuvants may provide the key to increasing the duration of influenza vaccine protection. Therefore, tuning of TLRs on VLP may provide a mechanism of conferring long lived vaccine memory that can be directly investigated using CyTOF.

Aside from evaluating influenza vaccines, we have also demonstrated the value of CyTOF as a powerful investigational tool. CyTOF readily identified the defective effector T cell response in aged mice – a known attribute of immunosenescence[363] – validating its characterization abilities. While aging is perhaps the most well-recognized risk factor for influenza, it is becoming increasingly clear that other host factors such as co-morbidities, nutrition, microbiota, and genetics heavily influence the immune system and their effects are much less understood.[364] In particular, genetic variation is well recognized to play an important role in the susceptibility of both humans and mice to a variety of diseases[365-368] including influenza.[369,370] Thus, application of CyTOF to study the effects of these host factors may provide new insight into developing vaccines that can provide comprehensive and long-lasting protection for all demographics.

5.4. Final Thoughts

We have come a long way since the times when we believed that the heavens influenced disease outbreaks. The discovery of microorganisms has led to the development of antibiotics and vaccines which have arguably had a more positive impact on human life than any other invention in the history of mankind. In the past century we have come to better understand the immune system and how to safely harness the adaptive arm of the immune response to achieve immunological memory against pathogen threats. Given that the immune system has evolved over millennia to detect and respond to invading pathogens, early vaccine design focused on mimicking these microorganisms as much as possible in order to elicit stronger immune responses and better protection. This early dogma spawned the creation of inactivated vaccines and live attenuated vaccines that have been successful for many pathogens. However, several diseases such as influenza, HIV, and malaria have been resistant to this strategy. Therefore, a new paradigm has emerged. Simple biomimicry is insufficient, and further engineering of the vaccine immunogen is needed to obtain broad, long-lasting protection.

Next generation vaccines need to be rationally engineered to elicit potent and highly focused immune responses towards key pathogen epitopes. The pace of progress is rapid. For example, the existence of influenza broadly neutralizing antibodies in humans was only discovered in 2008, yet several vaccine candidates have already demonstrated the ability to elicit them. Despite this progress, vaccine design has primarily relied on trial and error approaches with large failure rates. This is largely a result of the lack of tools available to adequately study the incredible complexity of the immune system. Only recently have we developed the capability to probe immune responses with enough depth and breadth to elucidate protective immune mechanisms. Understanding these protective immune signatures will lead to a more predictive approach to vaccine design.

In order to develop these valuable models that can prospectively determine vaccine efficacy, advanced machine learning tools must be fed information on how vaccine features such as adjuvants, epitope locations, and protein surface densities affect vaccine immunogenicity and reactogenicity. However, obtaining the data to train these algorithms is a major bottleneck. Therefore, rapid platforms for designing, building, and testing vaccines must be established. In this dissertation, we engineered *S. cerevisiae* for the production of influenza VLP, establishing a high-throughput system for vaccine manufacture. In parallel, we developed a new tool to aid in characterization and screening of these yeast VLP strains. Finally, we demonstrated the utility of CyTOF for performing in-depth characterization of the influenza immune response and developed algorithms to automate analysis of large high-dimensional data sets. This work establishes a much-needed platform for rapid prototyping and evaluation of influenza vaccines.

Appendices

Appendix A: Supplemental Material for Chapter 2

Figure A.1. Western blot quantification standard curves for Figure 2.1

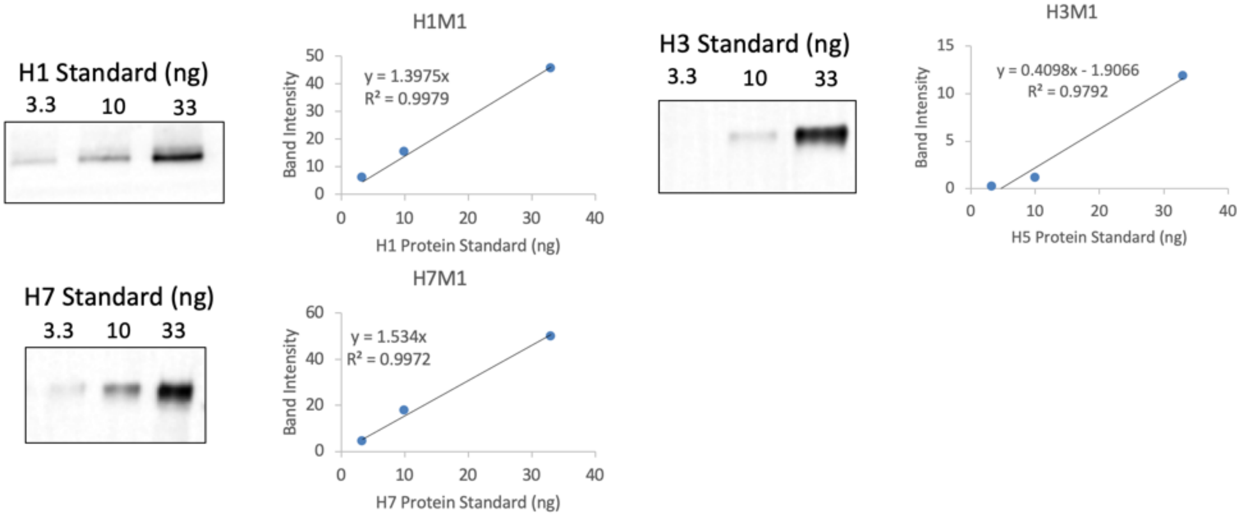

Figure A.2. Trimerization of yeast H1

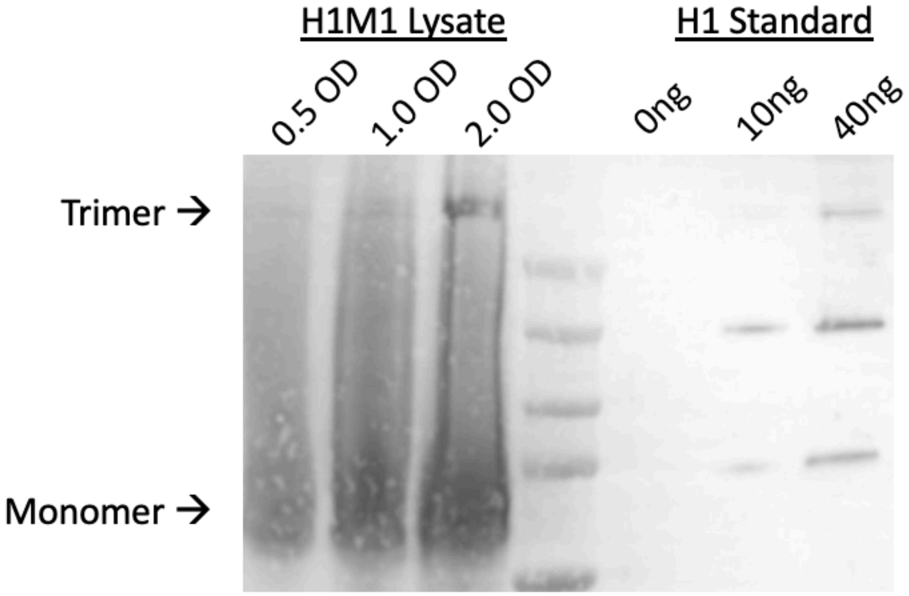

Western blot of yeast cell lysates of cells expressing H1M1 in comparison to H1 standard developed with anti-H1 antibody. 1 OD = 25 million cells.

Figure A.3. Western blot quantification standard curves for Figure 2.2 and 2.3

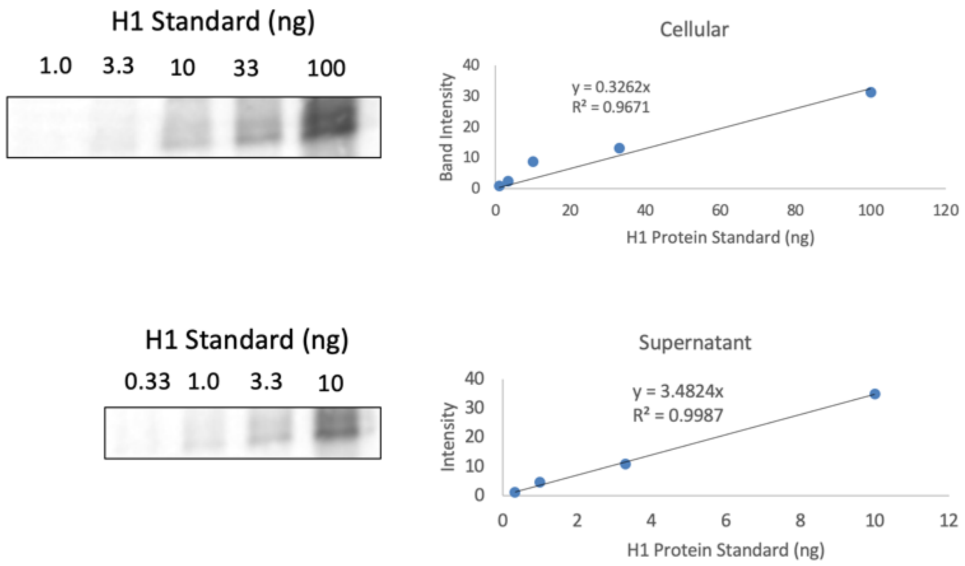

Figure A.4. Western blot quantification standard curves for Figure 2.4

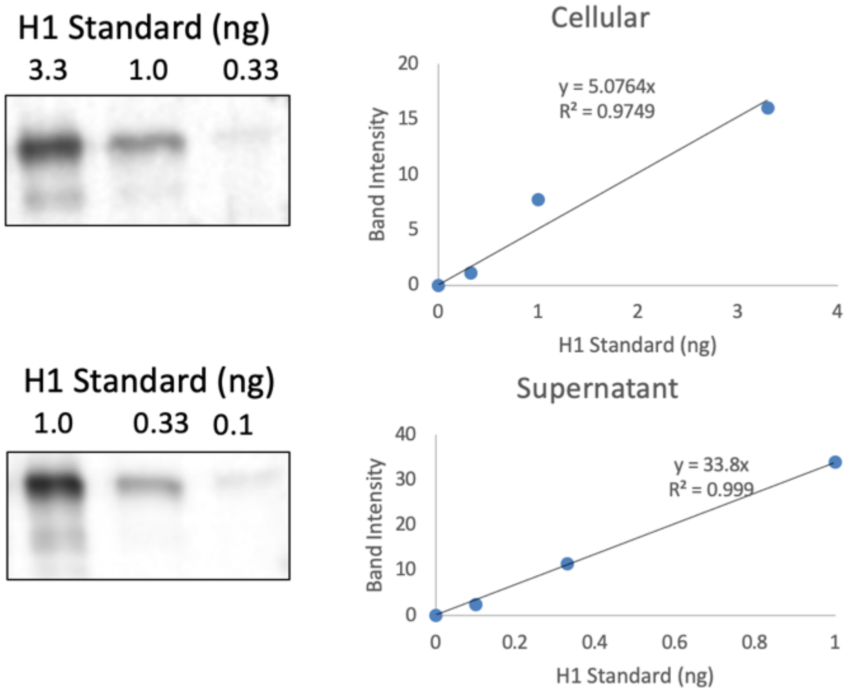

Figure A.5. Comparison of FC and his-tagged FC constructs

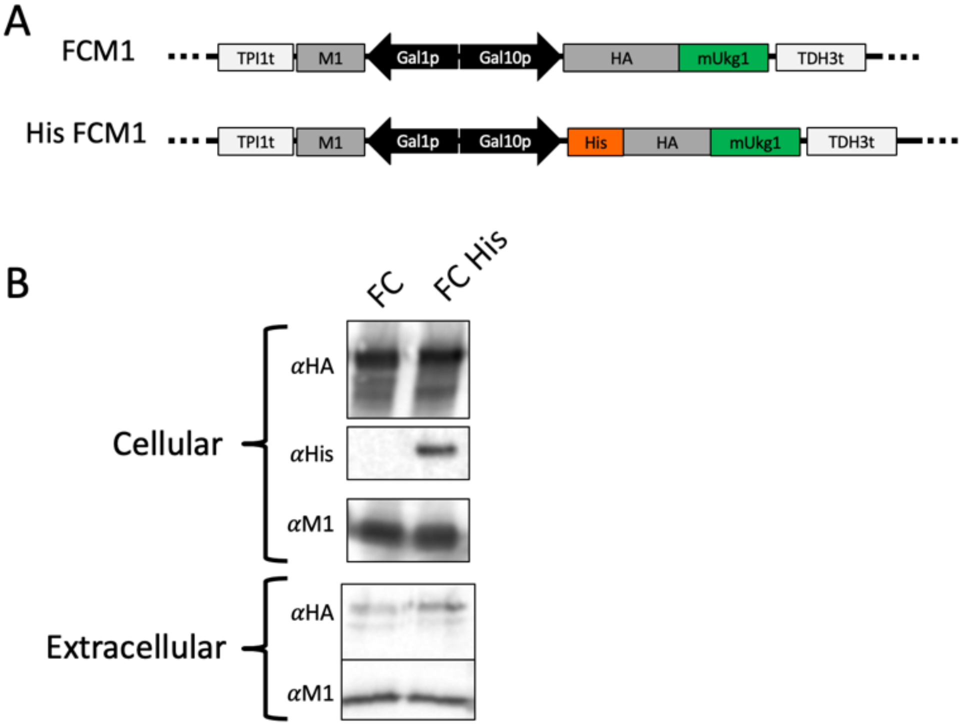

(**A**) 10x His tag was placed on the N-terminus of the FC construct right after the signal sequence. (**B**) Western blot analysis of FC and His-tagged FC constructs were indistinguishable from each other except for the ability of FC His to be stained with an anti-6xHis antibody.

Figure A.6. IMAC quantification of HA

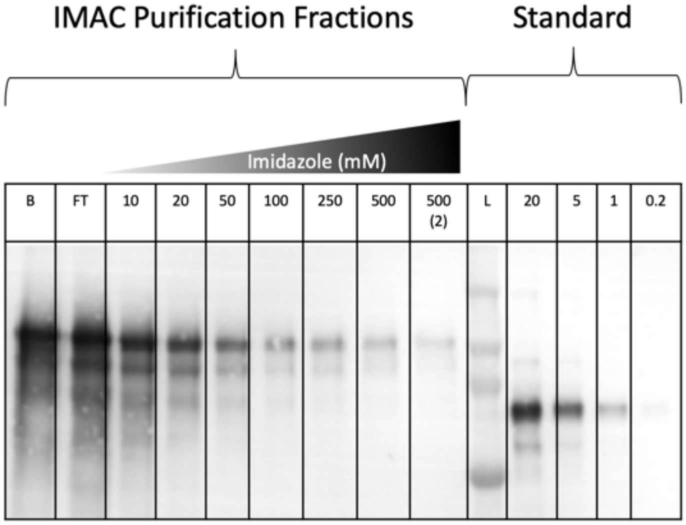

Quantification Data

Fraction	Total HA (μg/L)
Before IMAC	21
100 mM	0.12
250 mM	0.12
500 mM	0.06

Quantification of HisFC in different elution fractions during IMAC purification.

Figure A.7. Immunoprecipitation of HA pulls down M1

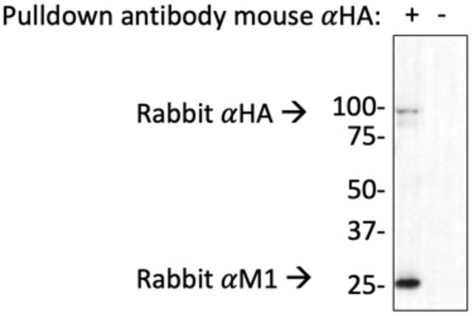

Immunoprecipitation of detergent solubilized FCM1 VLP with anti-HA antibody pulls down M1, indicating colocalization of the two proteins. FCM1 supernatants were diluted 1:1 with 100 mM C12E8 detergent for 10 minutes at room temperature. Immunoprecipitation was performed with a mouse anti-HA antibody 1:200 dilution at 4°C for 1 hr. Protein G magnetic beads (New England Biolabs, Ipswich, MA) were added and incubated for 1 hr 4°C. After washing 3x with PBS, samples were resuspended in SDS Page buffer. Samples were analyzed by Western Blot using rabbit anti-HA and anti-M1 antibodies followed be goat anti-rabbit alkaline phosphatase secondary antibody.

Appendix B: Supplemental Material for Chapter 4

Figure B.1. Aged mice have decreased survival compared to young mice

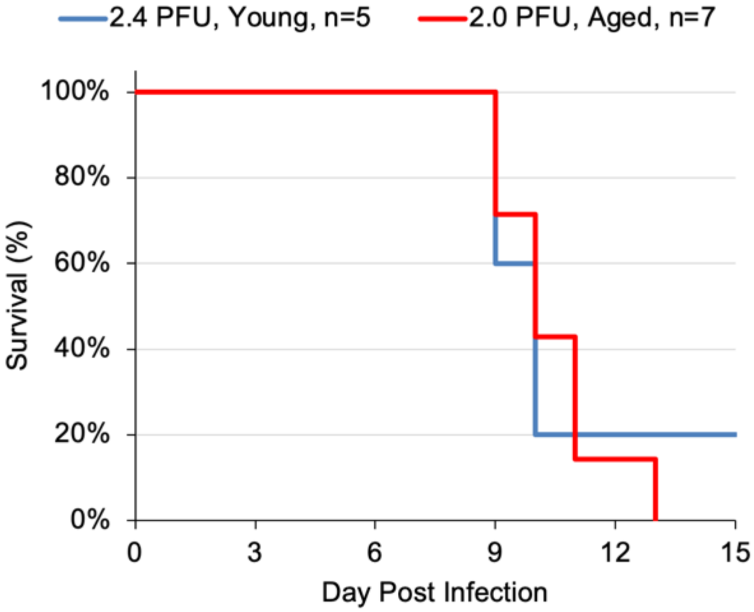

Young (9 weeks) and aged (76 weeks) C57BL/6 mice were intranasally infected with H1N1 A/PR/8/34 virus. Young mice were infected 2.4 × 10^4 plaque forming units (PFU) of virus whereas aged were infected with 2.0 × 10^4 PFU of virus. Despite being infected with a higher dose, young mice displayed enhanced survival.

Figure B.2. CyTOF antibody panel

	Label	Target	Clone	Company	Cat No
1	112Cd	CD19	6D5	Life Technologies	Q10379
2	141Pr	IFNg	XMG1.2	Biolegend	505812
3	142Nd	TNFalpha	MP6-XT22	Biolegend	506302
4	143Nd	anti-NP	H16-L10-4R5 (HB65)	BioXcell	BE0159
5	144Nd	Siglec-F	E50-2440	BD Biosciences	552125
6	145Nd	CD4	RM4-5	Biolegend	100520
7	146Nd	CD45R (B220)	RA3-6B2	Biolegend	103202
8	147Sm	CD206	C068C2	Biolegend	141701
9	148Nd	CD103	2E7	Biolegend	121402
10	149Sm	CD8	53-6.7	Biolegend	100716
11	150Nd	PDCA-1 (CD317)	129C1	Biolegend	127102
12	151Eu	CD49b	DX5	Biolegend	108902
13	152Sm	Ly-6C	HK1.4	Novus	NBP1-28046
14	153Eu	HA-IC	2F1A7	Sino Biologics	11684-MM03
15	154Sm	CD11c	N418	Biolegend	117302
16	155Gd	I-A/I-E	M5/114.15.2	Biolegend	107602
17	156Gd	CD25	3C7	Biolegend	101902
18	158Gd	IgM	RMM-1	Biolegend	406527
19	159Tb	Ly-6G	1A8	Biolegend	127637
20	160Gd	IL-4	11B11	Biolegend	504102
21	161Dy	HA	2F1A7	Sino Biologics	11684-MM03
22	162Dy	TCR γ/δ	GL3	Biolegend	118101
23	163Dy	CD64	X54-5/7.1	Biolegend	139302
24	164Dy	IL-10	JES5-16E3	Biolegend	505002
25	165Ho	CD49d	9C10 (MFR4.B)	Biolegend	103708
26	166Er	CXCR5	614641	Novus Biologicals	MAB6198
27	167Er	CD127	A7R34	Biolegend	135002
28	168Er	CD24	M1/69	Biolegend	101829
29	169Tm	Ki67	16A8	Biolegend	652402
30	170Er	CD62L	MEL-14	Biolegend	104402
31	171Yb	CD44	IM7	Biolegend	103014
32	172Yb	CD11b	M1/70	Fluidigm	3172012B
33	173Yb	CD69	H1.2F3	Biolegend	104502
34	174Yb	IgD	11-26c.2a	Biolegend	405702
35	175Lu	KLRG1	2F1	Novus Biologicals	MAB69441-100
36	176Yb	Granzyme B	GB11	Abcam	ab10912
37	191/193Ir	DNA		Fluidigm	201192B
38	195Pt	Live/Dead		Fluidigm	201064
39	209Bi	CD3	145-2C11	Biolegend	100314
40	89Y	mCD45	30-F11	Fluidigm	3089005B

Figure B.3. Gating scheme

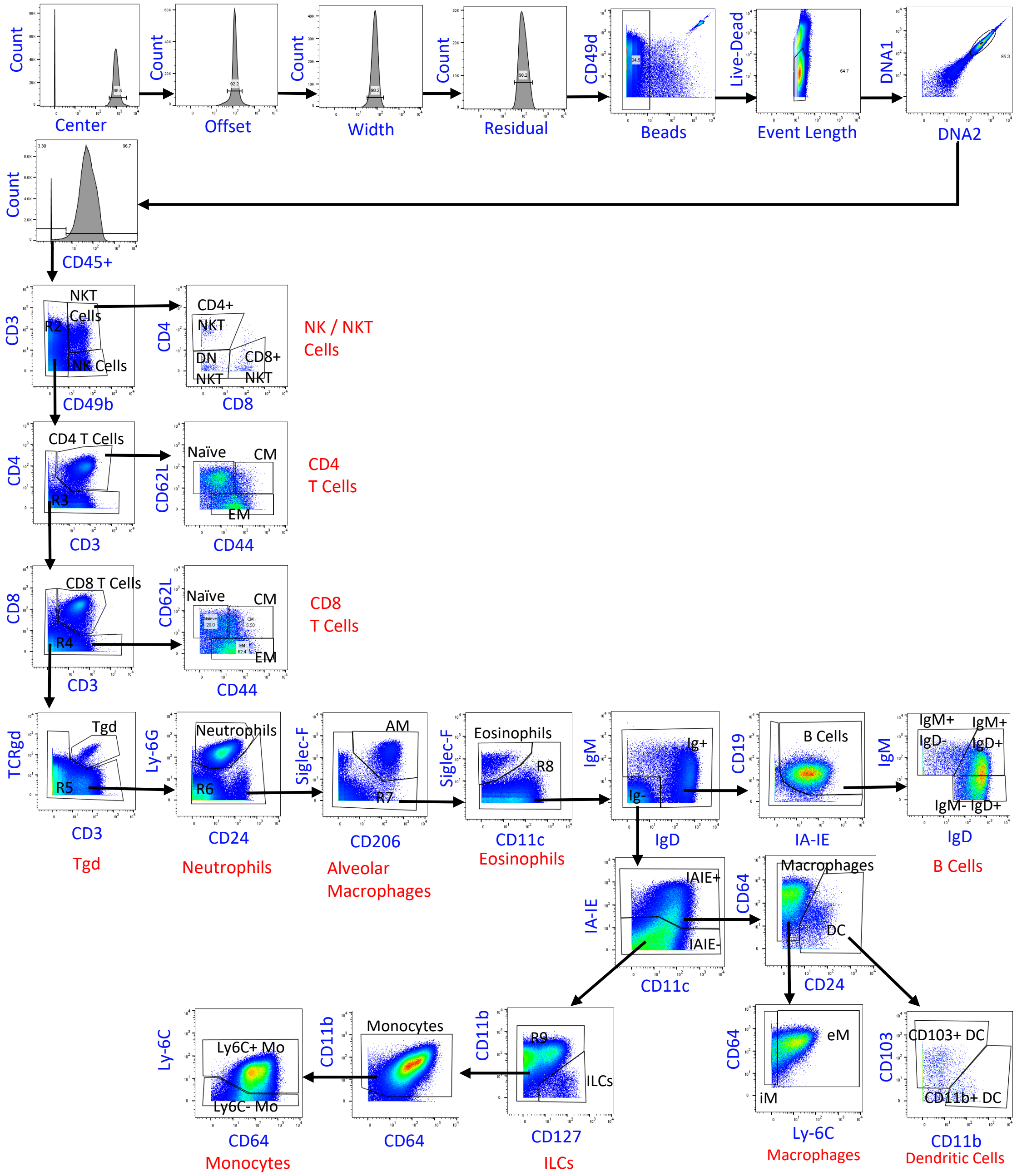

Figure B.4. SVM classifier probability threshold

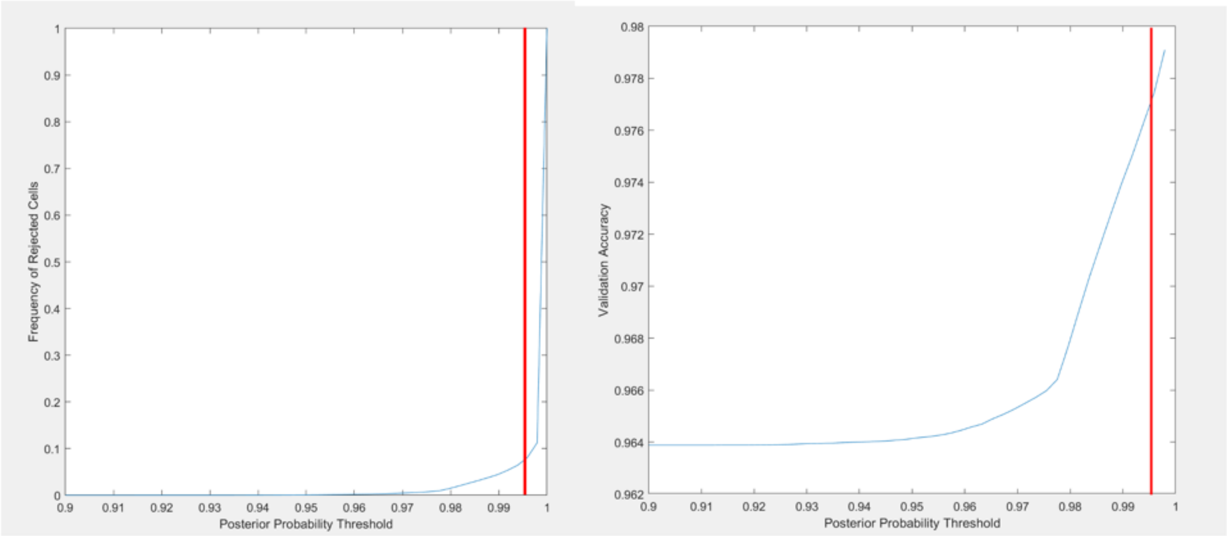

Effect of posterior probability threshold on proportion of rejected cells (left) and validation accuracy (right). Red bar indicates the chosen posterior probability threshold of 0.995.

Figure B.5. Comparison of SVM classification and manual gating

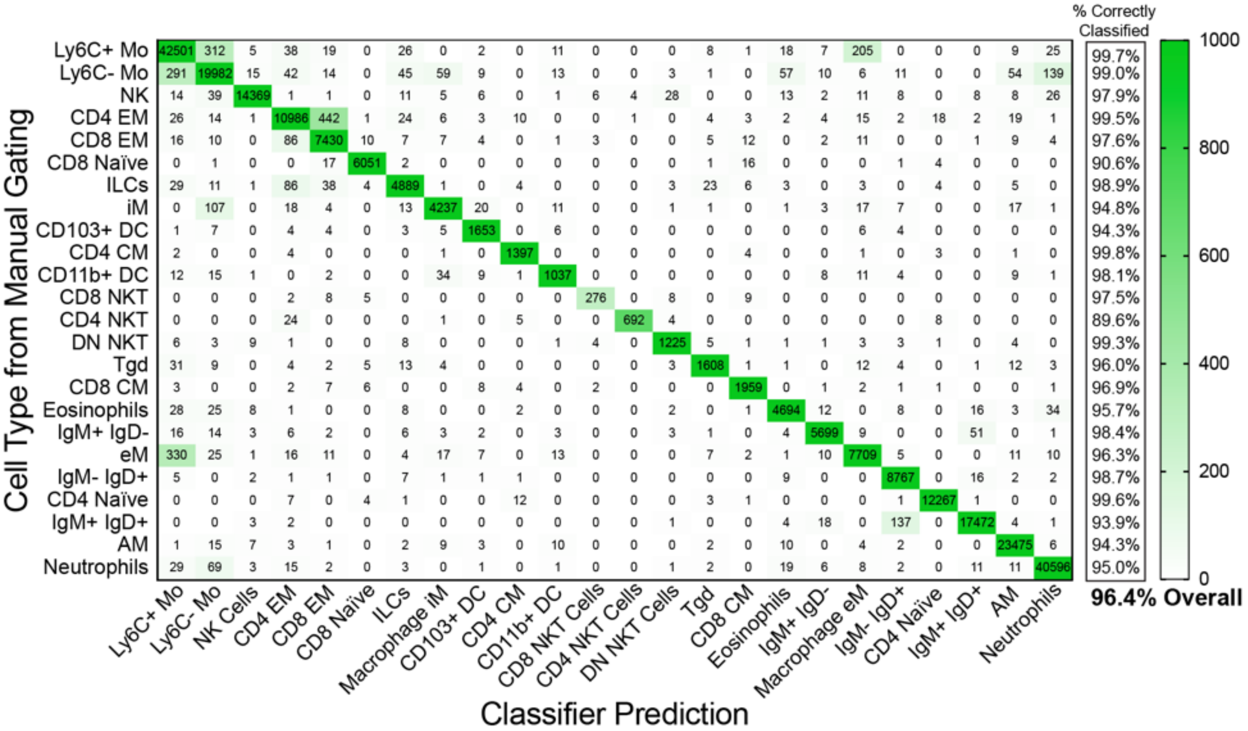

	Ly6C+ Mo	Ly6C- Mo	NK Cells	CD4 EM	CD8 EM	CD8 Naïve	ILCs	Macrophage iM	CD103+ DC	CD4 CM	CD11b+ DC	CD8 NKT Cells	CD4 NKT Cells	DN NKT Cells	Tgd	CD8 CM	Eosinophils	IgM+ IgD-	Macrophage eM	IgM- IgD+	CD4 Naïve	IgM+ IgD+	AM	Neutrophils	% Correctly Classified
Ly6C+ Mo	42501	312	5	38	19	0	26	0	2	0	11	0	0	0	8	1	18	7	205	0	0	0	9	25	99.7%
Ly6C- Mo	291	19982	15	42	14	0	45	59	9	0	13	0	0	3	1	0	57	10	6	11	0	0	54	139	99.0%
NK	14	39	14369	1	1	0	11	5	6	0	1	6	4	28	0	0	13	2	11	8	0	8	8	26	97.9%
CD4 EM	26	14	1	10986	442	1	24	6	3	10	0	0	1	0	4	3	2	4	15	2	18	2	19	1	99.5%
CD8 EM	16	10	0	86	7430	10	7	7	4	0	1	3	0	0	5	12	0	2	11	0	0	1	9	4	97.6%
CD8 Naïve	0	1	0	0	17	6051	2	0	0	0	0	0	0	0	1	16	0	0	0	1	4	0	0	0	90.6%
ILCs	29	11	1	86	38	4	4889	1	0	4	0	0	0	3	23	6	3	0	3	0	4	0	5	0	98.9%
iM	0	107	0	18	4	0	13	4237	20	0	11	0	0	1	1	0	1	3	17	7	0	0	17	1	94.8%
CD103+ DC	1	7	0	4	4	0	3	5	1653	0	6	0	0	0	0	0	0	0	6	4	0	0	0	0	94.3%
CD4 CM	2	0	0	4	0	0	0	1	0	1397	0	0	0	0	0	4	0	0	1	0	3	0	1	0	99.8%
CD11b+ DC	12	15	1	0	2	0	0	34	9	1	1037	0	0	0	0	0	0	8	11	4	0	0	9	1	98.1%
CD8 NKT	0	0	0	2	8	5	0	0	0	0	0	276	0	8	0	9	0	0	0	0	0	0	0	0	97.5%
CD4 NKT	0	0	0	24	0	0	0	1	0	5	0	0	692	4	0	0	0	0	0	0	8	0	0	0	89.6%
DN NKT	6	3	9	1	0	0	8	0	0	0	1	4	0	1225	5	1	1	1	3	3	1	0	4	0	99.3%
Tgd	31	9	0	4	2	5	13	4	0	0	0	0	0	3	1608	1	1	0	12	4	0	1	12	3	96.0%
CD8 CM	3	0	0	2	7	6	0	0	8	4	0	2	0	0	0	1959	0	1	2	1	1	0	0	1	96.9%
Eosinophils	28	25	8	1	0	0	8	0	0	2	0	0	0	2	0	1	4694	12	0	8	0	16	3	34	95.7%
IgM+ IgD-	16	14	3	6	2	0	6	3	2	0	3	0	0	3	1	0	4	5699	9	0	0	51	0	1	98.4%
eM	330	25	1	16	11	0	4	17	7	0	13	0	0	0	7	2	1	10	7709	5	0	0	11	10	96.3%
IgM- IgD+	5	0	2	1	1	0	7	1	1	1	0	0	0	0	0	0	9	0	0	8767	0	16	2	2	98.7%
CD4 Naïve	0	0	0	7	0	4	1	0	0	12	0	0	0	0	3	1	0	0	0	1	12267	1	0	0	99.6%
IgM+ IgD+	0	0	3	2	0	0	0	0	0	0	0	0	0	1	0	0	4	18	0	137	0	17472	4	1	93.9%
AM	1	15	7	3	1	0	2	9	3	0	10	0	0	0	2	0	10	0	4	2	0	0	23475	6	94.3%
Neutrophils	29	69	3	15	2	0	3	0	1	0	1	0	0	1	2	0	19	6	8	2	0	11	11	40596	95.0%

Confusion matrix comparing SVM classification to manual gating using a 250,000-cell training dataset equally sampled from all groups. Overall classification accuracy is 96.4%.

Figure B.6. ViSNE marker expression plots

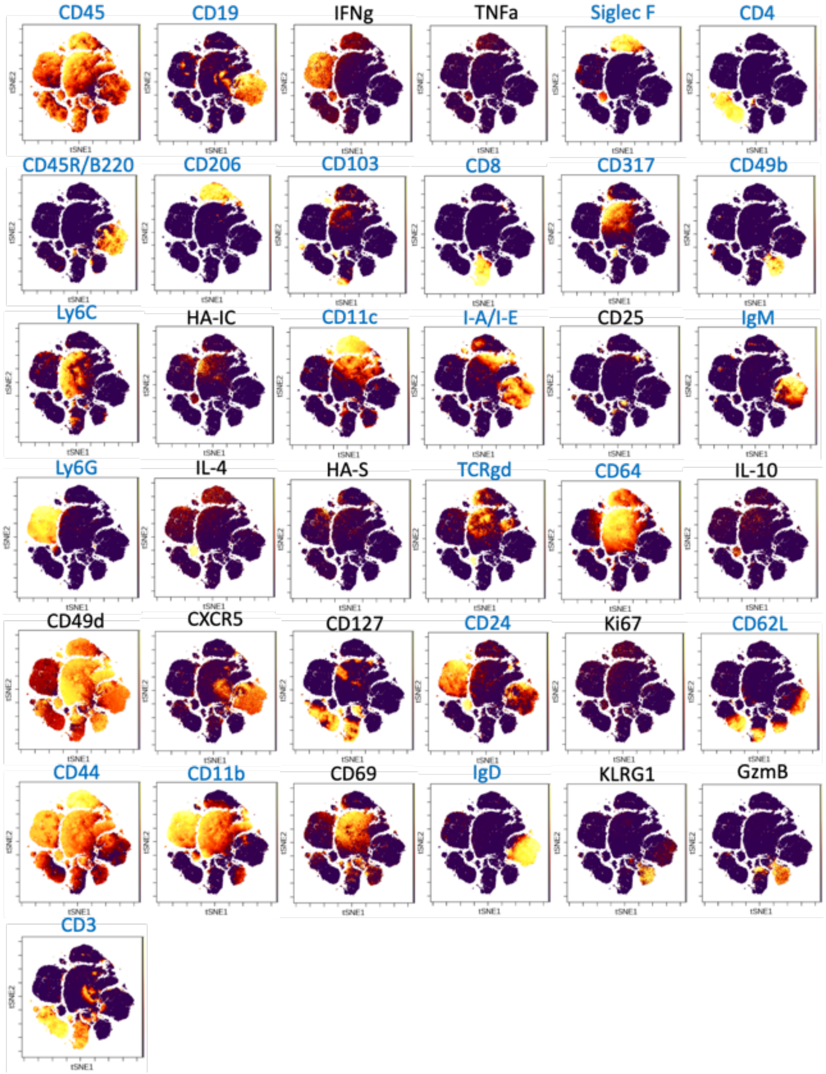

Heatmap of marker expression overlaid on the ViSNE map. ViSNE analysis was performed on 250,000 cells based on markers colored in blue.

Figure B.7. Comparison of HA^{IC}+ frequency and CD45+ frequency

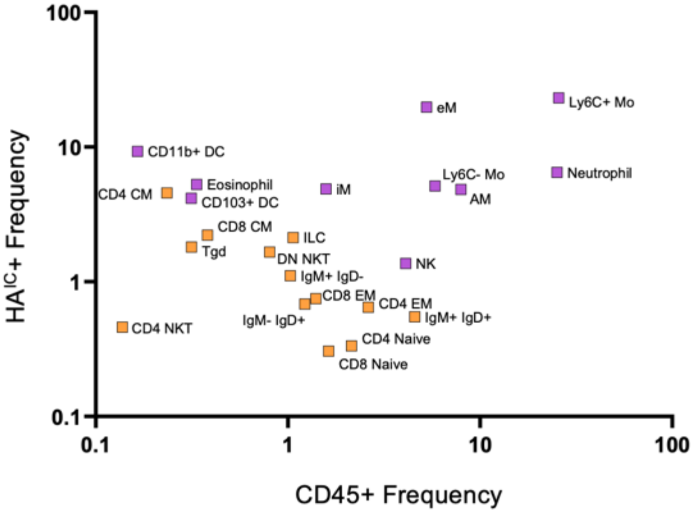

No trend is observed between HA^{IC}+ and CD45+ frequencies for either phagocytic cells (purple) or non-phagocytic cells (orange).

Figure B.8. Comparison of HA^{IC} and HA^{S} expression between young and aged mice.

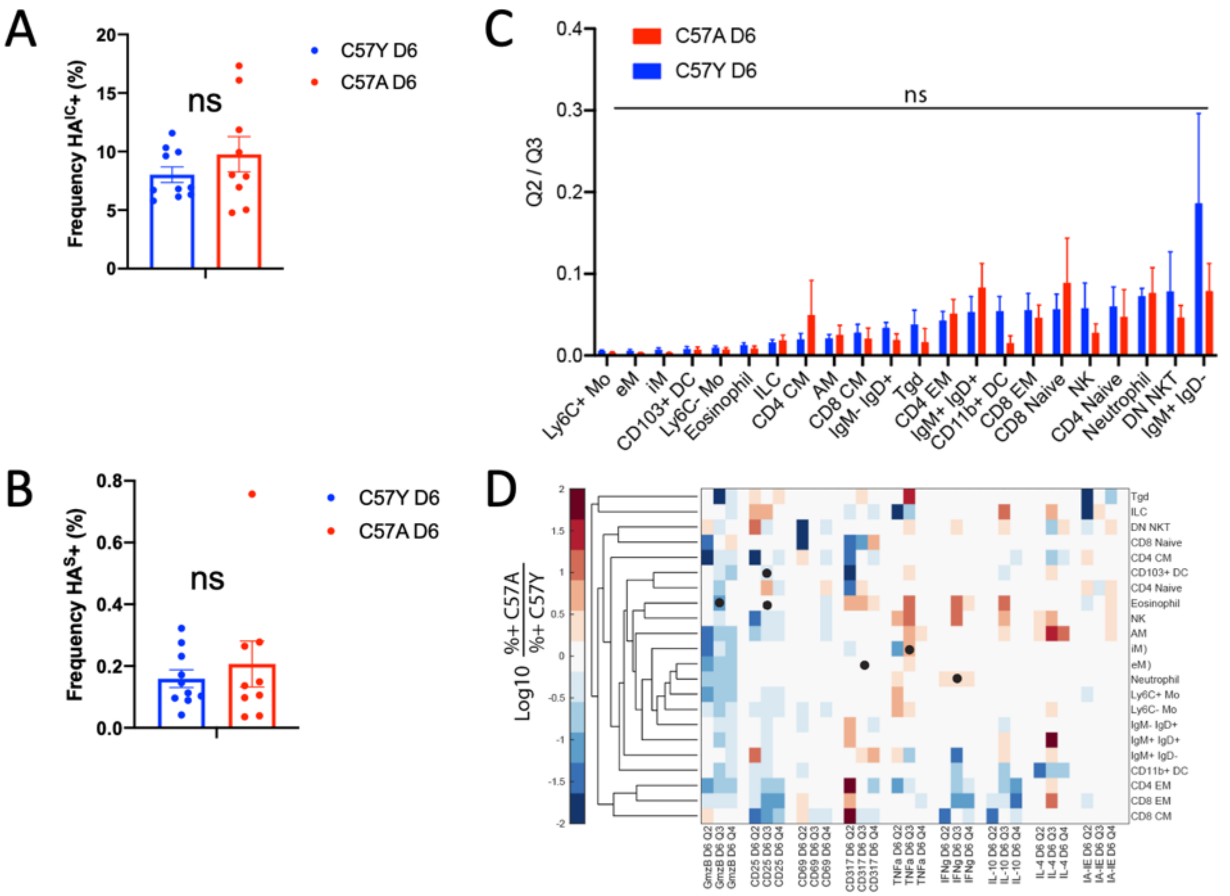

(**A**) HA^{IC}+ and (**B**) HA^{S}+ frequencies are not significantly different between young and aged mice. (**C**) Q2/Q3 frequency is not significantly different for any cell subset. (**D**) Log fold change in marker expression between young and aged mice for cells in Q2, Q3, and Q4. Significantly different subsets are indicated with a black dot. Data represent mean ± SEM. C57Y D6 *n* = 10, C57A D6 *n* = 9. Statistical comparisons in (A) and (B) computed by two-sided T test or (C) and (D) one-way ANOVA followed by Tukey's pairwise comparisons with FDR = 10%.

B.9 SVM classifier information

We used linear kernel SVM, as it has been demonstrated that linear decision boundaries are sufficient to achieve excellent class separability in CyTOF data.[371] Furthermore, linear models are less susceptible to overfitting that is often encountered with more complex supervised learners such as neural networks. The cleaned dataset was transformed using the inverse hyperbolic sine function and normalized to obtain a per-channel mean of 0 and standard deviation of 1. Multiclass SVM was implemented as a one-versus-one ensemble of binary SVM classifiers. For each learner, one class is positive, another is negative, and the rest are ignored. This design exhausts all combinations of class pair assignments for a total of 276 binary learners. To perform inference on a new test sample, all learners are queried, and the final prediction is obtained via majority vote.

In order to identify samples which do not belong to any of the predefined classes, we fitted optimal classification score-to-posterior probability transformation functions for each learner.[372] If two classes are perfectly separable, the optimal transformation function is the following step function, which transforms the score s_j corresponding to observation j to a positive class posterior probability

$$P(s_j) = \begin{cases} 0; & s < \max\limits_{y_k=-1} s_k \\ \pi; & \max\limits_{y_k=-1} s_k \leq s_j \leq \min\limits_{y_k=+1} s_k \\ 1; & s_j > \min\limits_{y_k=+1} s_k \end{cases},$$

Where π is the prior probability that an observation is in the positive class and y_k are binary class labels. If the classes are not separable, the optimal transformation is the sigmoid function

$$P(s_j) = \frac{1}{1 + \exp(As_j + B)}.$$

where parameters A and B are obtained by Platt's fitting method, a maximum likelihood technique which operates on the same training data used to train the original classifier.[372]

With the optimal score transformation function obtained for each learner, we generated a prediction matrix L and a positive class posterior probability matrix P for the 29 million cells in our dataset. Both matrices have dimensionality J x K, where J is the number of cells and K is the number of binary learners. Final class labels for each cell were obtained by a majority vote of all 276 binary learners (i.e. column-wise majority of each row in L), and final posterior probabilities were obtained by averaging those columns of P corresponding to learners which voted for the winning class label. Cells whose posterior probability fell below a threshold were rejected and placed in the "Other" class. We chose a threshold of 0.995, which corresponds to ~7% of cells being rejected in our dataset. This threshold is consistent with the empirical observation that 5-10% of cells were unable to be assigned to a user-defined cell gate.

References

1 Broxmeyer, L. Bird flu, influenza and 1918: the case for mutant Avian tuberculosis. *Med Hypotheses* **67**, 1006-1015, doi:10.1016/j.mehy.2006.05.002 (2006).

2 Wang, X. *et al.* Global burden of respiratory infections associated with seasonal influenza in children under 5 years in 2018: a systematic review and modelling study. *Lancet Glob Health* **8**, e497-e510, doi:10.1016/S2214-109X(19)30545-5 (2020).

3 Parrish, C. R., Murcia, P. R. & Holmes, E. C. Influenza virus reservoirs and intermediate hosts: dogs, horses, and new possibilities for influenza virus exposure of humans. *J Virol* **89**, 2990-2994, doi:10.1128/JVI.03146-14 (2015).

4 Johnson, N. P. & Mueller, J. Updating the accounts: global mortality of the 1918-1920 "Spanish" influenza pandemic. *Bull Hist Med* **76**, 105-115, doi:10.1353/bhm.2002.0022 (2002).

5 Nayak, D. P., Balogun, R. A., Yamada, H., Zhou, Z. H. & Barman, S. Influenza virus morphogenesis and budding. *Virus Res* **143**, 147-161, doi:10.1016/j.virusres.2009.05.010 (2009).

6 Rossman, J. S. & Lamb, R. A. Influenza virus assembly and budding. *Virology* **411**, 229-236, doi:10.1016/j.virol.2010.12.003 (2011).

7 Sugrue, R. J. & Hay, A. J. Structural characteristics of the M2 protein of influenza A viruses: evidence that it forms a tetrameric channel. *Virology* **180**, 617-624, doi:10.1016/0042-6822(91)90075-m (1991).

8 Lamb, R. A. & Choppin, P. W. The gene structure and replication of influenza virus. *Annu Rev Biochem* **52**, 467-506, doi:10.1146/annurev.bi.52.070183.002343 (1983).

9 Martin, K. & Helenius, A. Nuclear transport of influenza virus ribonucleoproteins: the viral matrix protein (M1) promotes export and inhibits import. *Cell* **67**, 117-130, doi:10.1016/0092-8674(91)90576-k (1991).

10 Braciale, T. J. Textbook of Influenza. *Textbook of Influenza*, doi:10.1002/9781118636817 (2013).

11 Drake, J. W. Rates of spontaneous mutation among RNA viruses. *Proc Natl Acad Sci U S A* **90**, 4171-4175, doi:10.1073/pnas.90.9.4171 (1993).

12 Smith, A. M. *et al.* Effect of 1918 PB1-F2 expression on influenza A virus infection kinetics. *PLoS Comput Biol* **7**, e1001081, doi:10.1371/journal.pcbi.1001081 (2011).

13 Cuevas, J. M., Geller, R., Garijo, R., Lopez-Aldeguer, J. & Sanjuan, R. Extremely High Mutation Rate of HIV-1 In Vivo. *PLoS Biol* **13**, e1002251, doi:10.1371/journal.pbio.1002251 (2015).

14 Das, S. R. *et al.* Defining influenza A virus hemagglutinin antigenic drift by sequential monoclonal antibody selection. *Cell Host Microbe* **13**, 314-323, doi:10.1016/j.chom.2013.02.008 (2013).

15 Bangaru, S. *et al.* A Site of Vulnerability on the Influenza Virus Hemagglutinin Head Domain Trimer Interface. *Cell* **177**, 1136-1152 e1118, doi:10.1016/j.cell.2019.04.011 (2019).

16 Jennings, G. T. & Bachmann, M. F. The coming of age of virus-like particle vaccines. *Biol Chem* **389**, 521-536, doi:10.1515/bc.2008.064 (2008).

17 Wong, S. S. & Webby, R. J. Traditional and new influenza vaccines. *Clin Microbiol Rev* **26**, 476-492, doi:10.1128/CMR.00097-12 (2013).

18 Hoft, D. F. *et al.* Live and inactivated influenza vaccines induce similar humoral responses, but only live vaccines induce diverse T-cell responses in young children. *J Infect Dis* **204**, 845-853, doi:10.1093/infdis/jir436 (2011).

19 Rajao, D. S. & Perez, D. R. Universal Vaccines and Vaccine Platforms to Protect against Influenza Viruses in Humans and Agriculture. *Front Microbiol* **9**, 123, doi:10.3389/fmicb.2018.00123 (2018).

20 Calzas, C. & Chevalier, C. Innovative Mucosal Vaccine Formulations Against Influenza A Virus Infections. *Front Immunol* **10**, 1605, doi:10.3389/fimmu.2019.01605 (2019).

21 Maassab, H. F. & Bryant, M. L. The development of live attenuated cold-adapted influenza virus vaccine for humans. *Rev Med Virol* **9**, 237-244, doi:10.1002/(sici)1099-1654(199910/12)9:4<237::aid-rmv252>3.0.co;2-g (1999).

22 Pebody, R., McMenamin, J. & Nohynek, H. Live attenuated influenza vaccine (LAIV): recent effectiveness results from the USA and implications for LAIV programmes elsewhere. *Arch Dis Child* **103**, 101-105, doi:10.1136/archdischild-2016-312165 (2018).

23 Matrajt, L., Halloran, M. E. & Antia, R. Successes and Failures of the Live-attenuated Influenza Vaccine: Can We Do Better? *Clin Infect Dis* **70**, 1029-1037, doi:10.1093/cid/ciz358 (2020).

24 Zhou, B. *et al.* Reversion of Cold-Adapted Live Attenuated Influenza Vaccine into a Pathogenic Virus. *J Virol* **90**, 8454-8463, doi:10.1128/JVI.00163-16 (2016).

25 White, J. A. *et al.* Development of a stable liquid formulation of live attenuated influenza vaccine. *Vaccine* **34**, 3676-3683, doi:10.1016/j.vaccine.2016.04.074 (2016).

26 Kumru, O. S. *et al.* Vaccine instability in the cold chain: mechanisms, analysis and formulation strategies. *Biologicals* **42**, 237-259, doi:10.1016/j.biologicals.2014.05.007 (2014).

27 Shinya, K. *et al.* Avian flu: influenza virus receptors in the human airway. *Nature* **440**, 435-436, doi:10.1038/440435a (2006).

28 van Riel, D. *et al.* H5N1 Virus Attachment to Lower Respiratory Tract. *Science* **312**, 399, doi:10.1126/science.1125548 (2006).

29 Lambert, L. C. & Fauci, A. S. Influenza vaccines for the future. *N Engl J Med* **363**, 2036-2044, doi:10.1056/NEJMra1002842 (2010).

30 Blumberg, B. S., Alter, H. J. & Visnich, S. A "New" Antigen in Leukemia Sera. *JAMA* **191**, 541-546, doi:10.1001/jama.1965.03080070025007 (1965).

31 Rappuoli, R. Bridging the knowledge gaps in vaccine design. *Nat Biotechnol* **25**, 1361-1366, doi:10.1038/nbt1207-1361 (2007).

32 Krugman, S. The newly licensed hepatitis B vaccine. Characteristics and indications for use. *JAMA* **247**, 2012-2015, doi:10.1001/jama.1982.03320390074052 (1982).

33 McAleer, W. J. *et al.* Human hepatitis B vaccine from recombinant yeast. *Nature* **307**, 178-180, doi:10.1038/307178a0 (1984).

34 Cormode, D. P., Skajaa, T., Fayad, Z. A. & Mulder, W. J. Nanotechnology in medical imaging: probe design and applications. *Arterioscler Thromb Vasc Biol* **29**, 992-1000, doi:10.1161/ATVBAHA.108.165506 (2009).

35 Manchester, M. & Singh, P. Virus-based nanoparticles (VNPs): platform technologies for diagnostic imaging. *Adv Drug Deliv Rev* **58**, 1505-1522, doi:10.1016/j.addr.2006.09.014 (2006).

36 Schwarz, B. & Douglas, T. Development of virus-like particles for diagnostic and prophylactic biomedical applications. *Wiley Interdiscip Rev Nanomed Nanobiotechnol* **7**, 722-735, doi:10.1002/wnan.1336 (2015).

37 Shen, L. *et al.* Efficient encapsulation of Fe(3)O(4) nanoparticles into genetically engineered hepatitis B core virus-like particles through a specific interaction for potential bioapplications. *Small* **11**, 1190-1196, doi:10.1002/smll.201401952 (2015).

38 Li, F. & Wang, Q. Fabrication of nanoarchitectures templated by virus-based nanoparticles: strategies and applications. *Small* **10**, 230-245, doi:10.1002/smll.201301393 (2014).

39 Wnek, M. *et al.* Fabrication and characterization of gold nano-wires templated on virus-like arrays of tobacco mosaic virus coat proteins. *Nanotechnology* **24**, 025605, doi:10.1088/0957-4484/24/2/025605 (2013).

40 Maity, B., Fujita, K. & Ueno, T. Use of the confined spaces of apo-ferritin and virus capsids as nanoreactors for catalytic reactions. *Curr Opin Chem Biol* **25**, 88-97, doi:10.1016/j.cbpa.2014.12.026 (2015).

41 Patterson, D., Edwards, E. & Douglas, T. Hybrid Nanoreactors: Coupling Enzymes and Small-Molecule Catalysts within Virus-Like Particles. *Isr J Chem* **55**, 96-101, doi:10.1002/ijch.201400092 (2015).

42 Patterson, D. P., McCoy, K., Fijen, C. & Douglas, T. Constructing catalytic antimicrobial nanoparticles by encapsulation of hydrogen peroxide producing enzyme inside the P22 VLP. *J Mater Chem B* **2**, 5948-5951, doi:10.1039/c4tb00983e (2014).

43 Ma, Y., Nolte, R. J. & Cornelissen, J. J. Virus-based nanocarriers for drug delivery. *Adv. Drug Deliv. Rev.* **64**, 811-825, doi:10.1016/j.addr.2012.01.005 (2012).

44 Molino, N. M. & Wang, S. W. Caged protein nanoparticles for drug delivery. *Curr. Opin. Biotechnol.* **28**, 75-82, doi:10.1016/j.copbio.2013.12.007 (2014).

45 Panda, S. K., Kapur, N., Paliwal, D. & Durgapal, H. Recombinant Hepatitis E virus like particles can function as RNA nanocarriers. *J. Nanobiotechnology* **13**, 44, doi:10.1186/s12951-015-0101-9 (2015).

46 Petry, H., Goldmann, C., Ast, O. & Luke, W. The use of virus-like particles for gene transfer. *Current Opinion in Molecular Therapeutics* **5**, 524-528 (2003).

47 Zuber, G., Dontenwill, M. & Behr, J. P. Synthetic viruslike particles for targeted gene delivery to alphavbeta3 integrin-presenting endothelial cells. *Mol. Pharm.* **6**, 1544-1552, doi:10.1021/mp900105q (2009).

48 Brasch, M., Voets, I. K., Koay, M. S. & Cornelissen, J. J. Phototriggered cargo release from virus-like assemblies. *Faraday Discuss.* **166**, 47-57 (2013).

49 de la Escosura, A. *et al.* Viral capsids as templates for the production of monodisperse Prussian blue nanoparticles. *Chem. Commun. (Camb)*, 1542-1544, doi:10.1039/b800936h (2008).

50 Sanchez-Sanchez, L. *et al.* Chemotherapy pro-drug activation by biocatalytic virus-like nanoparticles containing cytochrome P450. *Enzyme Microb. Technol.* **60**, 24-31, doi:10.1016/j.enzmictec.2014.04.003 (2014).

51 Pickett, G. G. & Peabody, D. S. Encapsidation of heterologous RNAs by bacteriophage MS2 coat protein. *Nucleic Acids Res.* **21**, 4621-4626 (1993).

52 Ashley, C. E. *et al.* Cell-specific delivery of diverse cargos by bacteriophage MS2 virus-like particles. *ACS Nano.* **5**, 5729-5745, doi:10.1021/nn201397z (2011).

53 Rhee, J. *et al.* Colorful virus-like particles: fluorescent protein packaging by the Qβ capsid. *Biomacromolecules* **12**, 3977-3981 (2011).

54 Fiedler, J. D., Brown, S. D., Lau, J. L. & Finn, M. G. RNA-Directed Packaging of Enzymes within Virus-like Particles. *Angew Chem Int Edit* **49**, 9648-9651, doi:10.1002/anie.201005243 (2010).

55 Cortes-Perez, N. G. *et al.* Rotavirus-like particles: a novel nanocarrier for the gut. *J. Biomed. Biotechnol.* **2010**, 317545, doi:10.1155/2010/317545 (2010).

56 Fang, C. Y. *et al.* Inhibition of human bladder cancer growth by a suicide gene delivered by JC polyomavirus virus-like particles in a mouse model. *J. Urol.* **193**, 2100-2106, doi:10.1016/j.juro.2015.01.084 (2015).

57 Toporkiewicz, M., Meissner, J., Matusewicz, L., Czogalla, A. & Sikorski, A. F. Toward a magic or imaginary bullet? Ligands for drug targeting to cancer cells: principles, hopes, and challenges. *Int. J. Nanomedicine* **10**, 1399-1414, doi:10.2147/IJN.S74514 (2015).

58 Galaway, F. A. & Stockley, P. G. MS2 viruslike particles: a robust, semisynthetic targeted drug delivery platform. *Mol. Pharm.* **10**, 59-68, doi:10.1021/mp3003368 (2013).

59 Kitai, Y. *et al.* Cell selective targeting of a simian virus 40 virus-like particle conjugated to epidermal growth factor. *J. Biotechnol.* **155**, 251-256, doi:10.1016/j.jbiotec.2011.06.030 (2011).

60 Pokorski, J. K., Hovlid, M. L. & Finn, M. G. Cell targeting with hybrid Qbeta virus-like particles displaying epidermal growth factor. *Chembiochem* **12**, 2441-2447, doi:10.1002/cbic.201100469 (2011).

61 Ren, Y., Wong, S. M. & Lim, L. Y. Folic acid-conjugated protein cages of a plant virus: a novel delivery platform for doxorubicin. *Bioconjug. Chem.* **18**, 836-843, doi:10.1021/bc060361p (2007).

62 Deo, V. K., Kato, T. & Park, E. Y. Chimeric virus-like particles made using GAG and M1 capsid proteins providing dual drug delivery and vaccination platform. *Mol. Pharm.* **12**, 839-845, doi:10.1021/mp500860x (2015).

63 Kato, T., Yui, M., Deo, V. K. & Park, E. Y. Development of Rous sarcoma Virus-like Particles Displaying hCC49 scFv for Specific Targeted Drug Delivery to Human Colon Carcinoma Cells. *Pharm. Res.* **32**, 3699-3707, doi:10.1007/s11095-015-1730-2 (2015).

64 Poulin, K. L. *et al.* Retargeting of Adenovirus Vectors through Genetic Fusion of a Single-Chain or Single-Domain Antibody to Capsid Protein IX. *J. Virol.* **84**, 10074-10086, doi:10.1128/Jvi.02665-09 (2010).

65 Cohen, B. A. & Bergkvist, M. Targeted in vitro photodynamic therapy via aptamer-labeled, porphyrin-loaded virus capsids. *J. Photochem. Photobiol. B.* **121**, 67-74, doi:10.1016/j.jphotobiol.2013.02.013 (2013).

66 Stephanopoulos, N., Tong, G. J., Hsiao, S. C. & Francis, M. B. Dual-surface modified virus capsids for targeted delivery of photodynamic agents to cancer cells. *ACS Nano.* **4**, 6014-6020, doi:10.1021/nn1014769 (2010).

67 Tong, G. J., Hsiao, S. C., Carrico, Z. M. & Francis, M. B. Viral capsid DNA aptamer conjugates as multivalent cell-targeting vehicles. *J. Am. Chem. Soc.* **131**, 11174-11178, doi:10.1021/ja903857f (2009).

68 Shishido, T. *et al.* Affibody-displaying bionanocapsules for specific drug delivery to HER2-expressing cancer cells. *Bioorg. Med. Chem. Lett.* **20**, 5726-5731, doi:10.1016/j.bmcl.2010.08.011 (2010).

69 Bachmann, M. F. & Zinkernagel, R. M. Neutralizing antiviral B cell responses. *Annu Rev Immunol* **15**, 235-270, doi:10.1146/annurev.immunol.15.1.235 (1997).

70 Trovato, M. & De Berardinis, P. Novel antigen delivery systems. *World J Virol* **4**, 156-168, doi:10.5501/wjv.v4.i3.156 (2015).

71 Rosenthal, J. A., Chen, L., Baker, J. L., Putnam, D. & DeLisa, M. P. Pathogen-like particles: biomimetic vaccine carriers engineered at the nanoscale. *Curr Opin Biotechnol* **28**, 51-58, doi:10.1016/j.copbio.2013.11.005 (2014).

72 Spohn, G. *et al.* Active immunization with IL-1 displayed on virus-like particles protects from autoimmune arthritis. *Eur J Immunol* **38**, 877-887, doi:10.1002/eji.200737989 (2008).

73 Ambuhl, P. M. *et al.* A vaccine for hypertension based on virus-like particles: preclinical efficacy and phase I safety and immunogenicity. *J Hypertens* **25**, 63-72, doi:10.1097/HJH.0b013e32800ff5d6 (2007).

74 Rohn, T. A. *et al.* Vaccination against IL-17 suppresses autoimmune arthritis and encephalomyelitis. *Eur J Immunol* **36**, 2857-2867, doi:10.1002/eji.200636658 (2006).

75 Chackerian, B., Lenz, P., Lowy, D. R. & Schiller, J. T. Determinants of autoantibody induction by conjugated papillomavirus virus-like particles. *J Immunol* **169**, 6120-6126, doi:10.4049/jimmunol.169.11.6120 (2002).

76 Braun, M. *et al.* Virus-like particles induce robust human T-helper cell responses. *Eur J Immunol* **42**, 330-340, doi:10.1002/eji.201142064 (2012).

77 Swain, S. L., McKinstry, K. K. & Strutt, T. M. Expanding roles for CD4(+) T cells in immunity to viruses. *Nature reviews. Immunology* **12**, 136-148, doi:10.1038/nri3152 (2012).

78 Davidson, E. & Doranz, B. J. A high-throughput shotgun mutagenesis approach to mapping B-cell antibody epitopes. *Immunology* **143**, 13-20, doi:10.1111/imm.12323 (2014).

79 Li Pira, G., Ivaldi, F., Moretti, P. & Manca, F. High throughput T epitope mapping and vaccine development. *J. Biomed. Biotechnol.* **2010**, 325720, doi:10.1155/2010/325720 (2010).

80 Patronov, A. & Doytchinova, I. T-cell epitope vaccine design by immunoinformatics. *Open. Biol.* **3**, 120139, doi:10.1098/rsob.120139 (2013).

81 Wen, F., Esteban, O. & Zhao, H. Rapid identification of CD4+ T-cell epitopes using yeast displaying pathogen-derived peptide library. *J Immunol Methods* **336**, 37-44, doi:10.1016/j.jim.2008.03.008 (2008).

82 Wen, F. & Zhao, H. Construction and screening of an antigen-derived peptide library displayed on yeast cell surface for CD4+ T cell epitope identification. *Methods Mol. Biol.* **1061**, 245-264, doi:10.1007/978-1-62703-589-7_15 (2013).

83 Kirchmeier, M. *et al.* Enveloped virus-like particle expression of human cytomegalovirus glycoprotein B antigen induces antibodies with potent and broad neutralizing activity. *Clin. Vaccine Immunol.* **21**, 174-180, doi:10.1128/CVI.00662-13 (2014).

84 Lagging, L. M., Meyer, K., Owens, R. J. & Ray, R. Functional role of hepatitis C virus chimeric glycoproteins in the infectivity of pseudotyped virus. *J. Virol.* **72**, 3539-3546 (1998).

85 Long, Q. *et al.* Virus-like particles presenting interleukin-33 molecules: immunization characteristics and potentials of blockingIL-33/ST2 pathway in allergic airway inflammation. *Hum. Vaccin. Immunother.* **10**, 2303-2311, doi:10.4161/hv.29425 (2014).

86 Lv, L. *et al.* Production and immunogenicity of chimeric virus-like particles containing the spike glycoprotein of infectious bronchitis virus. *J. Vet. Sci.* **15**, 209-216 (2014).

87 Ogembo, J. G. *et al.* A chimeric EBV gp350/220-based VLP replicates the virion B-cell attachment mechanism and elicits long-lasting neutralizing antibodies in mice. *J. Transl. Med.* **13**, 50, doi:10.1186/s12967-015-0415-2 (2015).

88 Qi, Y. *et al.* Incorporation of membrane-anchored flagellin or Escherichia coli heat-labile enterotoxin B subunit enhances the immunogenicity of rabies virus-like particles in mice and dogs. *Front. Microbiol.* **6**, 169, doi:10.3389/fmicb.2015.00169 (2015).

89 Schmidt, M. R. *et al.* Modification of the respiratory syncytial virus f protein in virus-like particles impacts generation of B cell memory. *J. Virol.* **88**, 10165-10176, doi:10.1128/JVI.01250-14 (2014).

90 Shahana, P. V., Das, D., Gontu, A., Chandran, D. & Maithal, K. Efficient production of Tymovirus like particles displaying immunodominant epitopes of Japanese Encephalitis Virus envelope protein. *Protein Expr. Purif.* **113**, 35-43, doi:10.1016/j.pep.2015.03.017 (2015).

91 Shen, H. *et al.* Assembly and immunological properties of a bivalent virus-like particle (VLP) for avian influenza and Newcastle disease. *Virus Res.* **178**, 430-436, doi:10.1016/j.virusres.2013.09.009 (2013).

92 Xue, C. *et al.* Chimeric influenza-virus-like particles containing the porcine reproductive and respiratory syndrome virus GP5 protein and the influenza virus HA and M1 proteins. *Arch. Virol.* **159**, 3043-3051, doi:10.1007/s00705-014-2178-0 (2014).

93 Jegerlehner, A. *et al.* A molecular assembly system that renders antigens of choice highly repetitive for induction of protective B cell responses. *Vaccine* **20**, 3104-3112, doi:10.1016/S0264-410x(02)00266-9 (2002).

94 Peacey, M., Wilson, S., Baird, M. A. & Ward, V. K. Versatile RHDV virus-like particles: incorporation of antigens by genetic modification and chemical conjugation. *Biotechnol. Bioeng.* **98**, 968-977, doi:10.1002/bit.21518 (2007).

95 Cronin, J., Zhang, X. Y. & Reiser, J. Altering the tropism of lentiviral vectors through pseudotyping. *Curr. Gene Ther.* **5**, 387-398 (2005).

96 Pushko, P. *et al.* Influenza virus-like particle can accommodate multiple subtypes of hemagglutinin and protect from multiple influenza types and subtypes. *Vaccine* **29**, 5911-5918, doi:10.1016/j.vaccine.2011.06.068 (2011).

97 Tretyakova, I., Pearce, M. B., Florese, R., Tumpey, T. M. & Pushko, P. Intranasal vaccination with H5, H7 and H9 hemagglutinins co-localized in a virus-like particle protects ferrets from multiple avian influenza viruses. *Virology* **442**, 67-73, doi:10.1016/j.virol.2013.03.027 (2013).

98 Hill, B. D., Zak, A., Khera, E. & Wen, F. Engineering Virus-like Particles for Antigen and Drug Delivery. *Curr Protein Pept Sci* **19**, 112-127, doi:10.2174/1389203718666161122113041 (2018).

99 Ding, F. X. *et al.* Multiepitope Peptide-Loaded Virus-Like Particles as a Vaccine Against Hepatitis B Virus-Related Hepatocellular Carcinoma. *Hepatology* **49**, 1492-1502, doi:10.1002/hep.22816 (2009).

100 Birkett, A. *et al.* A modified hepatitis B virus core particle containing multiple epitopes of the Plasmodium falciparum circumsporozoite protein provides a highly immunogenic malaria vaccine in preclinical analyses in rodent and primate hosts. *Infect. Immun.* **70**, 6860-6870 (2002).

101 Kim, M. C. *et al.* Virus-like particles containing multiple M2 extracellular domains confer improved cross-protection against various subtypes of influenza virus. *Mol. Ther.* **21**, 485-492, doi:10.1038/mt.2012.246 (2013).

102 De Filette, M. *et al.* Universal influenza A vaccine: optimization of M2-based constructs. *Virology* **337**, 149-161, doi:10.1016/j.virol.2005.04.004 (2005).

103 Yong, C. Y., Yeap, S. K., Ho, K. L., Omar, A. R. & Tan, W. S. Potential recombinant vaccine against influenza A virus based on M2e displayed on nodaviral capsid nanoparticles. *Int. J. Nanomedicine* **10**, 2751-2763, doi:10.2147/IJN.S77405 (2015).

104 Rueda, P. *et al.* Engineering parvovirus-like particles for the induction of B-cell, CD4(+) and CTL responses. *Vaccine* **18**, 325-332, doi:10.1016/s0264-410x(99)00202-9 (1999).

105 Salfeld, J., Pfaff, E., Noah, M. & Schaller, H. Antigenic determinants and functional domains in core antigen and e antigen from hepatitis B virus. *J. Virol.* **63**, 798-808 (1989).

106 Schodel, F. *et al.* The position of heterologous epitopes inserted in hepatitis B virus core particles determines their immunogenicity. *J. Virol.* **66**, 106-114 (1992).

107 Forsstrom, B. *et al.* Dissecting antibodies with regards to linear and conformational epitopes. *PLoS One* **10**, e0121673, doi:10.1371/journal.pone.0121673 (2015).

108 Wu, Y. *et al.* A potent broad-spectrum protective human monoclonal antibody crosslinking two haemagglutinin monomers of influenza A virus. *Nat. Commun.* **6**, 7708, doi:10.1038/ncomms8708 (2015).

109 Correia, B. E. *et al.* Proof of principle for epitope-focused vaccine design. *Nature* **507**, 201-206, doi:10.1038/nature12966 (2014).

110 Magro, M. *et al.* Neutralizing antibodies against the preactive form of respiratory syncytial virus fusion protein offer unique possibilities for clinical intervention. *P Natl Acad Sci USA* **109**, 3089-3094, doi:10.1073/pnas.1115941109 (2012).

111 Skehel, J. J. & Wiley, D. C. Coiled coils in both intracellular vesicle and viral membrane fusion. *Cell* **95**, 871-874, doi:Doi 10.1016/S0092-8674(00)81710-9 (1998).

112 Sia, S. K. & Kim, P. S. Protein grafting of an HIV-1-inhibiting epitope. *P Natl Acad Sci USA* **100**, 9756-9761, doi:10.1073/pnas.1733910100 (2003).

113 Chakraborty, S., Rao, B. J., Asgeirsson, B. & Dandekar, A. Characterizing alpha helical properties of Ebola viral proteins as potential targets for inhibition of alpha-helix mediated protein-protein interactions. *F1000Research* **3**, 251 (2014).

114 Ekiert, D. C. *et al.* Antibody recognition of a highly conserved influenza virus epitope. *Science* **324**, 246-251, doi:10.1126/science.1171491 (2009).

115 Anggraeni, M. R. *et al.* Sensitivity of immune response quality to influenza helix 190 antigen structure displayed on a modular virus-like particle. *Vaccine* **31**, 4428-4435, doi:10.1016/j.vaccine.2013.06.087 (2013).

116 Relf, W. A. *et al.* Mapping a conserved conformational epitope from the M protein of group A streptococci. *Pept. Res.* **9**, 12-20 (1996).

117 Yan, Z., Hartsock, W. J., Qian, Z., Holmes, K. V. & Hodges, R. S. in *Small Wonders: Peptides for Disease Control* Vol. 1095 (eds Kanniah Rajasekaran, Jeffrey W. Cary, Jesse M. Jaynes, & Emilio Montesinos) 93-136 (American Chemical Society, Washington, DC, 2012).

118 De Berardinis, P., Guardiola, J. & Manca, F. Epitope context and reshaping of activated T helper cell repertoire. *Hum. Immunol.* **54**, 189-193 (1997).

119 Del Val, M., Schlicht, H. J., Ruppert, T., Reddehase, M. J. & Koszinowski, U. H. Efficient processing of an antigenic sequence for presentation by MHC class I molecules depends on its neighboring residues in the protein. *Cell* **66**, 1145-1153, doi:10.1016/0092-8674(91)90037-y (1991).

120 Le Gall, S., Stamegna, P. & Walker, B. D. Portable flanking sequences modulate CTL epitope processing. *J. Clin. Invest.* **117**, 3563-3575, doi:10.1172/JCI32047 (2007).

121 Steers, N. J. *et al.* Designing the epitope flanking regions for optimal generation of CTL epitopes. *Vaccine* **32**, 3509-3516, doi:10.1016/j.vaccine.2014.04.039 (2014).

122 Rueda, P., Moron, G., Sarraseca, J., Leclerc, C. & Casal, J. I. Influence of flanking sequences on presentation efficiency of a CD8+ cytotoxic T-cell epitope delivered by parvovirus-like particles. *J. Gen. Virol.* **85**, 563-572, doi:10.1099/vir.0.19525-0 (2004).

123 Akram, A. & Inman, R. D. Immunodominance: a pivotal principle in host response to viral infections. *Clin. Immunol.* **143**, 99-115, doi:10.1016/j.clim.2012.01.015 (2012).

124 Sant, A. J. *et al.* Immunodominance in CD4 T-cell responses: implications for immune responses to influenza virus and for vaccine design. *Expert Rev. Vaccines* **6**, 357-368, doi:10.1586/14760584.6.3.357 (2007).

125 Wilson, E. H. & Hunter, C. A. Immunodominance and recognition of intracellular pathogens. *J. Infect. Dis.* **198**, 1579-1581, doi:10.1086/593020 (2008).

126 Frickel, E. M. *et al.* Parasite stage-specific recognition of endogenous Toxoplasma gondii-derived CD8+ T cell epitopes. *J. Infect. Dis.* **198**, 1625-1633, doi:10.1086/593019 (2008).

127 Recker, M. *et al.* Transient cross-reactive immune responses can orchestrate antigenic variation in malaria. *Nature* **429**, 555-558, doi:10.1038/nature02486 (2004).

128 Schreiber, H., Wu, T. H., Nachman, J. & Kast, W. M. Immunodominance and tumor escape. *Semin. Cancer Biol.* **12**, 25-31, doi:10.1006/scbi.2001.0401 (2002).

129 Friedrich, T. C. *et al.* Subdominant CD8+ T-cell responses are involved in durable control of AIDS virus replication. *J. Virol.* **81**, 3465-3476, doi:10.1128/JVI.02392-06 (2007).

130 Newell, E. W. Higher throughput methods of identifying T cell epitopes for studying outcomes of altered antigen processing and presentation. *Front. Immunol.* **4**, 430, doi:10.3389/fimmu.2013.00430 (2013).

131 Newell, E. W. & Davis, M. M. Beyond model antigens: high-dimensional methods for the analysis of antigen-specific T cells. *Nat. Biotechnol.* **32**, 149-157, doi:10.1038/nbt.2783 (2014).

132 Corbiere, V. *et al.* Antigen spreading contributes to MAGE vaccination-induced regression of melanoma metastases. *Cancer Res.* **71**, 1253-1262, doi:10.1158/0008-5472.CAN-10-2693 (2011).

133 Venkatesha, S. H., Durai, M. & Moudgil, K. D. Infection and Autoimmunity. *Infection and Autoimmunity*, 45-68, doi:10.1016/B978-0-444-63269-2.00003-9 (2015).

134 Kreiter, S. *et al.* Mutant MHC class II epitopes drive therapeutic immune responses to cancer. *Nature* **520**, 692-696 (2015).

135 D'Aoust, M. A. *et al.* The production of hemagglutinin-based virus-like particles in plants: a rapid, efficient and safe response to pandemic influenza. *Plant Biotechnol J* **8**, 607-619, doi:10.1111/j.1467-7652.2009.00496.x (2010).

136 Bright, R. A. *et al.* Cross-clade protective immune responses to influenza viruses with H5N1 HA and NA elicited by an influenza virus-like particle. *PLoS One* **3**, e1501, doi:10.1371/journal.pone.0001501 (2008).

137 Braun, M. *et al.* Virus-like particles induce robust human T-helper cell responses. *Eur. J. Immunol.* **42**, 330-340, doi:10.1002/eji.201142064 (2012).

138 Jennings, G. T. & Bachmann, M. F. The coming of age of virus-like particle vaccines. *Biol. Chem.* **389**, 521-536 (2008).

139 Storni, T. *et al.* Critical role for activation of antigen-presenting cells in priming of cytotoxic T cell responses after vaccination with virus-like particles. *J. Immunol.* **168**, 2880-2886 (2002).

140 Appay, V., Douek, D. C. & Price, D. A. CD8+ T cell efficacy in vaccination and disease. *Nat. Med.* **14**, 623-628, doi:10.1038/nm.f.1774 (2008).

141 Doherty, P. C. & Kelso, A. Toward a broadly protective influenza vaccine. *J. Clin. Invest.* **118**, 3273-3275, doi:10.1172/JCI37232 (2008).

142 Wilkinson, T. M. *et al.* Preexisting influenza-specific CD4+ T cells correlate with disease protection against influenza challenge in humans. *Nat. Med.* **18**, 274-280, doi:10.1038/nm.2612 (2012).

143 De Gregorio, E., D'Oro, U. & Wack, A. Immunology of TLR-independent vaccine adjuvants. *Curr Opin Immunol* **21**, 339-345, doi:10.1016/j.coi.2009.05.003 (2009).

144 van Montfoort, N., van der Aa, E. & Woltman, A. M. Understanding MHC class I presentation of viral antigens by human dendritic cells as a basis for rational design of therapeutic vaccines. *Front Immunol* **5**, 182, doi:10.3389/fimmu.2014.00182 (2014).

145 Neefjes, J., Jongsma, M. L., Paul, P. & Bakke, O. Towards a systems understanding of MHC class I and MHC class II antigen presentation. *Nature reviews. Immunology* **11**, 823-836, doi:10.1038/nri3084 (2011).

146 Tipping, P. G. Toll-like receptors: the interface between innate and adaptive immunity. *J. Am. Soc. Nephrol.* **17**, 1769-1771, doi:10.1681/ASN.2006050489 (2006).

147 Kasturi, S. P. *et al.* Programming the magnitude and persistence of antibody responses with innate immunity. *Nature* **470**, 543-547, doi:10.1038/nature09737 (2011).

148 Rahman, A. H., Taylor, D. K. & Turka, L. A. The contribution of direct TLR signaling to T cell responses. *Immunol. Res.* **45**, 25-36, doi:10.1007/s12026-009-8113-x (2009).

149 Singh, M. & O'Hagan, D. Advances in vaccine adjuvants. *Nat. Biotechnol.* **17**, 1075-1081, doi:10.1038/15058 (1999).

150 Storni, T. *et al.* Nonmethylated CG motifs packaged into virus-like particles induce protective cytotoxic T cell responses in the absence of systemic side effects. *Journal of Immunology* **172**, 1777-1785, doi:10.4049/jimmunol.172.3.1777 (2004).

151 Goldinger, S. M. *et al.* Nano-particle vaccination combined with TLR-7 and -9 ligands triggers memory and effector CD8(+) T-cell responses in melanoma patients. *Eur. J. Immunol.* **42**, 3049-3061, doi:10.1002/eji.201142361 (2012).

152 Speiser, D. E. *et al.* Memory and effector CD8 T-cell responses after nanoparticle vaccination of melanoma patients. *J. Immunother.* **33**, 848-858, doi:10.1097/CJI.0b013e3181f1d614 (2010).

153 Lebel, M.-È. *et al.* Nanoparticle adjuvant sensing by TLR7 enhances CD8+ T cell-mediated protection from Listeria monocytogenes infection. *Journal of immunology* **192**, 1071-1078, doi:10.4049/jimmunol.1302030 (2014).

154 Chua, B. Y. *et al.* Hepatitis C VLPs Delivered to Dendritic Cells by a TLR2 Targeting Lipopeptide Results in Enhanced Antibody and Cell-Mediated Responses. *PLoS ONE* **7**, e47492, doi:10.1371/journal.pone.0047492 (2012).

155 Wang, B. Z. *et al.* Incorporation of Membrane-Anchored Flagellin into Influenza Virus-Like Particles Enhances the Breadth of Immune Responses. *Journal of Virology* **82**, 11813-11823, doi:10.1128/Jvi.01076-08 (2008).

156 Wang, B. Z. *et al.* Incorporation of membrane-anchored flagellin into influenza virus-like particles enhances the breadth of immune responses. *J Virol* **82**, 11813-11823, doi:10.1128/JVI.01076-08 (2008).

157 Taylor, D. N. *et al.* Induction of a potent immune response in the elderly using the TLR-5 agonist, flagellin, with a recombinant hemagglutinin influenza-flagellin fusion vaccine (VAX125, STF2.HA1 SI). *Vaccine* **29**, 4897-4902, doi:10.1016/j.vaccine.2011.05.001 (2011).

158 Lee, S.-M., Joo, Y.-D. & Seo, S.-K. Expression and Function of TLR2 on CD4 Versus CD8 T Cells. *Immune network* **9**, 127-132, doi:10.4110/in.2009.9.4.127 (2009).

159 Cottalorda, A. *et al.* TLR2 engagement on memory CD8+ T cells improves their cytokine-mediated proliferation and IFN-γ secretion in the absence of Ag. *European Journal of Immunology* **39**, 2673-2681, doi:10.1002/eji.200939627 (2009).

160 Mercier, B. C., Cottalorda, A., Coupet, C.-A., Marvel, J. & Bonnefoy-Berard, N. TLR2 Engagement on CD8 T Cells Enables Generation of Functional Memory Cells in Response to a Suboptimal TCR Signal. *The Journal of Immunology* **182**, 1860-1867, doi:10.4049/jimmunol.0801167 (2009).

161 Caron, G. *et al.* Direct Stimulation of Human T Cells via TLR5 and TLR7/8: Flagellin and R-848 Up-Regulate Proliferation and IFN- Production by Memory CD4+ T Cells. *The Journal of Immunology* **175**, 1551-1557, doi:10.4049/jimmunol.175.3.1551 (2005).

162 Crellin, N. K. *et al.* Human CD4+ T cells express TLR5 and its ligand flagellin enhances the suppressive capacity and expression of FOXP3 in CD4+CD25+ T regulatory cells. *J. Immunol.* **175**, 8051-8059, doi:10.4049/jimmunol.175.12.8051 (2005).

163 Liu, H., Komai-Koma, M., Xu, D. & Liew, F. Y. Toll-like receptor 2 signaling modulates the functions of CD4+ CD25+ regulatory T cells. *Proc Natl Acad Sci U S A* **103**, 7048-7053, doi:10.1073/pnas.0601554103 (2006).

164 Reynolds, J. M. *et al.* Toll-like receptor 2 signaling in CD4(+) T lymphocytes promotes T helper 17 responses and regulates the pathogenesis of autoimmune disease. *Immunity* **32**, 692-702, doi:10.1016/j.immuni.2010.04.010 (2010).

165 Bendelac, A. & Medzhitov, R. Adjuvants of immunity: harnessing innate immunity to promote adaptive immunity. *J. Exp. Med.* **195**, F19-23, doi:10.1084/jem.20020073 (2002).

166 Coffman, R. L., Sher, A. & Seder, R. A. Vaccine adjuvants: putting innate immunity to work. *Immunity* **33**, 492-503, doi:10.1016/j.immuni.2010.10.002 (2010).

167 McKee, S. J. *et al.* Virus-like particles and alpha-galactosylceramide form a self-adjuvanting composite particle that elicits anti-tumor responses. *J. Control Release* **159**, 338-345, doi:10.1016/j.jconrel.2012.02.015 (2012).

168 Franco, D., Liu, W. M., Gardiner, D. F., Hahn, B. H. & Ho, D. D. CD40L-Containing Virus-Like Particle as a Candidate HIV-1 Vaccine Targeting Dendritic Cells. *Jaids-J Acq Imm Def* **56**, 393-400, doi:10.1097/QAI.0b013e31820b844e (2011).

169 Skountzou, I. *et al.* Incorporation of glycosylphosphatidylinositol-anchored granulocyte-macrophage colony-stimulating factor or CD40 ligand enhances immunogenicity of chimeric simian immunodeficiency virus-like particles. *Journal of virology* **81**, 1083-1094 (2007).

170 Kang, H. *et al.* Chimeric rabies virus-like particles containing membrane-anchored GM-CSF enhances the immune response against rabies virus. *Viruses* **7**, 1134-1152, doi:10.3390/v7031134 (2015).

171 Skountzou, I. *et al.* Incorporation of glycosylphosphatidylinositol-anchored granulocyte-macrophage colony-stimulating factor or CD40 ligand enhances immunogenicity of chimeric simian immunodeficiency virus-like particles. *J. Virol.* **81**, 1083-1094, doi:10.1128/JVI.01692-06 (2007).

172 Caton, A. J., Brownlee, G. G., Yewdell, J. W. & Gerhard, W. The antigenic structure of the influenza virus A/PR/8/34 hemagglutinin (H1 subtype). *Cell* **31**, 417-427, doi:10.1016/0092-8674(82)90135-0 (1982).

173 Liu, W., Zou, P., Ding, J., Lu, Y. & Chen, Y. H. Sequence comparison between the extracellular domain of M2 protein human and avian influenza A virus provides new information for bivalent influenza vaccine design. *Microbes Infect* **7**, 171-177, doi:10.1016/j.micinf.2004.10.006 (2005).

174 Black, R. A., Rota, P. A., Gorodkova, N., Klenk, H. D. & Kendal, A. P. Antibody response to the M2 protein of influenza A virus expressed in insect cells. *J Gen Virol* **74 (Pt 1)**, 143-146, doi:10.1099/0022-1317-74-1-143 (1993).

175 Deng, L., Cho, K. J., Fiers, W. & Saelens, X. M2e-Based Universal Influenza A Vaccines. *Vaccines* **3**, 105-136, doi:10.3390/vaccines3010105 (2015).

176 Jegerlehner, A., Schmitz, N., Storni, T. & Bachmann, M. F. Influenza A vaccine based on the extracellular domain of M2: weak protection mediated via antibody-dependent NK cell activity. *J Immunol* **172**, 5598-5605, doi:10.4049/jimmunol.172.9.5598 (2004).

177 Kang, S. M., Kim, M. C. & Compans, R. W. Virus-like particles as universal influenza vaccines. *Expert Rev Vaccines* **11**, 995-1007, doi:10.1586/erv.12.70 (2012).

178 Song, J. M. *et al.* Influenza virus-like particles containing M2 induce broadly cross protective immunity. *PLoS One* **6**, e14538, doi:10.1371/journal.pone.0014538 (2011).

179 Krammer, F. & Palese, P. Universal Influenza Virus Vaccines That Target the Conserved Hemagglutinin Stalk and Conserved Sites in the Head Domain. *J Infect Dis* **219**, S62-S67, doi:10.1093/infdis/jiy711 (2019).

180 Impagliazzo, A. *et al.* A stable trimeric influenza hemagglutinin stem as a broadly protective immunogen. *Science* **349**, 1301-1306, doi:10.1126/science.aac7263 (2015).

181 Yassine, H. M. *et al.* Hemagglutinin-stem nanoparticles generate heterosubtypic influenza protection. *Nat Med* **21**, 1065-1070, doi:10.1038/nm.3927 (2015).

182 Wrammert, J. *et al.* Broadly cross-reactive antibodies dominate the human B cell response against 2009 pandemic H1N1 influenza virus infection. *J Exp Med* **208**, 181-193, doi:10.1084/jem.20101352 (2011).

183 Li, G. M. *et al.* Pandemic H1N1 influenza vaccine induces a recall response in humans that favors broadly cross-reactive memory B cells. *Proc Natl Acad Sci U S A* **109**, 9047-9052, doi:10.1073/pnas.1118979109 (2012).

184 Bernstein, D. I. *et al.* Immunogenicity of chimeric haemagglutinin-based, universal influenza virus vaccine candidates: interim results of a randomised, placebo-controlled, phase 1 clinical trial. *Lancet Infect Dis* **20**, 80-91, doi:10.1016/S1473-3099(19)30393-7 (2020).

185 Lua, L. H. *et al.* Bioengineering virus-like particles as vaccines. *Biotechnol Bioeng* **111**, 425-440, doi:10.1002/bit.25159 (2014).

186 D'Aoust, M. A. *et al.* Influenza virus-like particles produced by transient expression in Nicotiana benthamiana induce a protective immune response against a lethal viral challenge in mice. *Plant Biotechnol J* **6**, 930-940, doi:10.1111/j.1467-7652.2008.00384.x (2008).

187 Wu, C. Y. *et al.* Mammalian expression of virus-like particles for advanced mimicry of authentic influenza virus. *PLoS One* **5**, e9784, doi:10.1371/journal.pone.0009784 (2010).

188 Hahn, T., Courban, D. & Hamer, M. Rapid manufacture and release of a GMP batch of avian influenza A (H7N9) virus-like particle vaccine made using recombinant baculovirus-Sf9 insect cell culture technology. *BioProcessing* **12** (2013).

189 Chen, B. J., Leser, G. P., Morita, E. & Lamb, R. A. Influenza virus hemagglutinin and neuraminidase, but not the matrix protein, are required for assembly and budding of plasmid-derived virus-like particles. *J Virol* **81**, 7111-7123, doi:10.1128/JVI.00361-07 (2007).

190 Kallolimath, S. *et al.* Engineering of complex protein sialylation in plants. *Proc Natl Acad Sci U S A* **113**, 9498-9503, doi:10.1073/pnas.1604371113 (2016).

191 Pushko, P. *et al.* Recombinant H1N1 virus-like particle vaccine elicits protective immunity in ferrets against the 2009 pandemic H1N1 influenza virus. *Vaccine* **28**, 4771-4776, doi:10.1016/j.vaccine.2010.04.093 (2010).

192 Zak, A. J. *et al.* Enhancing the Yield and Quality of Influenza Virus-like Particles (VLPs) Produced in Insect Cells by Inhibiting Cytopathic Effects of Matrix Protein M2. *ACS Synth Biol* **8**, 2303-2314, doi:10.1021/acssynbio.9b00111 (2019).

193 Nayak, D. P. *et al.* Biological and immunological properties of haemagglutinin and neuraminidase expressed from cloned cDNAs in prokaryotic and eukaryotic cells. *Vaccine* **3**, 165-171, doi:10.1016/0264-410x(85)90097-0 (1985).

194 Jabbar, M. A., Sivasubramanian, N. & Nayak, D. P. Influenza viral (A/WSN/33) hemagglutinin is expressed and glycosylated in the yeast Saccharomyces cerevisiae. *Proc Natl Acad Sci U S A* **82**, 2019-2023, doi:10.1073/pnas.82.7.2019 (1985).

195 Pietrzak, M. *et al.* An avian influenza H5N1 virus vaccine candidate based on the extracellular domain produced in yeast system as subviral particles protects chickens from lethal challenge. *Antiviral Res* **133**, 242-249, doi:10.1016/j.antiviral.2016.08.001 (2016).

196 Saelens, X. *et al.* Protection of mice against a lethal influenza virus challenge after immunization with yeast-derived secreted influenza virus hemagglutinin. *Eur J Biochem* **260**, 166-175, doi:10.1046/j.1432-1327.1999.00150.x (1999).

197 Nishioka, R., Satomura, A., Yamada, J., Kuroda, K. & Ueda, M. Rapid preparation of mutated influenza hemagglutinins for influenza virus pandemic prevention. *AMB Express* **6**, 8, doi:10.1186/s13568-016-0179-y (2016).

198 Wasilenko, J. L., Sarmento, L., Spatz, S. & Pantin-Jackwood, M. Cell surface display of highly pathogenic avian influenza virus hemagglutinin on the surface of Pichia pastoris cells using alpha-agglutinin for production of oral vaccines. *Biotechnol Prog* **26**, 542-547, doi:10.1002/btpr.343 (2010).

199 Athmaram, T. N. *et al.* Yeast expressed recombinant Hemagglutinin protein of novel H1N1 elicits neutralising antibodies in rabbits and mice. *Virol J* **8**, 524, doi:10.1186/1743-422X-8-524 (2011).

200 Lei, H., Jin, S., Karlsson, E., Schultz-Cherry, S. & Ye, K. Yeast Surface-Displayed H5N1 Avian Influenza Vaccines. *J Immunol Res* **2016**, 4131324, doi:10.1155/2016/4131324 (2016).

201 Wouters, O. J., McKee, M. & Luyten, J. Estimated Research and Development Investment Needed to Bring a New Medicine to Market, 2009-2018. *JAMA* **323**, 844-853, doi:10.1001/jama.2020.1166 (2020).

202 *CDC Seasonal Flu Vaccine Effectiveness Studies | CDC*, <https://www.cdc.gov/flu/vaccines-work/effectiveness-studies.htm> (2020).

203 Osterholm, M. T., Kelley, N. S., Sommer, A. & Belongia, E. A. Efficacy and effectiveness of influenza vaccines: a systematic review and meta-analysis. *Lancet Infect Dis* **12**, 36-44, doi:10.1016/S1473-3099(11)70295-X (2012).

204 Pop-Vicas, A. & Gravenstein, S. Influenza in the elderly: a mini-review. *Gerontology* **57**, 397-404, doi:10.1159/000319033 (2011).

205 Kirnbauer, R., Booy, F., Cheng, N., Lowy, D. R. & Schiller, J. T. Papillomavirus L1 major capsid protein self-assembles into virus-like particles that are highly immunogenic. *Proc Natl Acad Sci U S A* **89**, 12180-12184, doi:10.1073/pnas.89.24.12180 (1992).

206 Hilleman, M. R. Yeast recombinant hepatitis B vaccine. *Infection* **15**, 3-7, doi:10.1007/BF01646107 (1987).

207 Roldao, A., Mellado, M. C., Castilho, L. R., Carrondo, M. J. & Alves, P. M. Virus-like particles in vaccine development. *Expert Rev Vaccines* **9**, 1149-1176, doi:10.1586/erv.10.115 (2010).

208 Liu, F., Wu, X., Li, L., Liu, Z. & Wang, Z. Use of baculovirus expression system for generation of virus-like particles: successes and challenges. *Protein Expr Purif* **90**, 104-116, doi:10.1016/j.pep.2013.05.009 (2013).

209 Daniels, R., Kurowski, B., Johnson, A. E. & Hebert, D. N. N-linked glycans direct the cotranslational folding pathway of influenza hemagglutinin. *Mol Cell* **11**, 79-90, doi:10.1016/s1097-2765(02)00821-3 (2003).

210 Wagner, R., Heuer, D., Wolff, T., Herwig, A. & Klenk, H. D. N-Glycans attached to the stem domain of haemagglutinin efficiently regulate influenza A virus replication. *J Gen Virol* **83**, 601-609, doi:10.1099/0022-1317-83-3-601 (2002).

211 Roberts, P. C., Garten, W. & Klenk, H. D. Role of conserved glycosylation sites in maturation and transport of influenza A virus hemagglutinin. *J Virol* **67**, 3048-3060, doi:10.1128/JVI.67.6.3048-3060.1993 (1993).

212 Maley, F., Trimble, R. B., Tarentino, A. L. & Plummer, T. H., Jr. Characterization of glycoproteins and their associated oligosaccharides through the use of endoglycosidases. *Anal Biochem* **180**, 195-204, doi:10.1016/0003-2697(89)90115-2 (1989).

213 Hamilton, S. R. *et al.* Humanization of yeast to produce complex terminally sialylated glycoproteins. *Science* **313**, 1441-1443, doi:10.1126/science.1130256 (2006).

214 Kim, H., Yoo, S. J. & Kang, H. A. Yeast synthetic biology for the production of recombinant therapeutic proteins. *FEMS Yeast Res* **15**, 1-16, doi:10.1111/1567-1364.12195 (2015).

215 Copeland, C. S., Doms, R. W., Bolzau, E. M., Webster, R. G. & Helenius, A. Assembly of influenza hemagglutinin trimers and its role in intracellular transport. *J Cell Biol* **103**, 1179-1191, doi:10.1083/jcb.103.4.1179 (1986).

216 Galloway, S. E., Reed, M. L., Russell, C. J. & Steinhauer, D. A. Influenza HA subtypes demonstrate divergent phenotypes for cleavage activation and pH of fusion: implications for host range and adaptation. *PLoS Pathog* **9**, e1003151, doi:10.1371/journal.ppat.1003151 (2013).

217 Sakuragi, S., Goto, T., Sano, K. & Morikawa, Y. HIV type 1 Gag virus-like particle budding from spheroplasts of Saccharomyces cerevisiae. *Proc Natl Acad Sci U S A* **99**, 7956-7961, doi:10.1073/pnas.082281199 (2002).

218 Matlin, K. S., Skibbens, J. & McNeil, P. L. Reduced extracellular pH reversibly inhibits oligomerization, intracellular transport, and processing of the influenza hemagglutinin in infected Madin-Darby canine kidney cells. *J Biol Chem* **263**, 11478-11485 (1988).

219 Chlanda, P. *et al.* Structural Analysis of the Roles of Influenza A Virus Membrane-Associated Proteins in Assembly and Morphology. *J Virol* **89**, 8957-8966, doi:10.1128/JVI.00592-15 (2015).

220 Tsutsui, H., Karasawa, S., Okamura, Y. & Miyawaki, A. Improving membrane voltage measurements using FRET with new fluorescent proteins. *Nat Methods* **5**, 683-685, doi:10.1038/nmeth.1235 (2008).

221 Kaishima, M., Ishii, J., Matsuno, T., Fukuda, N. & Kondo, A. Expression of varied GFPs in Saccharomyces cerevisiae: codon optimization yields stronger than expected expression and fluorescence intensity. *Sci Rep* **6**, 35932, doi:10.1038/srep35932 (2016).

222 Zinkeviciute, R. *et al.* Heat shock at higher cell densities improves measles hemagglutinin translocation and human GRP78/BiP secretion in Saccharomyces cerevisiae. *N Biotechnol* **32**, 690-700, doi:10.1016/j.nbt.2015.04.001 (2015).

223 Ciplys, E., Sasnauskas, K. & Slibinskas, R. Overexpression of human calnexin in yeast improves measles surface glycoprotein solubility. *FEMS Yeast Res* **11**, 514-523, doi:10.1111/j.1567-1364.2011.00742.x (2011).

224 Ciplys, E., Samuel, D., Juozapaitis, M., Sasnauskas, K. & Slibinskas, R. Overexpression of human virus surface glycoprotein precursors induces cytosolic unfolded protein response in Saccharomyces cerevisiae. *Microb Cell Fact* **10**, 37, doi:10.1186/1475-2859-10-37 (2011).

225 Schultz, L. D. *et al.* Expression and secretion in yeast of a 400-kDa envelope glycoprotein derived from Epstein-Barr virus. *Gene* **54**, 113-123, doi:10.1016/0378-1119(87)90353-2 (1987).

226 Drew, D. & Kim, H. Optimizing Saccharomyces cerevisiae induction regimes. *Methods Mol Biol* **866**, 191-195, doi:10.1007/978-1-61779-770-5_16 (2012).

227 Abdul Jabbar, M. & Nayak, D. P. Signal processing, glycosylation, and secretion of mutant hemagglutinins of a human influenza virus by Saccharomyces cerevisiae. *Mol Cell Biol* **7**, 1476-1485, doi:10.1128/mcb.7.4.1476 (1987).

228 Costa, S., Almeida, A., Castro, A. & Domingues, L. Fusion tags for protein solubility, purification and immunogenicity in Escherichia coli: the novel Fh8 system. *Front Microbiol* **5**, 63, doi:10.3389/fmicb.2014.00063 (2014).

229 Dalken, B., Jabulowsky, R. A., Oberoi, P., Benhar, I. & Wels, W. S. Maltose-binding protein enhances secretion of recombinant human granzyme B accompanied by in vivo processing of a precursor MBP fusion protein. *PLoS One* **5**, e14404, doi:10.1371/journal.pone.0014404 (2010).

230 Filipe, V., Hawe, A. & Jiskoot, W. Critical evaluation of Nanoparticle Tracking Analysis (NTA) by NanoSight for the measurement of nanoparticles and protein aggregates. *Pharm Res* **27**, 796-810, doi:10.1007/s11095-010-0073-2 (2010).

231 Shao, Z., Zhao, H. & Zhao, H. DNA assembler, an in vivo genetic method for rapid construction of biochemical pathways. *Nucleic Acids Res* **37**, e16, doi:10.1093/nar/gkn991 (2009).

232 Hatziioannou, T., Delahaye, E., Martin, F., Russell, S. J. & Cosset, F. L. Retroviral display of functional binding domains fused to the amino terminus of influenza hemagglutinin. *Hum Gene Ther* **10**, 1533-1544, doi:10.1089/10430349950017860 (1999).

233 Nielsen, J. & Jewett, M. C. Impact of systems biology on metabolic engineering of Saccharomyces cerevisiae. *FEMS Yeast Res* **8**, 122-131, doi:10.1111/j.1567-1364.2007.00302.x (2008).

234 Hong, K. K. & Nielsen, J. Metabolic engineering of Saccharomyces cerevisiae: a key cell factory platform for future biorefineries. *Cell Mol Life Sci* **69**, 2671-2690, doi:10.1007/s00018-012-0945-1 (2012).

235 Sun, J. *et al.* Cloning and characterization of a panel of constitutive promoters for applications in pathway engineering in Saccharomyces cerevisiae. *Biotechnol Bioeng* **109**, 2082-2092, doi:10.1002/bit.24481 (2012).

236 Tan, S. Z., Manchester, S. & Prather, K. L. Controlling Central Carbon Metabolism for Improved Pathway Yields in Saccharomyces cerevisiae. *ACS Synth Biol* **5**, 116-124, doi:10.1021/acssynbio.5b00164 (2016).

237 Bugada, L. F., Smith, M. R. & Wen, F. Engineering Spatially Organized Multienzyme Assemblies for Complex Chemical Transformation. *Acs Catalysis* **8**, 7898-7906, doi:10.1021/acscatal.8b01883 (2018).

238 Li, Y. *et al.* Complete biosynthesis of noscapine and halogenated alkaloids in yeast. *Proc Natl Acad Sci U S A* **115**, E3922-E3931, doi:10.1073/pnas.1721469115 (2018).

239 Lu, C. & Jeffries, T. Shuffling of promoters for multiple genes to optimize xylose fermentation in an engineered Saccharomyces cerevisiae strain. *Appl Environ Microbiol* **73**, 6072-6077, doi:10.1128/AEM.00955-07 (2007).

240 Begley, T. P., Wen, F., McLachlan, M. & Zhao, H. in *Wiley Encyclopedia of Chemical Biology* 1-10 (John Wiley & Sons, Inc., Hoboken, NJ, USA, 2008).

241 Wang, H. H. *et al.* Programming cells by multiplex genome engineering and accelerated evolution. *Nature* **460**, 894-898, doi:10.1038/nature08187 (2009).

242 Du, J., Yuan, Y., Si, T., Lian, J. & Zhao, H. Customized optimization of metabolic pathways by combinatorial transcriptional engineering. *Nucleic Acids Res* **40**, e142, doi:10.1093/nar/gks549 (2012).

243 Si, T. *et al.* Automated multiplex genome-scale engineering in yeast. *Nat Commun* **8**, 15187, doi:10.1038/ncomms15187 (2017).

244 Zhou, S. H. & Alper, H. S. Strategies for directed and adapted evolution as part of microbial strain engineering. *Journal of Chemical Technology and Biotechnology* **94**, 366-376, doi:10.1002/jctb.5746 (2019).

245 Boder, E. T. & Wittrup, K. D. Yeast surface display for directed evolution of protein expression, affinity, and stability. *Methods Enzymol* **328**, 430-444, doi:10.1016/s0076-6879(00)28410-3 (2000).

246 Smith, M. R., Khera, E. & Wen, F. Engineering Novel and Improved Biocatalysts by Cell Surface Display. *Ind Eng Chem Res* **54**, 4021-4032, doi:10.1021/ie504071f (2015).

247 Smith, M. R. *et al.* Elucidating structure-performance relationships in whole-cell cooperative enzyme catalysis. *Nature Catalysis* **2**, 809-819, doi:10.1038/s41929-019-0321-8 (2019).

248 Wen, F., Nair, N. U. & Zhao, H. Protein engineering in designing tailored enzymes and microorganisms for biofuels production. *Curr Opin Biotechnol* **20**, 412-419, doi:10.1016/j.copbio.2009.07.001 (2009).

249 Crivat, G. & Taraska, J. W. Imaging proteins inside cells with fluorescent tags. *Trends Biotechnol* **30**, 8-16, doi:10.1016/j.tibtech.2011.08.002 (2012).

250 Chudakov, D. M., Matz, M. V., Lukyanov, S. & Lukyanov, K. A. Fluorescent proteins and their applications in imaging living cells and tissues. *Physiol Rev* **90**, 1103-1163, doi:10.1152/physrev.00038.2009 (2010).

251 Los, G. V. & Wood, K. The HaloTag: a novel technology for cell imaging and protein analysis. *Methods Mol Biol* **356**, 195-208, doi:10.1385/1-59745-217-3:195 (2007).

252 Blackstock, D. & Chen, W. Halo-tag mediated self-labeling of fluorescent proteins to molecular beacons for nucleic acid detection. *Chem Commun (Camb)* **50**, 13735-13738, doi:10.1039/c4cc07118b (2014).

253 Juillerat, A. *et al.* Directed evolution of O6-alkylguanine-DNA alkyltransferase for efficient labeling of fusion proteins with small molecules in vivo. *Chem Biol* **10**, 313-317, doi:10.1016/s1074-5521(03)00068-1 (2003).

254 Gautier, A. *et al.* An engineered protein tag for multiprotein labeling in living cells. *Chem Biol* **15**, 128-136, doi:10.1016/j.chembiol.2008.01.007 (2008).

255 Jensen, E. C. Use of fluorescent probes: their effect on cell biology and limitations. *Anat Rec (Hoboken)* **295**, 2031-2036, doi:10.1002/ar.22602 (2012).

256 Snapp, E. Design and use of fluorescent fusion proteins in cell biology. *Curr Protoc Cell Biol* **Chapter 21**, 21 24 21-21 24 13, doi:10.1002/0471143030.cb2104s27 (2005).

257 Baens, M. *et al.* The dark side of EGFP: defective polyubiquitination. *PLoS One* **1**, e54, doi:10.1371/journal.pone.0000054 (2006).

258 Margolin, W. The price of tags in protein localization studies. *J Bacteriol* **194**, 6369-6371, doi:10.1128/JB.01640-12 (2012).

259 Swulius, M. T. & Jensen, G. J. The helical MreB cytoskeleton in Escherichia coli MC1000/pLE7 is an artifact of the N-Terminal yellow fluorescent protein tag. *J Bacteriol* **194**, 6382-6386, doi:10.1128/JB.00505-12 (2012).

260 Heo, M. *et al.* Impact of fluorescent protein fusions on the bacterial flagellar motor. *Sci Rep* **7**, 12583, doi:10.1038/s41598-017-11241-w (2017).

261 Wu, C. F., Cha, H. J., Rao, G., Valdes, J. J. & Bentley, W. E. A green fluorescent protein fusion strategy for monitoring the expression, cellular location, and separation of biologically active organophosphorus hydrolase. *Appl Microbiol Biotechnol* **54**, 78-83, doi:10.1007/s002539900286 (2000).

262 Cha, H. J., Wu, C. F., Valdes, J. J., Rao, G. & Bentley, W. E. Observations of green fluorescent protein as a fusion partner in genetically engineered Escherichia coli: Monitoring protein expression and solubility. *Biotechnology and Bioengineering* **67**, 565-574, doi:10.1002/(Sici)1097-0290(20000305)67:5<565::Aid-Bit7>3.0.Co;2-P (2000).

263 Griffin, B. A., Adams, S. R. & Tsien, R. Y. Specific covalent labeling of recombinant protein molecules inside live cells. *Science* **281**, 269-272, doi:10.1126/science.281.5374.269 (1998).

264 Adams, S. R. *et al.* New biarsenical ligands and tetracysteine motifs for protein labeling in vitro and in vivo: synthesis and biological applications. *J Am Chem Soc* **124**, 6063-6076, doi:10.1021/ja017687n (2002).

265 Enninga, J., Mounier, J., Sansonetti, P. & Tran Van Nhieu, G. Secretion of type III effectors into host cells in real time. *Nat Methods* **2**, 959-965, doi:10.1038/nmeth804 (2005).

266 Dyachok, O., Isakov, Y., Sagetorp, J. & Tengholm, A. Oscillations of cyclic AMP in hormone-stimulated insulin-secreting beta-cells. *Nature* **439**, 349-352, doi:10.1038/nature04410 (2006).

267 Hoffmann, C. *et al.* A FlAsH-based FRET approach to determine G protein-coupled receptor activation in living cells. *Nat Methods* **2**, 171-176, doi:10.1038/nmeth742 (2005).

268 Zurn, A. *et al.* Site-specific, orthogonal labeling of proteins in intact cells with two small biarsenical fluorophores. *Bioconjug Chem* **21**, 853-859, doi:10.1021/bc900394j (2010).

269 Hoffmann, C. *et al.* Fluorescent labeling of tetracysteine-tagged proteins in intact cells. *Nat Protoc* **5**, 1666-1677, doi:10.1038/nprot.2010.129 (2010).

270 Machleidt, T., Robers, M. & Hanson, G. T. Protein labeling with FlAsH and ReAsH. *Methods Mol Biol* **356**, 209-220, doi:10.1385/1-59745-217-3:209 (2007).

271 Cheng, Q., Ruebling-Jass, K., Zhang, J., Chen, Q. & Croker, K. M. Use FACS sorting in metabolic engineering of Escherichia coli for increased peptide production. *Methods Mol Biol* **834**, 177-196, doi:10.1007/978-1-61779-483-4_12 (2012).

272 Zordan, R. E., Beliveau, B. J., Trow, J. A., Craig, N. L. & Cormack, B. P. Avoiding the ends: internal epitope tagging of proteins using transposon Tn7. *Genetics* **200**, 47-58, doi:10.1534/genetics.114.169482 (2015).

273 De Nobel, J. G. & Barnett, J. A. Passage of molecules through yeast cell walls: a brief essay-review. *Yeast* **7**, 313-323, doi:10.1002/yea.320070402 (1991).

274 Kiseleva, E. *et al.* A protocol for isolation and visualization of yeast nuclei by scanning electron microscopy (SEM). *Nat Protoc* **2**, 1943-1953, doi:10.1038/nprot.2007.251 (2007).

275 Ovalle, R. *et al.* A spheroplast rate assay for determination of cell wall integrity in yeast. *Yeast* **14**, 1159-1166, doi:10.1002/(SICI)1097-0061(19980930)14:13<1159::AID-YEA317>3.0.CO;2-3 (1998).

276 Ovalle, R., Spencer, M., Thiwanont, M. & Lipke, P. N. The spheroplast lysis assay for yeast in microtiter plate format. *Appl Environ Microbiol* **65**, 3325-3327, doi:10.1128/AEM.65.8.3325-3327.1999 (1999).

277 Niu, W., Hart, G. T. & Marcotte, E. M. High-throughput immunofluorescence microscopy using yeast spheroplast cell-based microarrays. *Methods Mol Biol* **706**, 83-95, doi:10.1007/978-1-61737-970-3_7 (2011).

278 Aguilar-Uscanga, B. & Francois, J. M. A study of the yeast cell wall composition and structure in response to growth conditions and mode of cultivation. *Lett Appl Microbiol* **37**, 268-274, doi:10.1046/j.1472-765x.2003.01394.x (2003).

279 Dominguez, R. & Holmes, K. C. Actin structure and function. *Annu Rev Biophys* **40**, 169-186, doi:10.1146/annurev-biophys-042910-155359 (2011).

280 Baschong, W., Suetterlin, R. & Laeng, R. H. Control of autofluorescence of archival formaldehyde-fixed, paraffin-embedded tissue in confocal laser scanning microscopy (CLSM). *J Histochem Cytochem* **49**, 1565-1572, doi:10.1177/002215540104901210 (2001).

281 Moyses, D. N., Reis, V. C., de Almeida, J. R., de Moraes, L. M. & Torres, F. A. Xylose Fermentation by Saccharomyces cerevisiae: Challenges and Prospects. *Int J Mol Sci* **17**, 207, doi:10.3390/ijms17030207 (2016).

282 Kwak, S. & Jin, Y. S. Production of fuels and chemicals from xylose by engineered Saccharomyces cerevisiae: a review and perspective. *Microb Cell Fact* **16**, 82, doi:10.1186/s12934-017-0694-9 (2017).

283 Gao, M., Ploessl, D. & Shao, Z. Enhancing the Co-utilization of Biomass-Derived Mixed Sugars by Yeasts. *Front Microbiol* **9**, 3264, doi:10.3389/fmicb.2018.03264 (2018).

284 Futcher, B. & Carbon, J. Toxic effects of excess cloned centromeres. *Mol Cell Biol* **6**, 2213-2222, doi:10.1128/mcb.6.6.2213 (1986).

285 Karim, A. S., Curran, K. A. & Alper, H. S. Characterization of plasmid burden and copy number in Saccharomyces cerevisiae for optimization of metabolic engineering applications. *FEMS Yeast Res* **13**, 107-116, doi:10.1111/1567-1364.12016 (2013).

286 Ni, H., Laplaza, J. M. & Jeffries, T. W. Transposon mutagenesis to improve the growth of recombinant Saccharomyces cerevisiae on D-xylose. *Appl Environ Microbiol* **73**, 2061-2066, doi:10.1128/AEM.02564-06 (2007).

287 Van Vleet, J. H., Jeffries, T. W. & Olsson, L. Deleting the para-nitrophenyl phosphatase (pNPPase), PHO13, in recombinant Saccharomyces cerevisiae improves growth and ethanol production on D-xylose. *Metab Eng* **10**, 360-369, doi:10.1016/j.ymben.2007.12.002 (2008).

288 Pival, S. L., Birner-Gruenberger, R., Krump, C. & Nidetzky, B. D-Xylulose kinase from Saccharomyces cerevisiae: isolation and characterization of the highly unstable enzyme, recombinantly produced in Escherichia coli. *Protein Expr Purif* **79**, 223-230, doi:10.1016/j.pep.2011.05.018 (2011).

289 Eliasson, A., Hofmeyr, J. H. S., Pedler, S. & Hahn-Hagerdal, B. The xylose reductase/xylitol dehydrogenase/xylulokinase ratio affects product formation in recombinant xylose-utilising Saccharomyces cerevisiae. *Enzyme and microbial technology* **29**, 288-297, doi:Doi 10.1016/S0141-0229(01)00386-6 (2001).

290 Kim, S. R., Ha, S. J., Kong, II & Jin, Y. S. High expression of XYL2 coding for xylitol dehydrogenase is necessary for efficient xylose fermentation by engineered Saccharomyces cerevisiae. *Metab Eng* **14**, 336-343, doi:10.1016/j.ymben.2012.04.001 (2012).

291 Wang, X., Wang, Z. & Da Silva, N. A. G418 Selection and stability of cloned genes integrated at chromosomal δ sequences of Saccharomyces cerevisiae. *Biotechnology and Bioengineering* **49**, 45-51, doi:10.1002/(sici)1097-0290(19960105)49:1<45::Aid-bit6>3.0.Co;2-t (2000).

292 O'Malley, M. A., Lazarova, T., Britton, Z. T. & Robinson, A. S. High-level expression in Saccharomyces cerevisiae enables isolation and spectroscopic characterization of functional human adenosine A2a receptor. *J Struct Biol* **159**, 166-178, doi:10.1016/j.jsb.2007.05.001 (2007).

293 Routledge, S. J. *et al.* The synthesis of recombinant membrane proteins in yeast for structural studies. *Methods* **95**, 26-37, doi:10.1016/j.ymeth.2015.09.027 (2016).

294 Bulter, T. *et al.* Functional expression of a fungal laccase in Saccharomyces cerevisiae by directed evolution. *Appl Environ Microbiol* **69**, 987-995, doi:10.1128/aem.69.2.987-995.2003 (2003).

295 Johannes, T. W., Woodyer, R. D. & Zhao, H. Directed evolution of a thermostable phosphite dehydrogenase for NAD(P)H regeneration. *Appl Environ Microbiol* **71**, 5728-5734, doi:10.1128/AEM.71.10.5728-5734.2005 (2005).

296 Doan, M. *et al.* Diagnostic Potential of Imaging Flow Cytometry. *Trends Biotechnol* **36**, 649-652, doi:10.1016/j.tibtech.2017.12.008 (2018).

297 DiCarlo, J. E. *et al.* Genome engineering in Saccharomyces cerevisiae using CRISPR-Cas systems. *Nucleic Acids Res* **41**, 4336-4343, doi:10.1093/nar/gkt135 (2013).

298 Billi, A. C. *et al.* The female-biased factor VGLL3 drives cutaneous and systemic autoimmunity. *JCI Insight* **4**, e127291, doi:10.1172/jci.insight.127291 (2019).

299 Smith, M. R., Bugada, L. F. & Wen, F. Rapid microsphere-assisted peptide screening (MAPS) of promiscuous MHCII-binding peptides in Zika virus envelope protein. *AIChE Journal* **66**, e16697, doi:10.1002/aic.16697 (2019).

300 Levitt, D. & King, M. Methanol fixation permits flow cytometric analysis of immunofluorescent stained intracellular antigens. *J Immunol Methods* **96**, 233-237, doi:10.1016/0022-1759(87)90319-x (1987).

301 Jensen, U. B., Owens, D. M., Pedersen, S. & Christensen, R. Zinc fixation preserves flow cytometry scatter and fluorescence parameters and allows simultaneous analysis of DNA content and synthesis, and intracellular and surface epitopes. *Cytometry A* **77**, 798-804, doi:10.1002/cyto.a.20914 (2010).

302 Schmittgen, T. D. & Livak, K. J. Analyzing real-time PCR data by the comparative C(T) method. *Nat Protoc* **3**, 1101-1108, doi:10.1038/nprot.2008.73 (2008).

303 Shamanna, D. K. & Sanderson, K. E. Uptake and catabolism of D-xylose in Salmonella typhimurium LT2. *J Bacteriol* **139**, 64-70, doi:10.1128/JB.139.1.64-70.1979 (1979).

304 Eliasson, A., Christensson, C., Wahlbom, C. F. & Hahn-Hagerdal, B. Anaerobic xylose fermentation by recombinant Saccharomyces cerevisiae carrying XYL1, XYL2, and XKS1 in mineral medium chemostat cultures. *Appl Environ Microbiol* **66**, 3381-3386, doi:10.1128/aem.66.8.3381-3386.2000 (2000).

305 Sekar, R., Shin, H. D. & DiChristina, T. J. Activation of an Otherwise Silent Xylose Metabolic Pathway in Shewanella oneidensis. *Appl Environ Microbiol* **82**, 3996-4005, doi:10.1128/AEM.00881-16 (2016).

306 Yamada, R. *et al.* Cocktail delta-integration: a novel method to construct cellulolytic enzyme expression ratio-optimized yeast strains. *Microb Cell Fact* **9**, 32, doi:10.1186/1475-2859-9-32 (2010).

307 Memoli, M. J. *et al.* Influenza A Reinfection in Sequential Human Challenge: Implications for Protective Immunity and "Universal" Vaccine Development. *Clin Infect Dis* **70**, 748-753, doi:10.1093/cid/ciz281 (2020).

308 Su, S. *et al.* Epidemiology, Genetic Recombination, and Pathogenesis of Coronaviruses. *Trends Microbiol* **24**, 490-502, doi:10.1016/j.tim.2016.03.003 (2016).

309 Callow, K. A., Parry, H. F., Sergeant, M. & Tyrrell, D. A. The time course of the immune response to experimental coronavirus infection of man. *Epidemiol Infect* **105**, 435-446, doi:10.1017/s0950268800048019 (1990).

310 Holmes, K. V. SARS coronavirus: a new challenge for prevention and therapy. *J Clin Invest* **111**, 1605-1609, doi:10.1172/JCI18819 (2003).

311 Pulendran, B. Systems vaccinology: probing humanity's diverse immune systems with vaccines. *Proc Natl Acad Sci U S A* **111**, 12300-12306, doi:10.1073/pnas.1400476111 (2014).

312 Querec, T. D. *et al.* Systems biology approach predicts immunogenicity of the yellow fever vaccine in humans. *Nat Immunol* **10**, 116-125, doi:10.1038/ni.1688 (2009).

313 Nakaya, H. I. *et al.* Systems biology of vaccination for seasonal influenza in humans. *Nat Immunol* **12**, 786-795, doi:10.1038/ni.2067 (2011).

314 Gaucher, D. *et al.* Yellow fever vaccine induces integrated multilineage and polyfunctional immune responses. *J Exp Med* **205**, 3119-3131, doi:10.1084/jem.20082292 (2008).

315 Bendall, S. C., Nolan, G. P., Roederer, M. & Chattopadhyay, P. K. A deep profiler's guide to cytometry. *Trends Immunol* **33**, 323-332, doi:10.1016/j.it.2012.02.010 (2012).

316 Bandura, D. R. *et al.* Mass cytometry: technique for real time single cell multitarget immunoassay based on inductively coupled plasma time-of-flight mass spectrometry. *Anal Chem* **81**, 6813-6822, doi:10.1021/ac901049w (2009).

317 Chevrier, S. *et al.* Compensation of Signal Spillover in Suspension and Imaging Mass Cytometry. *Cell Syst* **6**, 612-620 e615, doi:10.1016/j.cels.2018.02.010 (2018).

318 Levine, J. H. *et al.* Data-Driven Phenotypic Dissection of AML Reveals Progenitor-like Cells that Correlate with Prognosis. *Cell* **162**, 184-197, doi:10.1016/j.cell.2015.05.047 (2015).

319 Qiu, P. *et al.* Extracting a cellular hierarchy from high-dimensional cytometry data with SPADE. *Nat Biotechnol* **29**, 886-891, doi:10.1038/nbt.1991 (2011).

320 Bruggner, R. V., Bodenmiller, B., Dill, D. L., Tibshirani, R. J. & Nolan, G. P. Automated identification of stratifying signatures in cellular subpopulations. *Proc Natl Acad Sci U S A* **111**, E2770-2777, doi:10.1073/pnas.1408792111 (2014).

321 Vapnik, V., Golowich, S. E. & Smola, A. Support vector method for function approximation, regression estimation, and signal processing. *Advances in Neural Information Processing Systems 9* **9**, 281-287 (1997).

322 Amir el, A. D. *et al.* viSNE enables visualization of high dimensional single-cell data and reveals phenotypic heterogeneity of leukemia. *Nat Biotechnol* **31**, 545-552, doi:10.1038/nbt.2594 (2013).

323 Geissmann, F. *et al.* Development of monocytes, macrophages, and dendritic cells. *Science* **327**, 656-661, doi:10.1126/science.1178331 (2010).

324 Chen, X. *et al.* Host Immune Response to Influenza A Virus Infection. *Front Immunol* **9**, 320, doi:10.3389/fimmu.2018.00320 (2018).

325 Rojas, J. M., Avia, M., Martin, V. & Sevilla, N. IL-10: A Multifunctional Cytokine in Viral Infections. *J Immunol Res* **2017**, 6104054, doi:10.1155/2017/6104054 (2017).

326 Boivin, W. A., Cooper, D. M., Hiebert, P. R. & Granville, D. J. Intracellular versus extracellular granzyme B in immunity and disease: challenging the dogma. *Lab Invest* **89**, 1195-1220, doi:10.1038/labinvest.2009.91 (2009).

327 Luzina, I. G. *et al.* Regulation of inflammation by interleukin-4: a review of "alternatives". *J Leukoc Biol* **92**, 753-764, doi:10.1189/jlb.0412214 (2012).

328 Sun, J., Madan, R., Karp, C. L. & Braciale, T. J. Effector T cells control lung inflammation during acute influenza virus infection by producing IL-10. *Nat Med* **15**, 277-284, doi:10.1038/nm.1929 (2009).

329 Bahadoran, A. *et al.* Immune Responses to Influenza Virus and Its Correlation to Age and Inherited Factors. *Front Microbiol* **7**, 1841, doi:10.3389/fmicb.2016.01841 (2016).

330 Steuerman, Y. *et al.* Dissection of Influenza Infection In Vivo by Single-Cell RNA Sequencing. *Cell Syst* **6**, 679-691 e674, doi:10.1016/j.cels.2018.05.008 (2018).

331 Manicassamy, B. *et al.* Analysis of in vivo dynamics of influenza virus infection in mice using a GFP reporter virus. *Proc Natl Acad Sci U S A* **107**, 11531-11536, doi:10.1073/pnas.0914994107 (2010).

332 Perez-Caballero, D. *et al.* Tetherin inhibits HIV-1 release by directly tethering virions to cells. *Cell* **139**, 499-511, doi:10.1016/j.cell.2009.08.039 (2009).

333 Wong, C. K. *et al.* Aging Impairs Alveolar Macrophage Phagocytosis and Increases Influenza-Induced Mortality in Mice. *J Immunol* **199**, 1060-1068, doi:10.4049/jimmunol.1700397 (2017).

334 Hufford, M. M., Kim, T. S., Sun, J. & Braciale, T. J. The effector T cell response to influenza infection. *Curr Top Microbiol Immunol* **386**, 423-455, doi:10.1007/82_2014_397 (2015).

335 Franceschi, C., Garagnani, P., Parini, P., Giuliani, C. & Santoro, A. Inflammaging: a new immune-metabolic viewpoint for age-related diseases. *Nat Rev Endocrinol* **14**, 576-590, doi:10.1038/s41574-018-0059-4 (2018).

336 Lu, Y. *et al.* The interaction of influenza H5N1 viral hemagglutinin with sialic acid receptors leads to the activation of human gammadelta T cells. *Cell Mol Immunol* **10**, 463-470, doi:10.1038/cmi.2013.26 (2013).

337 Brandes, M., Willimann, K. & Moser, B. Professional antigen-presentation function by human gammadelta T Cells. *Science* **309**, 264-268, doi:10.1126/science.1110267 (2005).

338 Qin, G. *et al.* Type 1 responses of human Vgamma9Vdelta2 T cells to influenza A viruses. *J Virol* **85**, 10109-10116, doi:10.1128/JVI.05341-11 (2011).

339 Dong, P. *et al.* gammadelta T Cells Provide Protective Function in Highly Pathogenic Avian H5N1 Influenza A Virus Infection. *Front Immunol* **9**, 2812, doi:10.3389/fimmu.2018.02812 (2018).

340 Goldberg, E. L. *et al.* Ketogenic diet activates protective gammadelta T cell responses against influenza virus infection. *Sci Immunol* **4**, doi:10.1126/sciimmunol.aav2026 (2019).

341 Samarasinghe, A. E. *et al.* Eosinophils Promote Antiviral Immunity in Mice Infected with Influenza A Virus. *J Immunol* **198**, 3214-3226, doi:10.4049/jimmunol.1600787 (2017).

342 Rosenberg, H. F., Dyer, K. D. & Domachowske, J. B. Eosinophils and their interactions with respiratory virus pathogens. *Immunol Res* **43**, 128-137, doi:10.1007/s12026-008-8058-5 (2009).

343 LeMessurier, K. S. *et al.* Influenza A virus directly modulates mouse eosinophil responses. *J Leukoc Biol* **108**, 151-168, doi:10.1002/JLB.4MA0320-343R (2020).

344 Garcia-Sastre, A. *et al.* Influenza A virus lacking the NS1 gene replicates in interferon-deficient systems. *Virology* **252**, 324-330, doi:10.1006/viro.1998.9508 (1998).

345 Council, N. R. in *Guide for the Care and Use of Laboratory Animals The National Academies Collection: Reports funded by National Institutes of Health* (ed th) (2011).

346 Veit, M. & Thaa, B. Association of influenza virus proteins with membrane rafts. *Adv Virol* **2011**, 370606, doi:10.1155/2011/370606 (2011).

347 Fantini, J., Di Scala, C., Evans, L. S., Williamson, P. T. & Barrantes, F. J. A mirror code for protein-cholesterol interactions in the two leaflets of biological membranes. *Sci Rep* **6**, 21907, doi:10.1038/srep21907 (2016).

348 Boesze-Battaglia, K. *et al.* Cytolethal distending toxin-induced cell cycle arrest of lymphocytes is dependent upon recognition and binding to cholesterol. *J Biol Chem* **284**, 10650-10658, doi:10.1074/jbc.M809094200 (2009).

349 Christian, A. E., Haynes, M. P., Phillips, M. C. & Rothblat, G. H. Use of cyclodextrins for manipulating cellular cholesterol content. *J Lipid Res* **38**, 2264-2272, doi:10.1073/pnas.1202810109 (1997).

350 Souza, C. M. *et al.* A stable yeast strain efficiently producing cholesterol instead of ergosterol is functional for tryptophan uptake, but not weak organic acid resistance. *Metab Eng* **13**, 555-569, doi:10.1016/j.ymben.2011.06.006 (2011).

351 Sareneva, H. & Makarow, M. Membrane biology in yeast as probed with enveloped viruses. *Subcell Biochem* **15**, 367-404, doi:10.1007/978-1-4899-1675-4_11 (1989).

352 Gluck, R. *et al.* Immunopotentiating reconstituted influenza virus virosome vaccine delivery system for immunization against hepatitis A. *J Clin Invest* **90**, 2491-2495, doi:10.1172/JCI116141 (1992).

353 Stegmann, T. *et al.* Functional reconstitution of influenza virus envelopes. *EMBO J* **6**, 2651-2659 (1987).

354 Nussbaum, O., Lapidot, M. & Loyter, A. Reconstitution of functional influenza virus envelopes and fusion with membranes and liposomes lacking virus receptors. *J Virol* **61**, 2245-2252, doi:10.1128/JVI.61.7.2245-2252.1987 (1987).

355 Amacker, M. *et al.* Peptide-loaded chimeric influenza virosomes for efficient in vivo induction of cytotoxic T cells. *Int Immunol* **17**, 695-704, doi:10.1093/intimm/dxh249 (2005).

356 Gotzke, H. *et al.* The ALFA-tag is a highly versatile tool for nanobody-based bioscience applications. *Nat Commun* **10**, 4403, doi:10.1038/s41467-019-12301-7 (2019).

357 Gonzalez-Sapienza, G., Rossotti, M. A. & Tabares-da Rosa, S. Single-Domain Antibodies As Versatile Affinity Reagents for Analytical and Diagnostic Applications. *Front Immunol* **8**, 977, doi:10.3389/fimmu.2017.00977 (2017).

358 Kaplan, C. & Ewers, H. Optimized sample preparation for single-molecule localization-based superresolution microscopy in yeast. *Nat Protoc* **10**, 1007-1021, doi:10.1038/nprot.2015.060 (2015).

359 Rahman, A. H., Taylor, D. K. & Turka, L. A. The contribution of direct TLR signaling to T cell responses. *Immunol Res* **45**, 25-36, doi:10.1007/s12026-009-8113-x (2009).

360 Manicassamy, S. & Pulendran, B. Modulation of adaptive immunity with Toll-like receptors. *Semin Immunol* **21**, 185-193, doi:10.1016/j.smim.2009.05.005 (2009).

361 Davis, C. W. *et al.* Influenza vaccine-induced human bone marrow plasma cells decline within a year after vaccination. *Science*, doi:10.1126/science.aaz8432 (2020).

362 Nguyen, D. C., Joyner, C. J., Sanz, I. & Lee, F. E. Factors Affecting Early Antibody Secreting Cell Maturation Into Long-Lived Plasma Cells. *Front Immunol* **10**, 2138, doi:10.3389/fimmu.2019.02138 (2019).

363 Chen, J., Kelley, W. J. & Goldstein, D. R. Role of Aging and the Immune Response to Respiratory Viral Infections: Potential Implications for COVID-19. *J Immunol* **205**, 313-320, doi:10.4049/jimmunol.2000380 (2020).

364 Brodin, P. & Davis, M. M. Human immune system variation. *Nature reviews. Immunology* **17**, 21-29, doi:10.1038/nri.2016.125 (2017).

365 De Maio, A., Torres, M. B. & Reeves, R. H. Genetic determinants influencing the response to injury, inflammation, and sepsis. *Shock* **23**, 11-17, doi:10.1097/01.shk.0000144134.03598.c5 (2005).

366 Hill, A. V. The genomics and genetics of human infectious disease susceptibility. *Annu Rev Genomics Hum Genet* **2**, 373-400, doi:10.1146/annurev.genom.2.1.373 (2001).

367 Tuite, A. & Gros, P. The impact of genomics on the analysis of host resistance to infectious disease. *Microbes Infect* **8**, 1647-1653, doi:10.1016/j.micinf.2005.11.016 (2006).

368 van der Made, C. I. *et al.* Presence of Genetic Variants Among Young Men With Severe COVID-19. *JAMA*, doi:10.1001/jama.2020.13719 (2020).

369 Trammell, R. A. & Toth, L. A. Genetic susceptibility and resistance to influenza infection and disease in humans and mice. *Expert Rev Mol Diagn* **8**, 515-529, doi:10.1586/14737159.8.4.515 (2008).

370 Zuniga, J. *et al.* Genetic variants associated with severe pneumonia in A/H1N1 influenza infection. *Eur Respir J* **39**, 604-610, doi:10.1183/09031936.00020611 (2012).

371 Abdelaal, T. *et al.* Predicting Cell Populations in Single Cell Mass Cytometry Data. *Cytometry A* **95**, 769-781, doi:10.1002/cyto.a.23738 (2019).

372 Platt, J. C. Probabilistic outputs for support vector machines and comparisons to regularized likelihood methods. *Advances in Large Margin Classifiers* (2000).